Department of Precision and Microsystems Engineering

Design Optimization of Shock Mounts Subjected to an Underwater Blast Wave

Siddharth Sivaramakrishnan

Report no : 2020.037
Coach : Dr.ir.M.(Matthijs) Langelaar, ir.S.J.(Sanne) van den Boom
Professor : Dr.ir.M.(Matthijs) Langelaar
Specialisation : Structural Optimization and Mechanics
Type of report : MSc Thesis
Date : 29 September 2020

TU Delft Delft University of Technology

Precision and Microsystems Engineering

Challenge the future

DESIGN OPTIMIZATION OF SHOCK MOUNTS

SUBJECTED TO AN UNDERWATER BLAST WAVE

Master of Science Thesis Report

In partial fulfillment of the requirements for the degree of

Master of Science in Mechanical Engineering

by

Siddharth SIVARAMAKRISHNAN

to be defended publicly on 29 September 2020

Precision and Microsystems Engineering (PME)
Faculty of Mechanical, Maritime and Materials Engineering (3mE)
Delft University of Technology
The Netherlands

Thesis Committee:

Dr.ir.M.(Matthijs) Langelaar,	Delft University of Technology
Dr.ir.J.H.(Henk) den Besten	Delft University of Technology
ir.Sabiju Valiya Valapppil	Delft University of Technology
ir.S.J.(Sanne) van den Boom,	TNO

"Aim for excellence, work hard, nobody is going to do it for you. Listen and learn, even if you know the answer. Let the good news take the stairs and bad news take the elevator. Help others rise. Greatness comes not from position but helping build the future. Be fair with yourself. And more important: remember who you are and where you come from, always."

This page is intentionally left blank.

CONTENTS

This page is intentionally left blank.

ABSTRACT

Shock mounts are crucial components in reducing the transmissibility of a shock or impact, thereby protecting the objective system. Such shock mounts are application-specific and need a redesign for specific uses. This study establishes a transient nonlinear finite element optimization procedure to design a shock mount for withstanding an underwater blast wave. The work showcases the analysis of two design concepts. The first design demonstrates average acceleration transmissibility of 5.51×10^{-3}. The second design exploits the phenomenon of reflection of waves at an interface. This design is unique, promising a factor 3.263 lower average transmissibility than the first design which is similar without the metal interface. The study also details the modeling and analysis of both shock mount designs using 2D axisymmetric and 3D transient nonlinear finite element analyses. The results of both these analyses were comparable, making a 2D study efficient and reliable in the analysis and optimization of shock mounts.

This page is intentionally left blank.

EXECUTIVE SUMMARY

Shock mounts are interface devices that support sensitive equipment and protect the objective from any external disturbances. Multiple shock mounts exist in various shapes employing various concepts, where each one is specific in its respective function. Many factors such as the environmental conditions, nature of loading, the sensitivity of the objective equipment, aftershock response, and the transmissibility that needs to be achieved, etc. all contribute to the design of an optimal shock mount.

This thesis aims to develop and optimize a shock mount for use in marine vessels capable of protecting itself and the objective equipment from underwater explosions. The final product is a device that is compliant under huge impact loads. The study also includes the investigation of the shock mount under various magnitudes of shock loads and analyzing its performance.

Neoprene nonlinear hyperelastic material and its analytical nonlinear material model was found to be a suitable candidate to model the shock mount. Various material models from the literature were analyzed and the polynomial order 3 material model was found to represent the test data better.

Nature inspires technology and provides interesting solutions to fundamental problems. Two design concepts are generated inspired by nature and literature. The shock mount in the first design concept is modeled completely using the neoprene material. The second concept is unique in using the behavior of waves phenomenon at an interface between Neoprene and structural steel. This concept partially reflects and transmits the incoming shock wave also undergoing a total internal reflection. Theoretically, the second design can reduce the transmissibility by about eight times, transmitting only 12.4% of the incoming shock wave. This concept shock mount employed in the second design delivers 0.2% overall average transmissibility when analyzed numerically using finite elements. A similar design without the interface provides an overall average transmissibility of 0.55%. This is one of the promising outcomes of this thesis. The implementation of both the designs with their limitations is also discussed. Both geometries are modeled as cylinders so that they can be approximated as 2D axisymmetric and generated using revolve in 3D analysis respectively.

An underwater explosion is an extreme event that propagates in all directions underwater as pressure waves and in the form of cavitation bubbles. The pressure wave imparts a vertical shock on the ship. Modeling of such an event is discussed along with the Taylor flat plate theory. Here the vessel is assumed to be a flat plate and this theory is used to translate the pressure waves into corresponding displacement, velocity, and acceleration responses of the ship. This displacement response data is used as the boundary load for the shock mount to be analyzed. A complete transient nonlinear finite element analysis procedure in Abaqus for the analysis of the shock mount in 2D and 3D is provided. The finite element solution sampling and optimal mesh sizes are determined using solution convergence studies. The element mesh sizes play a significant role in the cost of the analysis. Even though the second design was modeled using a coarser mesh, its analysis was computationally costlier than the first design.

An optimization validation study was performed and the BOBYQA optimization algorithm was found to perform better under simulated numerical noise. But the optimizer never converged to a global optimum with the shock problem under study. Therefore best results obtained from the optimization and parametric studies were selected to come up with a virtual global optimum. The results of the virtual global optimum design were verified using the 3D analysis. The results of the 2D and 3D studies were similar. This makes a 2D analysis sufficient to optimize and analyze the shock mounts. The acceleration, stress, and frequency results were found to lie within the limits for most conditions and few exceptions are discussed. The second multi-material design with an interface performed better in all the analyses and is proposed as a suitable shock mount candidate.

The results of the thesis are promising and can be used for optimizing shock mounts subject to the applications of interest.

PREFACE

This master thesis on "Design Optimization of Shock Mounts Subjected to an Underwater Blast Wave", describes the approach to analyze the shock mount and optimize its shape. This thesis is the concluding component of my graduation at the Department of Precision & Microsystems Engineering (PME), in the Structural Optimization and Mechanics group. The report has been written to fulfill the graduation requirements for MSc Mechanical Engineering at the Delft University of Technology.

The project was provided by the Structural Dynamics department of the Netherlands Organization for Applied Scientific Research (TNO) and undertaken at the Delft University of Technology, under the supervision of Matthijs Langelaar and Sanne van den Boom. I would like to thank them for their guidance at the right time and for motivating me through the project. They were with me from day 1, always on time, in giving me feedback and understanding my difficulties. They were flexible and gave me the freedom to do my research, making me the boss of this project. They made me realize what I am capable of, this helped me in discovering my strengths and working with my weaknesses. It was a very good learning experience working with them.

I am indebted to Eveline Matroos, for her kindness and guidance throughout my master's education. She was very quick in understanding and solving my academic and personal problems. I would like to thank the 3mE service desk for helping me solve all software issues. They were with me when I was experimenting with multiple ways to solve the problem, and helped me in getting licenses and directing me to people who could help me. I would like to acknowledge the efforts of Jan Hol, Secretary of the Department of Aerospace Structures Materials, who helped me in figuring out ways to efficiently use Abaqus over HPC.

I am grateful to The Foundation Justus & Louise van Effen for completely supporting my two-year education at TU Delft. I will in the future contribute back to society with my technical knowledge, bringing technological developments in solving societal issues.

My friends and fellow students were true motivators, enquiring constantly about my progress and sharing the experiences with their work. They helped me to take decisions during tough times. Finally, I would like to thank my parents, their blessings have got me here into TU Delft. Their thoughts about my future motivate and gave me the confidence to face all the challenges in life. They were with me every day over the phone, taking care of my physical and mental health.

Siddharth Sivaramakrishnan
Delft, September 2020

This page is intentionally left blank.

LIST OF FIGURES

LIST OF TABLES

This page is intentionally left blank.

1

INTRODUCTION

Shock mounts are used as a mechanical isolator between systems, thereby preventing the flow of energy into the objective system. They find vital applications in defense to protect critical systems. The electronics and delicate components inside the objective system are vulnerable to vigorous shocks, as the acceleration transmitted to the system creates forces, which the connections and components in the subsystems are unable to handle. Also in a general context, shock mounts are crucial components ensuring structural safety and reliability. They are used to delay, spread out, absorb and dampen out shock impulses reducing transmissibility. In this thesis, the shock mount is designed using a systematic simulation-based design approach, in the context of marine applications. Considering the complexity of the phenomenon and responses involved, designing an optimal shock mount is a challenging task. The process typically involves multiple manual design iterations. Automated shape optimization is expected to be highly beneficial and justifies the effort in terms of design time and shock mount performance.

1.1. PROBLEM DEFINITION

The objective of the thesis is to explore the use of design optimization techniques to design and analyze the shock mount, which is to be mounted on the ship platform, under the application of a TNT blast shock wave. The shock mount needs to be optimized for lowering the transmissibility of the shock to the objective mass, thus shielding it from the shock. The shock-induced acceleration is very large and induces large deflections. The frequency of the acceleration applied to the objective mass is also important. Acceleration induces forces that can excite the eigenmodes of the objective mass. This creates the need to push the frequency of the acceleration, experienced by the objective mass, to a lower value. Developing a novel design to suppress high accelerations of the objective mass using design optimization techniques is the aim of the thesis.

1.2. PROBLEM APPROACH

This report comprises the developed procedure to be used in the design optimization of shock mounts. The shock mounts made of rubber or elastomeric materials are used when operating under large deflections[12]. A proper material choice is necessary considering its use in the marine environment. In this thesis, numerical simulations are used to evaluate shock mount performance. Hyperelastic material properties are applied to the model using suitable material models. The shock profile of the blast wave along with the dynamics of the shock mount under shock loading is studied. This helps in determining the loading and boundary conditions of the model. Shock mount designs vary depending on the mass they carry, the load they experience, and various other parameters. Considering all these factors, a basic design of the shock mount is developed. This shock mount is modeled, parameterized, and analyzed using Abaqus, a commercial FE solver. Shock mounts are then optimized to meet the performance characteristics of the structure under the impact, this tunes the shock mount to shield the specific structure. Relevant results are extracted and interpreted to study the model better. A complete procedure of developing a shock mount under blast loading, including the aspects of design initiation, material selection, approximations, modeling, loading, analysis, and optimization, is the outcome of this report.

1.3. REPORT STRUCTURE

The structure is aligned with the systematic analysis procedure. The first three chapters deal with the theory behind the analysis. The material properties and the chosen material model which describes hyperelastic behavior is reviewed in Chapter 2. Shock mount design along with a detailed explanation of the theory behind is discussed in Chapter 3. The shock experienced by the mounts and the derivation of loads applied to the model is summarized in Chapter 4. The chapter discusses the theory behind the shock wave and its uniqueness, high-intensity impulses acting for a very short span. The next three chapters deal with the modeling, optimization, and verification of the model. Finite element modeling of the structural shock mount and its implementation is outlined in Chapter 5. The optimization technique that is used in the optimization of structural shock mounts is discussed in Chapter 6. Verification and performance of the analysis are conducted in Chapter 7. Results obtained from the analysis are presented and discussed in Chapter 8. Towards the end, a conclusion along with the recommendations are summarized in Chapter 9.

2

MATERIAL MODELS

2.1. INTRODUCTION

It can be postulated that a shock mount undergoes large deformation when subjected to huge impact loading. Such deformations are too large to be represented by the classical theory of small strains. Hyperelastic materials/elastomers/rubbers are the kind of materials that can accommodate such deformations and exhibit a highly nonlinear deformation response. This chapter discusses the analytical modeling of such materials using elastomeric/hyperelastic material models. Such hyperelastic materials are nearly incompressible, and when the material is not in a confined volume (when free to deform) it undergoes large shear[13].

2.2. MATERIALS USED

Natural rubber is the most widely used elastomer and accounts for 50% of all produced shock absorbers. It is cheap and exhibits a large stretch capacity. It is highly elastic with low hysteresis and is a thermoset once vulcanized[14]. Butyl rubber is a synthetic thermoset that resembles natural rubber in properties. Isoprene (or Polyisoprene) has low hysteresis and high tear resistance, making it highly elastic and tough. It is processed the same way as natural rubber and therefore called synthetic natural rubber[14]. Butyl, Chlorobutyl, and Bromobutyl rubbers show high damping and energy absorption properties. Neoprene is a synthetic rubber composed of carbon, hydrogen, and chlorine polymers[14]. All these materials are used in anti-vibration mounts and are suitable candidates for application in shock mounts. For the current study neoprene rubber is chosen due to the following properties and applications:

1. Neoprene is temperature, oil, and water-resistant.
2. It is used for corrosion-resistant coatings and in materials that face harsh conditions and too much wear.
3. It is weather, flame, and compression resistant.
4. It is used in marine applications for waterproofing and in the manufacture of wetsuits.
5. Neoprene has high tensile strength, resilience, and elongation.

The chlorine present in Neoprene prevents it from swelling when exposed to oil and fuel while giving it more resistance to oxidation. It also makes it fire resistant. Neoprene was used as shock mounts for engines, in a study conducted at T.N.O and other agencies[15]. Neoprene has one of the lowest acoustic impedance values, making it a good candidate for exploiting the phenomenon of reflection of a wave at an interface when used along with a high acoustic impedance material. All these physical properties and applications make Neoprene the best candidate for application in marine and critical applications. Modeling of hyperelastic materials such as neoprene is discussed in the next section.

2.3. HYPERELASTIC MATERIAL MODELS

A material is hyperelastic if there exists an elastic strain energy density function (ψ) that is a scalar function of strain deformation tensors, whose derivatives with respect to strain components determine the corresponding stress components[16]. Such materials have nonlinear stress-strain curves, are incompressible, and strain rate independent. Such materials can be modeled using hyperelastic material models. The choice of the material model depends on its applications, corresponding variables and data available to determine material parameters[16]. The most important and often used hyperelastic material models[17] are Neo-Hookean[18], Mooney-Rivlin[19], Arruda-Boyce[20], Polynomial[21], Reduced Polynomial[22], Yeoh[23] and Ogden[24]. All these material models are compared and discussed below. The hyperelastic material stability criterion is discussed in Sec. A.1.2.

Uniaxial, biaxial, planar (shear) and volumetric test data of neoprene material is obtained from Ansys Material Library[9] and is provided for reference in Appendix A.2. The test data used in the analysis that is used to model the Neoprene hyperelastic material is plotted in Fig. A.2. Deformation modes of obtained test results are shown in Fig. A.1. This data is used to fit and compare material models in the next subsection.

2.3.1. COMPARISON

Different material models are studied and their performances are compared in Tab. 2.2. The residual obtained by computing the nominal error of the curve is tabulated. The polynomial order 3 material model fits the curve better and is used throughout all studies and analyses in this report. It is recommended not to for higher orders of N than the one necessary and unless it improves the fit to a large extent. Using very high orders of N may cause more oscillations, leading to instability in the stress-strain curve.

Material Model	Order (O) / Parameter (P)	Residual
Neo-Hookean	-	2.7153
Mooney-Rivlin	2 P	2.5025
	3 P	2.4775
	5 P	1.2009
	9 P	0.42109
Yeoh	1 O	2.7153
	2 O	1.8618
	3 O	0.88194
Ogden	1 O	2.5901
	2 O	29.003
	3 O	24.68
Arruda-Boyce	-	1.4873
Polynomial	1 O	2.5025
	2 O	1.2009
	3 O	0.42105

Table 2.1: Comparison Table.

Material Parameters	Value (Unit)
Material Constant C_{10}	11782 Pa
Material Constant C_{01}	2235.6 Pa
Material Constant C_{20}	-70.43 Pa
Material Constant C_{11}	253.24 Pa
Material Constant C_{02}	19.277 Pa
Material Constant C_{30}	1.4735 Pa
Material Constant C_{21}	7.7492 Pa
Material Constant C_{12}	-1.0873 Pa
Material Constant C_{03}	0.03325 Pa
Incompressibility Parameter $D1$	1.4346×10^{-7} Pa^{-1}
Incompressibility Parameter $D2$	-1.7474×10^{-7} Pa^{-1}
Incompressibility Parameter $D3$	5.7345×10^{-9} Pa^{-1}

Table 2.2: Material parameter values for Polynomial order 3 material model.

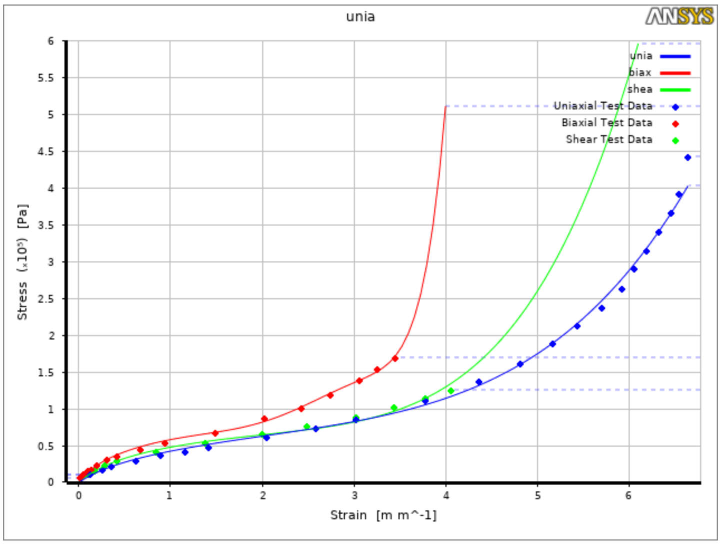

Figure 2.1: Plot showing all three test data curve fitted employing polynomial material model of order 3, using the parameters computed in Tab. 2.2.

2.3.2. DETERMINING THE PARAMETERS FOR POLYNOMIAL MATERIAL MODEL

The material parameters/constants of any hyperelastic material model are determined by fitting the stress-strain curve. For this study, the stress-strain curve is fitted using the Polynomial order 3 material model. Material parameter values associated with the model are tabulated in Tab. 2.2. Fitted curves for all three test modes are shown in Fig. 2.1. The analytical modeling of the polynomial material model along with its relation to other material models is given in Sec. A.1.

2.4. VISCOSITY

Damping associated with volumetric straining is achieved by applying a bulk viscosity to the model. This improves the modeling of high-speed dynamic events such as blast shocks. Abaqus recommends using default bulk viscosity parameters. Bulk viscosity pressure is intended as a numerical effect only, therefore it is not included in the material point stresses [25].

2.4.1. LINEAR BULK VISCOSITY

Linear bulk viscosity produces a bulk viscosity pressure which is linear in the volumetric strain rate and is given by Eq. 2.1. This is always included in order to damp the "ringing" effect in the highest element frequency[25].

$$p_1 = b_1 \rho c_d L^e \dot{\epsilon}_{vol} \tag{2.1}$$

In Eq. 2.1, b_1 is the damping coefficient, by default it has a value 0.06 in Abaqus. ρ is the current material density, c_d is the current dilatational wave speed, L^e is the characteristic length of the element, and $\dot{\epsilon}_{vol}$ is the volumetric strain rate.

2.4.2. QUADRATIC BULK VISCOSITY

Quadratic bulk viscosity is applied only if the volumetric strain is compressive. Bulk viscosity pressure follows Eq. 2.2 which is quadratic in strain rate. Here b_2 is the damping coefficient with a default value of 1.2 in Abaqus[25].

$$p_2 = \rho \left(b_2 L^e\right)^2 \left|\dot{\epsilon}_{vol}\right| \min(0, \dot{\epsilon}_v ol) \tag{2.2}$$

The time in which a dilatational wave travels across an element is precisely the stable time increment size. This makes the element collapse to zero volume in a one-time increment if the initial nodal velocity is equal to the dilatational speed of the material. The quadratic bulk viscosity term smears a shock front across several elements under extremely high-velocity gradients, by introducing a resisting pressure. This helps in preventing elements from collapse.

This page is intentionally left blank.

3

Shock Mount Design

3.1. Introduction

Various energy absorbing and dissipating devices have been developed for mounting sensitive equipment. Such devices absorb the energy from an impact, the energy is later dissipated and/or transmitted in low-intensity spread over time. This reduces the transmissibility of shock to the objective mass. Compression spring with a viscous damper is the most widely used energy absorber for applications experiencing small deformations. The characteristic of such a mount is stiff under impact loading and relatively compliant under gradual loading This is due to the presence of the viscous component which resists deflection/velocity. To introduce a more compliant characteristic under impact loading and absorb a greater amount of impact energy a shock absorber type of mounting mechanism is used. This chapter briefly reviews various relevant aspects of shock mounts and their design, and on that basis, the design concepts that will be studied in this thesis are proposed.

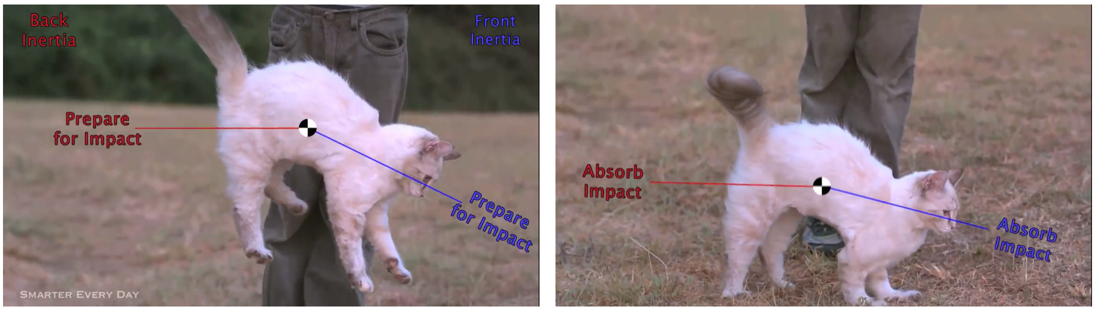

(a) Free Fall

(b) Touch Down

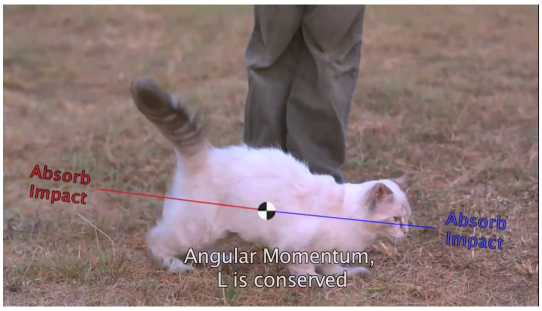

(c) Loading

Figure 3.1: Three stages during impact as experienced by the cat.[2]

3.2. INSPIRATION

Nature and biological life offer solutions to many engineering problems. Cats dropped from a larger height escape the fall without any hurt. The energy of the impact is absorbed instantaneously and transferred to the body over time, this reduces and limits the maximum deceleration experienced by the cat's body at any instance of time. The three stages during impact; free fall, touch down, and loading as experienced by the cat is shown in figure Fig. 3.1. Similar behavior can also be observed during jumping and landing of a human as shown in Fig. B.1. The legs do not dissipate significant energy, but in turn, they prologue the impact, which reduces the transmissibility and spreads it over time. This basically converts high magnitude very short duration impact which is dangerous into low magnitude large duration impact, the total energy is conserved. The shock experienced by the shock mount to be designed and optimized is quite drastic. Inspiration for such a design as discussed in further sections can be traced to these designs observed in nature.

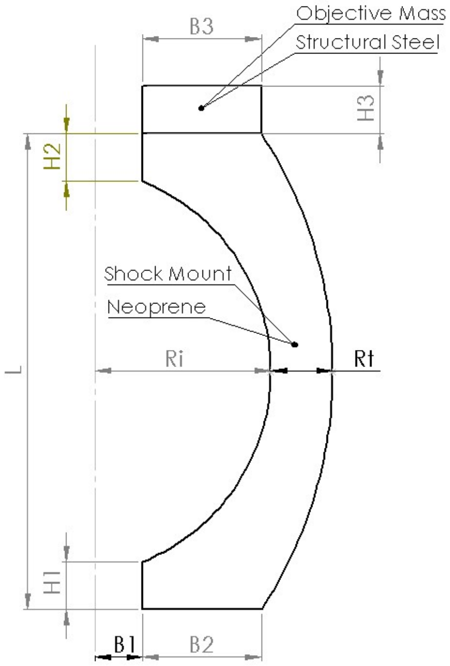

Figure 3.2: Design 1.0 with all its parameters.

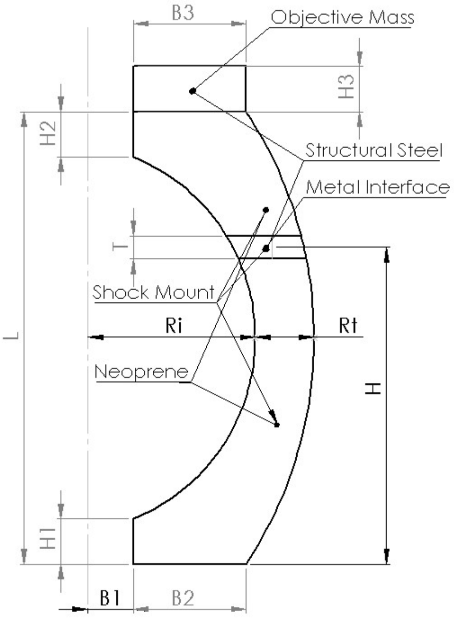

Figure 3.3: Design 2.0 with all the parameters.

3.3. DESIGN 1.0

The first considered design is to model the shock mount in close relation to that of the biological leg. The variation being, the model is assumed to be a 360° revolved extrusion of the geometry, this is done in order to make the forces balanced during impact. This 3D geometry is represented as an axisymmetric 2D case as shown in Fig. 3.2. In the model, the geometry enclosed by parameters B3xH3 is the "Objective Mass", which needs to be protected from the shock. The geometry to the bottom of the Objective Mass is the "Shock Mount" that needs to be optimized to contain the shock. The geometry even though simple can represent quite a range of stiffness and motion conditions. This geometry is parameterized as shown in Fig. 3.2, to be used in further design optimization studies. The load is applied at the bottom of the geometry with dimension B2. The thickness H1 is added to the bottom in order to avoid extreme deformation of elements close to the support due to the extreme load applied. This thickness helps to distribute and transfer the load better into the shock mount. The thickness h2 helps in the stabilization of the mass and spreading the propagated shock evenly. The amount of mass on the Shock Mount can be controlled using the parameter H3. The value of B3 need not be equal to B2. It is also important to increase B2 as thickness Rt moves further right of B2. This sufficient thickness of B2 helps to prevent the folding of the hyperelastic material around the right corner of B2 due to self-weight and static loading. Length L of the Shock Mount can be determined based on the magnitude of the applied load and travel experienced by the Objective Mass. Ri determines the curvature of the Shock Mount and Rt controls its thickness at the minimum point.

3.4. DESIGN 2.0

During preliminary simulation studies, the energy propagation in the hyperelastic shock mount concept model was observed to behave similarly to a wave. This phenomenon of wave propagation is exploited to limit the transmission of the shock, using the behavior of waves at an interface, which is discussed in the next subsection.

3.4.1. DESIGN IMPLEMENTATION

In Design 2.0 the basic design of Design 1.0 is updated with the Metal Interface, which helps in reducing transmissibility significantly. This 3D geometry is approximated as an axisymmetric 2D case as shown in Fig. 3.3. In the model, the geometry enclosed by parameters B3xH3 is the "Objective Mass", which needs to be protected from the shock. The geometry to the bottom of the Objective Mass is the "Shock Mount" that needs to be optimized to contain the shock. The geometry at location H from support enclosed within parameter T is the metal interface. This geometry is parameterized as shown in Fig. 3.3, to be used in the upcoming shape optimization studies. The load is applied at the bottom of the geometry with dimension B2. This model has added mass to the system in the form of the metal interface and therefore requires a broader base to stiffen the system to hold/stabilize the system under static gravity loading.

3.4.2. BEHAVIOR OF WAVES AT AN INTERFACE

Wave interaction with a material interface results in two waves, where one wave, u_t is transmitted across the interface as a forward-propagating wave and the second wave, u_r is being reflected from the interface as a backward propagating wave[3]. The Fig. 3.4 describes the phenomenon at the interface.

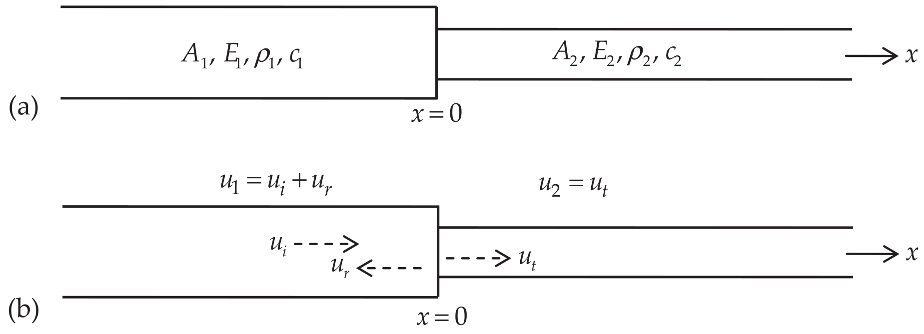

Figure 3.4: Two materials interacting at $x = 0$ in a uniform bar: a) material and geometric properties; b) transmitted and reflected waves. Where, A is the area of cross section, E is the Young's modulus, ρ is the density and c is the wave speed.[3]

From Fig. 3.4, for a given $\hat{u}_i$, $\hat{u}_r$ and $\hat{u}_t$ can be defined using the material and geometric properties, as shown in Eq. 3.1,where $\hat{u}_i$, $\hat{u}_r$ and $\hat{u}_t$ are complex wave amplitudes containing both magnitude and phase information. They are defined as in Eq. 3.2, where γ is the wave number and Z is the acoustic impedence defined as $Z = \rho c$. [3]

$$\begin{aligned} \hat{u}_r &= \frac{Z_1 A_1 - Z_2 A_2}{Z_1 A_1 + Z_2 A_2} \hat{u}_i \\ \hat{u}_t &= \frac{2 Z_2 A_1}{Z_1 A_1 + Z_2 A_2} \hat{u}_i \end{aligned} \tag{3.1}$$

$$\begin{aligned} u_i(x,t) &= \hat{u}_i e^{i(\gamma_1 x - \omega t)} \\ u_r(x,t) &= \hat{u}_r e^{i(-\gamma_1 x - \omega t)} \\ u_t(x,t) &= \hat{u}_t e^{i(\gamma_2 x - \omega t)} \end{aligned} \tag{3.2}$$

Reflection and transmission coefficients can be defined in terms of displacements, stress (σ) at interface, and stress wave amplitudes ($\hat{\sigma}$) as shown in Eq. 3.3. The relation between stress wave and stress is shown in Eq. 3.4. [3]

$$
\begin{aligned}
R &= \frac{-Z_1A_1 + Z_2A_2}{Z_1A_1 + Z_2A_2} = -\frac{\hat{u}_r}{\hat{u}_i} = \frac{\sigma_r}{\sigma_i}\bigg|_{x=0} = \frac{\hat{\sigma}_r}{\hat{\sigma}_i} \\
T &= \frac{2Z_2A_1}{Z_1A_1 + Z_2A_2} = \frac{Z_2}{Z_1}\frac{\hat{u}_r}{\hat{u}_i} = \frac{\sigma_t}{\sigma_i}\bigg|_{x=0} = \frac{\hat{\sigma}_t}{\hat{\sigma}_i}
\end{aligned}
\tag{3.3}
$$

$$
\begin{aligned}
\sigma_i(x,t) &= \hat{\sigma}_i e^{i(\gamma_1 x - \omega t)} \\
\sigma_r(x,t) &= \hat{\sigma}_r e^{i(-\gamma_1 x - \omega t)} \\
\sigma_t(x,t) &= \hat{\sigma}_t e^{i(\gamma_2 x - \omega t)}
\end{aligned}
\tag{3.4}
$$

ANALYSIS

For the case used in the model where $A_1 = A_2$, Eq. 3.3 simplifies into Eq. 8.4. From Eq. 8.4 it can be observed that the reflection and transmission coefficients are functions of the acoustic impedances, which is a material property. It is stress which translates into force and later into acceleration across the boundary. The measure of this reflection and transmission coefficients provide the amount of wave energy transmitted and reflected, which forms the basic principle of the design.

$$
\begin{aligned}
R &= \frac{-Z_1 + Z_2}{Z_1 + Z_2} = \frac{\sigma_r}{\sigma_i}\bigg|_{x=0} \\
T &= \frac{2Z_2}{Z_1 + Z_2} = \frac{\sigma_t}{\sigma_i}\bigg|_{x=0}
\end{aligned}
\tag{3.5}
$$

The acoustic impedance of Neoprene Rubber is $Z_{Neoprene} = 1.55 \times 10^6$ kg m^{-2}s^{-1}[26]. From literature the best candidate for the interface material is chosen to be Structural (Mild) Steel with an acoustic impedance of $Z_{Steel} = 46.7 \times 10^6$ kg m^{-2}s^{-1}. Metals such as Gold ($Z = 63 \times 10^6$ kg m^{-2}s^{-1}), Platinum ($Z = 85 \times 10^6$ kg m^{-2}s^{-1}) and Tungsten ($Z = 100 \times 10^6$ kg m^{-2}s^{-1}) have higher acoustic impedance, but Structural Steel is chosen taking into account easy and cheap implementation[27].

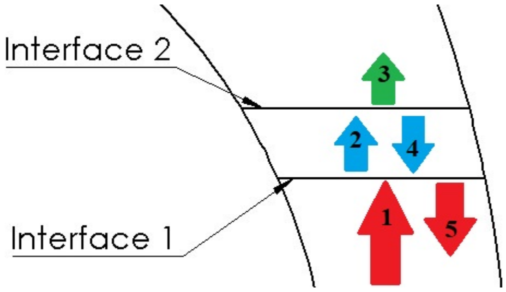

Figure 3.5: Enlarged metal interface of Design 2.0.

In Fig. 3.5, two interface boundaries are shown, Interface 1 and Interface 2. Structural Steel is assembled in the region between Interface 1 and Interface 2. The material outside this region is hyperelastic Neoprene rubber. The shock reaches the interface from the support through 1 and propagates to the objective mass through 3.

At Interface 1:

From Fig. 3.5, 1 is the incident wave, 2 is the transmitted wave and 5 is the reflected wave at Interface 1.

The Coefficient of reflection corresponding to wave 5 is given by Eq. 3.6 and the coefficient of transmission corresponding to wave 2 is given by Eq. 3.7. Here $Z_1 = Z_{Neoprene}$ and $Z_2 = Z_{Steel}$ are applied.

$$\begin{aligned} R_1 &= \left.\frac{\sigma_r}{\sigma_i}\right|_{x=0} = \frac{-Z_1 + Z_2}{Z_1 + Z_2} \\ R_1 &= \left.\frac{\sigma_r}{\sigma_i}\right|_{x=0} = 0.93575 \end{aligned} \tag{3.6}$$

$$\begin{aligned} T_1 &= \left.\frac{\sigma_t}{\sigma_i}\right|_{x=0} = \frac{2Z_2}{Z_1 + Z_2} \\ T_1 &= \left.\frac{\sigma_t}{\sigma_i}\right|_{x=0} = 1.93575 \end{aligned} \tag{3.7}$$

R_1 positive and <1 denotes that the reflected wave has the same nature as that of the incident wave with amplitude diminished.T_1 positive and >1 denotes that the reflected wave has the same nature as that of the incident wave with amplitude magnified.

At Interface 2:
From Fig. 3.5, 2 is the incident wave, 3 is the transmitted wave and 4 is the reflected wave at Interface 2. The Coefficient of reflection corresponding to wave 4 is given by Eq. 3.8 and the coefficient of transmission corresponding to wave 3 is given by Eq. 3.9. Here $Z_1 = Z_{Steel}$ and $Z_2 = Z_{Neoprene}$ are applied.

$$\begin{aligned} R_2 &= \left.\frac{\sigma_r}{\sigma_i}\right|_{x=0} = \frac{-Z_1 + Z_2}{Z_1 + Z_2} \\ R_2 &= \left.\frac{\sigma_r}{\sigma_i}\right|_{x=0} = -0.93575 \end{aligned} \tag{3.8}$$

$$\begin{aligned} T_2 &= \left.\frac{\sigma_t}{\sigma_i}\right|_{x=0} = \frac{2Z_2}{Z_1 + Z_2} \\ T_2 &= \left.\frac{\sigma_t}{\sigma_i}\right|_{x=0} = 0.0642487 \end{aligned} \tag{3.9}$$

R_2 negative and <1 denotes that the reflected wave has the opposite nature as that of the incident wave (i.e., an incoming compression wave is reflected as a tension wave) with amplitude diminished.T_2 positive and ≪1 denotes that the reflected wave has the same nature as that of the incident wave with amplitude largely diminished.

From Eq. 3.7 and Eq. 3.9, the amplitude of the wave leaving the Interface 2 is 0.12437 times the amplitude of the incident wave at Interface 1. This concept lowers the transmissibility by about eight times, transmitting only 12.4% of the incoming shock wave. This is a significant theoretical reduction in transmissibility compared to Design 1.0. The wave reflected at Interface 2 will again get reflected by Interface 1, this will follow total internal refection and create a buffer of stress waves that are released slowly. This phenomenon helps prevent instantaneous shock from reaching the objective mass. The amplitude of respective waves as the ratio of the incident wave is shown in Fig. 3.6.

3.5. ASSUMED DESIGN WORKING CONDITIONS

The midsection view of the proposed Design 1.0 and Design 2.0 are shown in Fig. 3.8. The red guide rod present along with the base support will ensure the system does not deviate much from the vertical position. The flexibility/horizontal bending stiffness of the rod will bring the system back to the vertical position if it suffers from such a horizontal load. The contact between the red and green metallic parts if so any is modeled to be a line contact. All the horizontal interfaces in Fig. 3.8, including the blue metal interface,

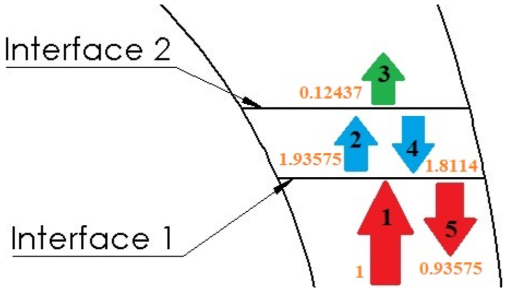

Figure 3.6: Enlarged metal interface of Design 2.0 with respective amplitude ratios.

are bonded to each other with a sufficiently strong adhesive. All the vertical interfaces are lubricated. The vertical interfaces also prevent excessive distortion to the surface under very high impact loading. The shock mount is supported to the base structure using bolts and internal threading in the support. The green and red support act as stoppers when the shock mount is loaded with excessive load and limits the travel of the shock mount. This is added as complete compression of the shock mount was observed during the initial designs. Such a complete compression was avoided by choosing a proper parameter value for B2, by increasing the vertical stiffness under compression. However, for safety, a stopper is added. The use of the metallic guide is optional and is not recommended for use in very high impact loads. But then the structure has to be protected differently from large transverse loads.

3.5.1. APPROXIMATIONS

The approximations made during the design of the shock mount is given below:

1. The load due to the applied mass is not eccentric. This ensures and it is assumed that there is no contact between the green and red metallic supports in Fig. 3.8. But they just stabilize the system, bring it back to the default non-eccentric configuration, when an excessive horizontal load is applied.
2. The orange objective mass on the top in Fig. 3.8 is of no detail and it just acts as a constant stable mass (i.e the mass by itself does not have any dynamics).
3. The vertical interface walls of the black rubber shock mount connecting the green and red part metallic supports, in Fig. 3.8, are well lubricated and are taken to be frictionless.
4. To avoid a numerically expensive contact problem, it is assumed that all horizontal interfaces in Fig. 3.8 are rigid and undergo zero relative motion.
5. The vertical interfaces of the black SA in Fig. 3.8 are constrained in one direction by the green and red metallic supports. That is from the shown configuration $x > 0$ and $\delta z > 0$ at the interface. But this introduces a metal-hyperelastic contact problem. As the loading is almost compressive (it is in tension during bounce back, vertically overshooting the normal position in the upward direction for a relatively small period) the SA is almost always in contact with the vertical interface. This can be approximated by constraining the vertical interface displacements in the horizontal directions, i.e $u_x = 0$ and $u_z = 0$ at the vertical black-green, black-red interface in Fig. 3.8.
6. The gap in between the red and green metallic supports is sufficient to escape the air in the cavity of the shock mount without causing any pressurization. In reality, this might cause some damping to aftershock oscillations, bringing stability to the system.

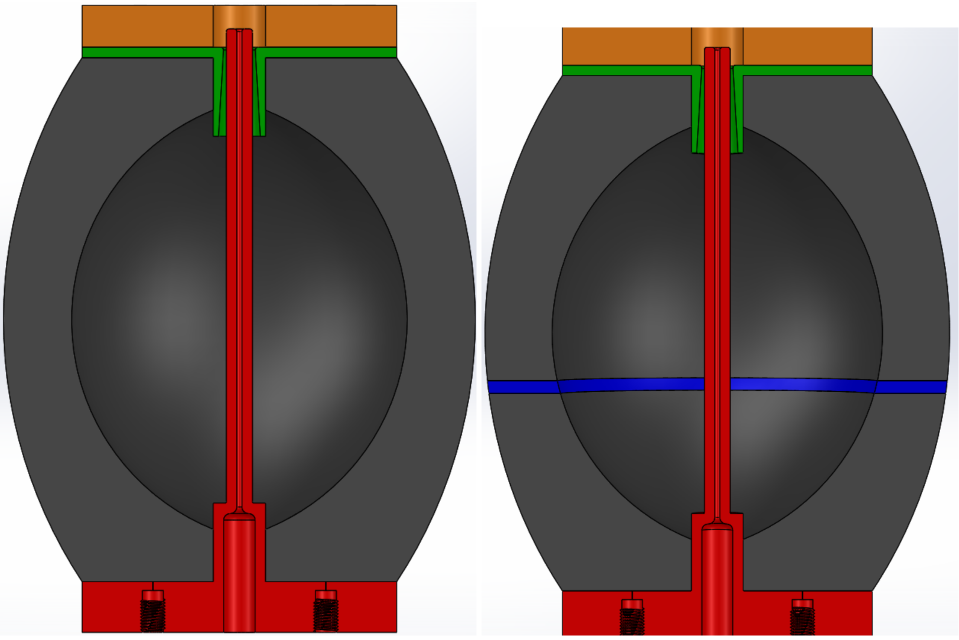

(a) Design 1.0

(b) Design 2.0

Figure 3.7: 3D section view of the shock mount design.

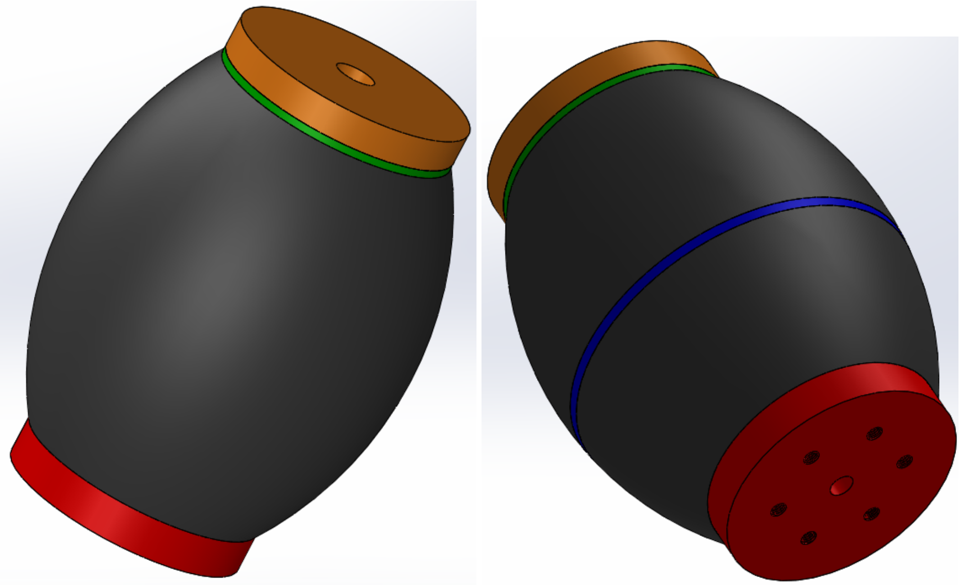

(a) Design 1.0

(b) Design 2.0

Figure 3.8: 3D shock mount design.

This page is intentionally left blank.

4

MODELING SHOCK

4.1. INTRODUCTION

Shock mounts are devices that enhance the ability of a system to withstand and dissipate the shock that strikes it. To design the shock mount it is critical how severe the shock is. Given the intended application, the shocks generated due to an underwater explosion are discussed in this chapter. The impact caused by underwater explosions has been studied ever since it was realized that explosions underwater could be accomplished. Various tests were conducted on ship sections and models of ship sections under different severity of the attack. The sequence of events after an explosion and their responses is discussed.

4.2. SHOCK WAVE

The sequence of events associated with the shock wave is discussed in Sec. C.2. The shock is experienced at a given point away from its origin is considered. At a fixed location the pressure history begins with an instantaneous pressure increase to peak pressure p_0 in less than 10^{-7} seconds. This is followed by a decay that is initially approximated by an exponential function shown in Eq. 4.1. Fig. C.2 shows the pressure-time curve after the shock wave has passed through a particular location.

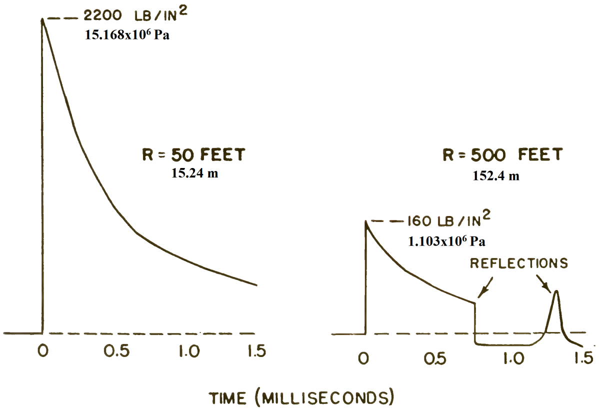

Figure 4.1: Shock wave pressure-time curves at 2 locations from a 300 pound (136 kg) TNT charge[4].

$$p(t) = p_0 e^{-t/\theta} \tag{4.1}$$

where θ is the decay time $\forall 0 \leq t \leq \theta$.

The velocity of propagation depends on the peak pressure of the shock wave. For most practical purposes the velocity is approximately 5000 fps (1524 m/s) [5]. For pressures up to 10,000 psi (68.947×10^6 Pa), the velocity is linearized as,

$$C = c \times (1 + 8.7 \times 10^{-10} p_0) \tag{4.2}$$

where c(m/s) is the velocity of sound in the medium and p_0 is in Pa.

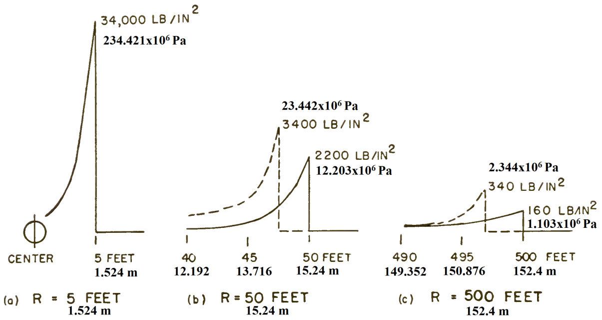

Figure 4.2: Pressure distribution around a 300 pound (136kg) TNT charge at 3 locations after completion of detonation[4].

The pressure distribution behind a plane shock front at large distances from the explosion is given by Eq. 4.3.

$$p(x) = p_0 e^{-x/c\theta} \tag{4.3}$$

The size of the explosive charge and standoff distance from the charge at which the pressure is measured modulates the peak pressure p_0 and the decay constant θ. For TriNitroToluene (TNT), it holds that,

$$p_0 = 52.4 \times 10^6 \left(\frac{W^{1/3}}{R}\right)^{1.18} \qquad ,\text{Pa} \tag{4.4}$$

$$\theta = 0.084 W^{1/3} \left(\frac{W^{1/3}}{R}\right)^{-0.23} /1000 \qquad ,\text{sec} \tag{4.5}$$

where charge weight W is in kg of TNT and standoff R is in m. Fig. 4.2 depicts the shock wavefront that would be experienced at different locations from the charge. The dotted line represents the wavefront if the shock wave was propagated as an acoustic wave.

These equations describe the shock wave sufficiently except in the immediate vicinity of the explosive charge. In the immediate vicinity, the peak pressure is higher than what is predicted[5].

Cole[4] and Keil[5] have performed a detailed study in Underwater explosions presenting the sequence of events, modeling, measurement, effects, and damage.

4.3. MODELING THE SHOCK WAVE

Surface ships and submarines have different responses for an underwater shock-wave. In this study, we consider only Surface ships. They primarily move in an upward direction, no matter where the charge is located or explosion has occurred underwater. When the plating structure of the ship is incident with a shock wave, a proportion of energy is transferred to the plate, while the remaining portion is reflected[11]. The proportion of energy transferred to the plate depends on several factors, such as the cosine of the angle of incidence (α) of the incoming shock-wave w.r.t the plate and water backing of the plate. When the ballast tanks, which are used in stabilizing the ship are just under half full then the ideal situation for low shock damage exists. The free surface of the water allows for the dissipation of the shock-wave and the large fluid bulk absorbs any reflected waves. Bottoming of equipment (reaching the lowest point before stabilizing) might occur because of subsequent bubble pulses if the equipment response is out of phase with its base motion. Below mentioned theories are formulated for air-backed plates under an incident shock-wave[11].

4.3.1. TAYLOR FLAT PLATE EQUATION

Taylor flat plate theory is used to determine the dynamic response of hull plating to a shock wave caused by an underwater explosion. It does not model the fluid explicitly and is a simplified fluid-structure interaction equation. In this section, the final equation is provided and discussed. The complete derivation of the equations is provided by Mathew[28].

The translational velocity of the hull in the vertically upward direction at time t after an incident pressure wave of peak pressure (p_0) strikes the hull is given by [28][11].

$$V_s(t) = \frac{2p_0\theta}{m_p(1-\beta)}\left[\exp\left\{-\left(\frac{\beta t}{\theta}\right)\right\} - \exp\left\{-\left(\frac{t}{\theta}\right)\right\}\right], \tag{4.6}$$

where $m_p = \frac{M}{A}$ is the mass per unit area (here M is the mass of the ship, A is the area of the hull that touches the water), p_0 is the peak pressure obtained in Eq. 4.4, θ is the decay constant as computed in Eq. 4.5. β is a constant as defined in[28].

$$\beta = \frac{\rho c\theta}{m_p cos\alpha}, \tag{4.7}$$

here, ρ is the density of seawater, c is the speed of sound in seawater and alpha is the angle of incidence (i.e angle between the normals of the flat surface and wavefront).

The Peak Translational Velocity (PTV) (V_s^{max}) is the overall maximum velocity impaired on the ship by a shock-wave. This can be obtained by differentiating Eq. 4.6, and equating it to zero to get the rise-time (t_{max}) at which PTV is attained, substituting this t_{max} back in Eq. 4.6 gives PTV. Equations to determine t_{max} and V_s^{max} is derived and shown in Eq. 4.8[28].

$$\begin{aligned} V_s^{max} &= \frac{2P_0\theta}{m_p}\beta^{\frac{\beta}{1-\beta}} \\ t_{max} &= \theta\frac{ln(\beta)}{\beta-1} \end{aligned} \tag{4.8}$$

4.3.2. ATTACK SEVERITY

It is important to determine the relationship between shock velocity, geometry, and attack severity, as ships can be subject to a large variety of underwater explosions like the variation in charge, standoff, and relative attack geometry. The energy density of the arriving shock wave (Maximum Shock Factor [MSF]) at the ship's hull is used to describe the attack severity for high explosive charges, as given in Eq. 4.9. Angle function ($f(\alpha)$) is used to describe the effect of angle of incidence in determining attack severity, as given in Eq. 4.10[5].

$$\text{MSF} = \frac{W^{1/2}}{R} \tag{4.9}$$

$$f(\alpha) = \eta + (1-\eta)cos(\alpha) \tag{4.10}$$

Shock velocity on board the ship is determined by Eq. 4.11, as a function of shock signature (showing the typical variation of velocity with time) using Eq. 4.6[5].

$$V = SF \cdot V_s(t) \tag{4.11}$$

$$\text{where, } SF = C \cdot MSF \cdot f(\alpha) \tag{4.12}$$

where SF is the shock factor, C is a constant which depends on ship type, location aboard the ship, and type of installation.

A small charge positioned close to the hull may provide the same *SF* as that of a large charge positioned further away. But, the large charge will result in more damage, as it will have a longer impulse time. Whereas the smaller charge will produce greater accelerations, due to the increased peak pressure of the shock-wave when it strikes the hull[11].

The final velocity (V) relation which gives the velocity-time response of the ship under a shock wave is given in Eq. 4.13.

$$V = SF \cdot \frac{2p_0\theta}{m_p(1-\beta)}\left[\exp\left\{-\left(\frac{\beta t}{\theta}\right)\right\} - \exp\left\{-\left(\frac{t}{\theta}\right)\right\}\right] \tag{4.13}$$

Displacement (U) time response experienced by the ship under a shock wave is determined by integrating Eq. 4.13 w.r.t time, and is given in Eq. 4.14.

$$U = SF \cdot \frac{2p_0\theta^2}{m_p(1-\beta)}\left[\exp\left\{-\left(\frac{t}{\theta}\right)\right\} - \frac{\exp\left\{-\left(\frac{\beta t}{\theta}\right)\right\}}{\beta}\right] + C_0 \tag{4.14}$$

where C_0 is the constant of integration determined to be $C_0 = \frac{-2P_0\theta^2}{mp(1-\beta)}\left(1 - \frac{1}{\beta}\right)$.

Acceleration (A) time response experienced by the ship under a shock wave is determined by differentiating Eq. 4.13 w.r.t time, and is given in Eq. 4.15.

$$A = SF \cdot \frac{2p_0\theta}{m_p(1-\beta)}\left[\frac{1}{\theta}\exp\left\{-\left(\frac{t}{\theta}\right)\right\} - \frac{\beta}{\theta}\exp\left\{-\left(\frac{\beta t}{\theta}\right)\right\}\right] \tag{4.15}$$

Acceleration (A) frequency response experienced by the ship under a shock wave is determined by taking the Fourier transform of Eq. 4.15 and is given in Eq. 4.17. Relation Eq. 4.16 is used for this Fourier transformation.

$$g(t) = \exp\{-a|t|\} \Leftrightarrow G(\omega) = \frac{a}{a^2+\omega^2} \Leftrightarrow G(f) = \frac{a}{a^2+(2\pi f)^2} \quad \forall a \geq 0 \tag{4.16}$$

$$\hat{A}_f(f) = SF \cdot \frac{2p_0\theta}{m_p(1-\beta)}\left[\frac{1}{\theta}\frac{2a_1}{a_1^2+(2)^2)} - \frac{\beta}{\theta}\frac{2a_2}{a_2^2+(2\pi f)^2}\right] \tag{4.17}$$

where, $a_1 = \frac{1}{\theta}$ and $a_2 = \frac{\beta}{\theta}$

4.3.3. SHOCK LOADING VALUES

In order to obtain representative shock data for the shock mount design cases, shock loading values of displacement, velocity, and acceleration are computed for the following parameter values:

- Density of Sea Water : $\rho = 1025\ \mathrm{kg/m^3}$
- Speed of Sound in Water : $c = 1500\ \mathrm{m/s}$
- Mass of Explosive : $W = [125, 250, 500]$ kg (For Reference: Mark 48 torpedo -> 290kg)
- Distance to Rigid Plate / Stand Off Distance : $R = 10$ m
- Mass of Ship : $M = 3000$ Tons $= 3000000$ kg (Approx Reference: HNLMS Holland (P840) -> 3300 Tons)
- Area of Hull : $A = 1500\ \mathrm{m^2}$ (Approx Reference: HNLMS Holland (P840))

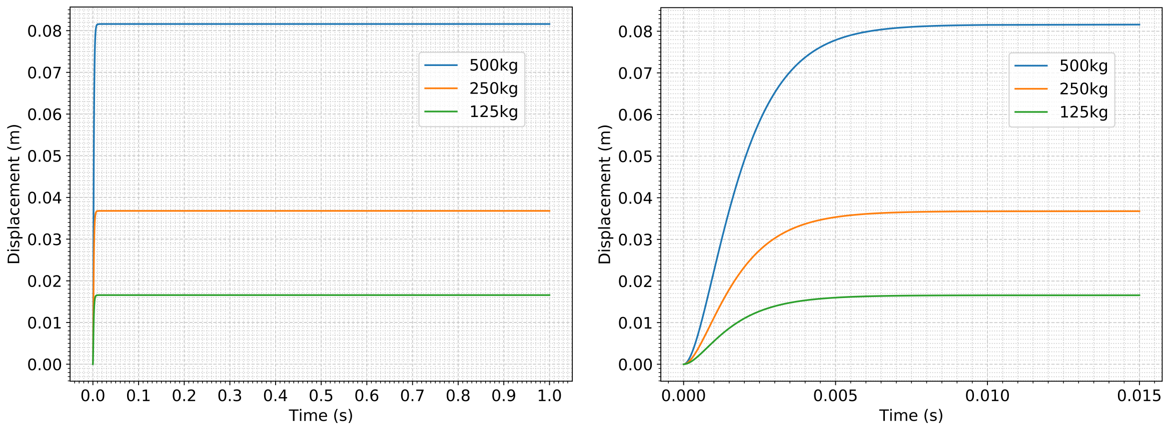

(a) Displacement (b) Magnified Displacement

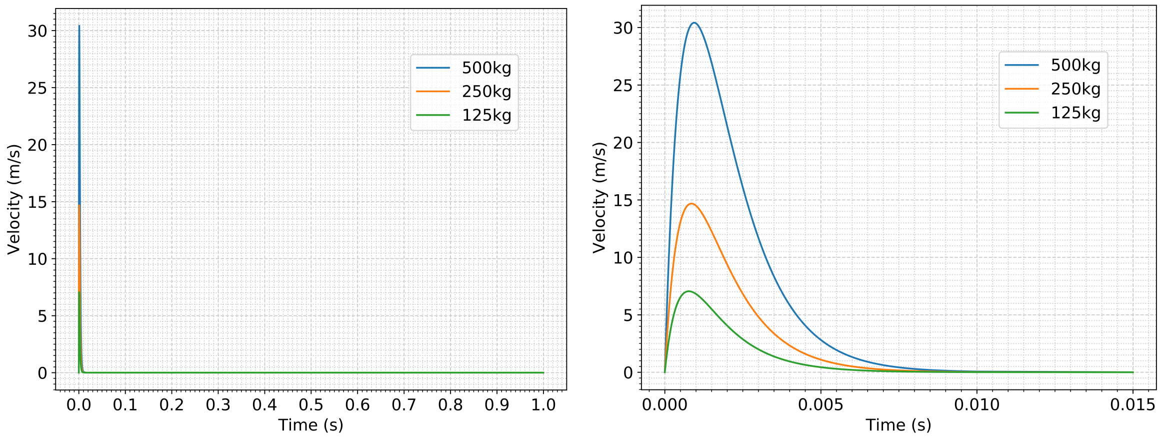

(c) Velocity (d) Magnified Velocity

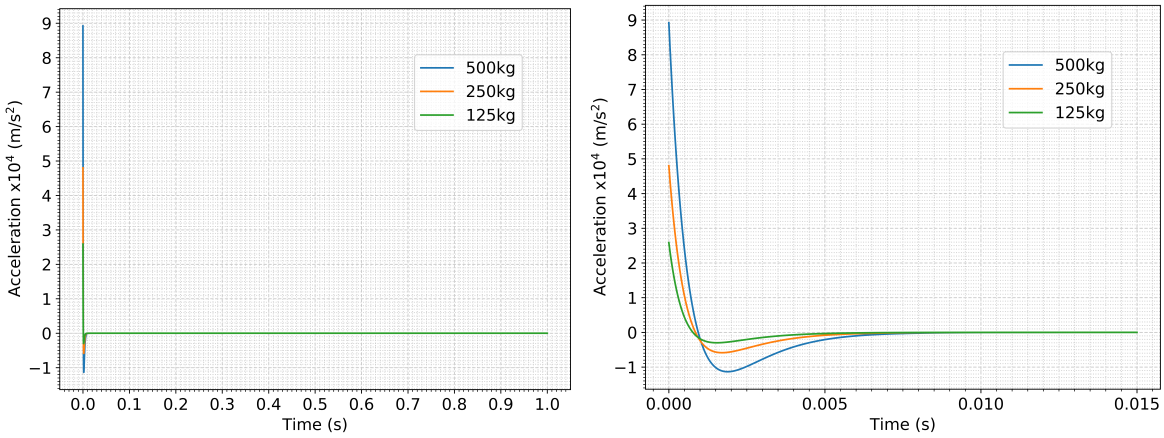

(e) Acceleration (f) Magnified Acceleration

Figure 4.3: Time response of the ship for a time of 1s and Magnified time response of the ship, where maximum change in plot takes place.

DISPLACEMENT

Displacement (U) time response experienced by the ship under a shock wave is plotted in Fig. 4.3a for three different mass of the explosive (W) (125,250 and 500 kg) for a time period of 1s. The second plot, in Fig. 4.3b, is magnified to the region where maximum change occurs.

An experimental displacement time response of the ship's hull during an underwater explosion event is shown in Fig. 4.4. Clearly, the analytical plots of Fig. 4.3a and Fig. 4.3b are approximations of the shape/-nature of the curve. But the maximum amplitude of the shock is well described by the analytical relation, the decrease in the displacement after the maximum amplitude is not well described. This is the approximation made in the modeling of the shock load.

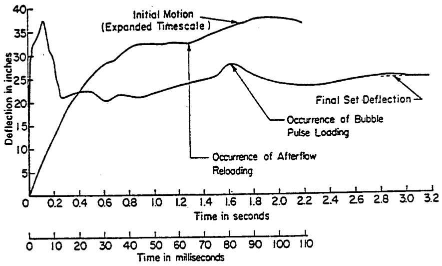

Figure 4.4: Experimental displacement of the hull plating during an underwater explosion event[5].

VELOCITY

Velocity (V) time response experienced by the ship under a shock wave is plotted in Fig. 4.3c for three different mass of the explosive (W) (125,250 and 500 kg) for a time period of 1s. The second plot, in Fig. 4.3d, is magnified to the region where maximum change occurs.

ACCELERATION

Acceleration (A) time response experienced by the ship under a shock wave is plotted in Fig. 4.3e for three different mass of the explosive (W) (125,250 and 500 kg) for a time period of 1s. A maximum acceleration of $89209.51 m/s^2$, $48027.62 m/s^2$, and $25856.57 m/s^2$ is experienced by the ship for 500kg, 250kg, and 125kg of explosive mass respectively. The second plot, in Fig. 4.3f, is magnified to the region where maximum change occurs.

Acceleration $(\hat{A}_f(f))$ frequency response experienced by the ship under a shock wave is plotted in Fig. 4.5 for three different mass of the explosive (W) (125,250 and 500 kg) for a time period of 1s.

These plots can be compared with the results of Chapter 8, to understand the performance of the shock mount.

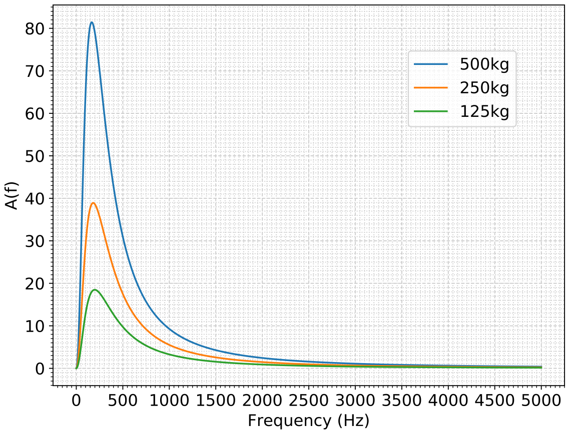

Figure 4.5: Plots showing the acceleration frequency response of the ship for a upto a frequency of 5000Hz.

5

Finite Element Modeling

5.1. Introduction

Now the solution structure of the problem can be formulated, loading as discussed in Chapter 4 can provide the required external load, this external loads can be converted to stresses using equilibrium equations discussed in this chapter, the material equations discussed in Chapter 2 helps to determine strain from the known stress. The strain is then applied to the geometry shown in Chapter 3 to come up with the deflections(continuity). Force to stress to strain(deformation) to deflection is the reversible procedure to solve any mechanics problem. Such a problem can be expressed in terms of a Partial Differential Equation(PDE) and the solution to the problem is the solution of that PDE. For most geometries analytical methods can not be used to solve PDEs and approximations are made to solve such PDEs. The Finite Element Method (FEM) is one such approximation which discretizes the geometric space into known subspaces on which the PDEs are solved numerically. Fundamentals of FEM and its implementation for nonlinear elastomeric systems can be found in textbooks[29] [30]. FE aspects that are specifically relevant to elastomeric shock mounts are discussed in this chapter.

5.2. Solution Methods

There are two solution methods to solve semi-discretized FE equations, explicit time integration, and implicit time integration. Explicit FEM uses just the current state to calculate the state of a system at the next timestep. Implicit FEM uses an equation containing both the current and later states of a given system to find the solution. Customer presentation from Ansys [6] prefers an explicit method for problems with very low time magnitude and high nonlinearity as shown in Fig. 5.1. Explicit time integration is best suited for blasts, high-speed impacts, buckling, drop, and severe structural deformation. More on governing equations and in-detail working of the solver can be referred to Chapter D.

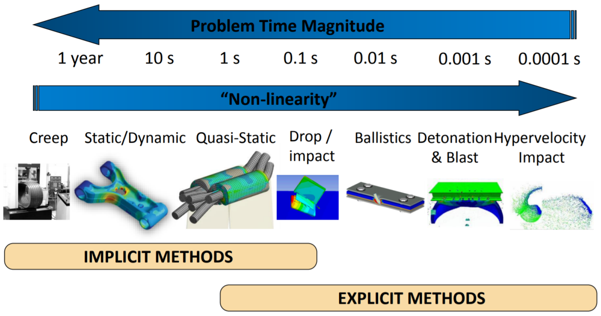

Figure 5.1: Applications for Implicit and Explicit time integration [6].

5.3. FINITE ELEMENT IMPLEMENTATION

Multiple Finite Element packages, such as Abaqus and Ansys, are commercially available to solve the problem in hand. It is not straight-forward in Ansys to combine a 2D static implicit (for steady-state gravity loading) and a 2D explicit dynamic (Autodyn explicit solver) study (used to apply the blast impact load), which is needed to solve the given problem. When it was attempted to solve the static gravity loading problem with a transient analysis, it did not stabilize even when analyzed for a large time, hence both static and dynamic analysis procedures are required. The semi-Implicit method is available in Ansys, which is a solution scheme in which the analysis starts out using an implicit solution method but transitions to an explicit solution method when the implicit solution fails to converge. It is recommended for problems that cannot converge in the implicit solution for a brief period due to extreme nonlinearities. For example, models with local buckling, snap-through problems, analyses in which temporary rigid body modes are activated, and models with sudden changes in material constitutive behavior can all benefit from the semi-implicit method[31]. Whereas the problem in hand is completely nonlinear loaded for a very short period. The response after initial peak loading also undergoes large deformations and buckling, hence a complete explicit study is preferred. It is also not straight forward to implement python programming and automation of the analysis in Ansys, because Ansys uses IronPython which makes it hard to use standard python libraries. This also makes it difficult to implement user-defined optimization algorithms in Ansys, forcing the user to use the inbuilt ones. Abaqus FE package is chosen as the best candidate for solving the problem, as it overcomes all the mentioned drawbacks of Ansys. Setting up of the FE model and execution of the analysis in Abaqus is discussed in the following sections.

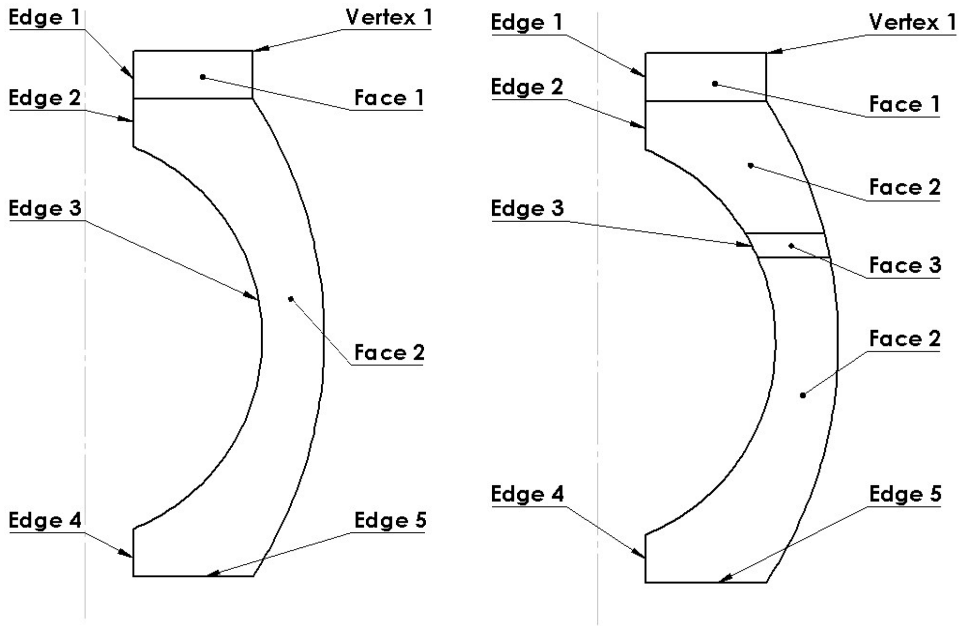

(a) Design 1.0

(b) Design 2.0

Figure 5.2: Sketch of the axi-symmetric model with faces and edges.

5.3.1. CAD MODELING

The parameterized geometry of the shock mount is modeled in Abaqus using the inbuilt "Parts" module. A python script is written to automate the generation of the geometry for feasible parameter values shown in Fig. 3.2 and Fig. 3.3. The modeling space is chosen to be axisymmetric and modeled as a deformable body using the shell base feature. The outer edges, as shown Fig. 5.2, are sketched using lines and arcs to form a closed loop, then the shell face is generated. The inner geometric features are then implemented using face partition. This allows for multiple faces in the geometry to accept different material properties. If each face is defined as an individual part, the user needs to define interactions (constraints) to connect faces, face partition helps avoid this step. The modeling of the geometry in 3D is described in the next subsection.

CAD MODELING IN 3D

The sketch of 3D geometry is similar to that of 2D. The modeling space in the "Parts" module is chosen to be 3D and modeled as a deformable body. The solid base feature of type revolution is used to generate the solid model. This is done to generate geometry analogous to the 2D axisymmetric model. The 3D solid is defined as "Cell" in Abaqus. Partition of inner geometric features is done using "Partition Cell By Plane Point Normal". The partition is created along the plane, whose orientation is defined by its normal vector (Edge 1) and location in 3D space defined by a point (Any point in the intersection of Edge 1 and Edge 2).

5.3.2. MATERIAL PROPERTIES

The material properties are defined on the partitioned faces of the geometric model. A homogeneous solid section is created for each face on which corresponding material properties are applied.

For Design 1.0 and Design 2.0: The objective mass, i.e Face 1 in Fig. 5.2a and Fig. 5.2b, is modeled using structural steel, with a density of 7850 kg/m^3, Young's modulus of 200 GPa, and Poisson's ratio of 0.33.

For Design 1.0 and Design 2.0: The shock mount, i.e Face 2 in Fig. 5.2a and Fig. 5.2b, is modeled with Neoprene hyperelastic material. Polynomial order 3 hyperelastic model with the material coefficients and properties as discussed in Sec. 2.3.2 is used to model Neoprene. The density of Neoprene material is taken to be 1230 kg/m^3.

For Design 2.0: The metallic interface, i.e Face 3 in Fig. 5.2b, is applied with structural steel with material properties equivalent to Face 1.

MATERIAL PROPERTIES IN 3D

For a 3D geometry, the material properties are applied to corresponding cells, instead of faces in the 2D geometry.

5.3.3. STEP

The step definition contains the type of analysis to be performed, solution output requests, and restart requests. The analysis of both designs, Design 1.0 and Design 2.0, is split into two. The first analysis is an implicit static (Abaqus/Standard, Static General) analysis. This brings the system into static equilibrium with the gravity body load. The second one is an explicit dynamic analysis, where the system is loaded under the shock load as discussed in Sec. 4.3.3. For both designs, the steps remain the same. But, unfortunately when an implicit step is added, then an explicit step cannot be added in the same model/analysis. The best way to make this possible is to split the analysis into two separate models, first an implicit model followed by a separate explicit model. An analysis restart is used to connect these models/steps.

IMPLICIT STATIC

Due to large displacements experienced during the study, and due to the presence of material nonlinearity, a nonlinear static analysis is performed. In the static implicit analysis, the gravity load of 9.81 m/s^2 is gradually added to the system using a ramp function, for a pseudo-time period of 0 to 0.8. At time 0.8 the system reaches equilibrium, but contains nonzero velocity, due to the motion it went through. There is no acceleration because the static analysis does not consider inertia into account. To make the velocity at the end time zero, the ramp is leveled off using a constant function of gravity load from the period 0.8 to 1.0. So, the static implicit study has two steps, one with a ramp function and the other with a constant function of gravity load. Here, in the static study, it is to be noted that the time has no unit. Time is used in the static analysis to cross-reference the amplitude, which can then be used to define loads, load increments, and change other parameters during the study.

Solution Technique: The Newton's method is used in Abaqus/Standard to solve nonlinear equilibrium equations. The full Newton and quasi-Newton methods are available as the solution technique. The full newton computes the stiffness / Jacobian matrix (tangent to the force-displacement curve) at every iteration, this makes it costly. Whereas quasi-Newton calculates the stiffness/ Jacobian matrix using an iteration process. The trade-off between the two being, quasi-Newton takes more iterations to converge compared to Newton for a highly nonlinear problem. Although this saves time in computing and solving the Jacobian, residual evaluations, and the arithmetic involved might make it costly for highly nonlinear problems. Hence, practically even though using quasi-Newton is more economical, it cannot be justified over full Newton for a highly nonlinear problem. It is recommended to use the Full Newton study, as the analysis is highly nonlinear.

Incrementation: The solution to nonlinear equilibrium equations is usually obtained in a series of increments, as the problems involve history-dependent responses. To ensure correct modeling of history-dependent effects, the increments must be kept small. More iterations are required if the increments are too large, the computational efficiency of the problem determines the optimal increment size. Above all, using a larger increment may not end up in any solution if the initial state is too far from the sought equilibrium state. This is because Newton's method has a finite radius of convergence and the sought equilibrium state might lie outside that, hence the increment size has an algorithmic restriction.

In Abaqus/Standard, an automatic incrementation scheme is chosen. It is the recommended option and it chooses the increment size based on the computation efficiency. This scheme asks for an initial, minimum, and maximum increment size. For our study after multiple iterations initial increment of 0.1, a minimum increment of 10^{-8}, and a maximum increment of 0.2 are used. For the maximum number of increments, the default value of 100 is used.

RESTARTS

Restart allows continuing a previous analysis with a new analysis. This is usually used to split the analysis over steps and extract intermediate results. This procedure also helps in continuing a failed lengthy analysis from the last restart point, removing the need to rerun it completely, saving time. It is not possible to include new geometry and change mesh in the new analysis, because additional steps are a continuation of what is done before.

To analyze an explicit dynamics simulation after an implicit static analysis, a restart is requested. For this analysis, restart is requested in the last step of implicit static analysis with a frequency of 1. The output of this restart is written to a .res file, which can be used to restart the analysis. The analysis is continued in the explicit dynamics model by specifying the restart as an "initial state" in the "predefined field" under the "load" module. This connects implicit with explicit analysis.

EXPLICIT DYNAMICS

Due to large displacements experienced during the study, and due to the presence of material nonlinearity, a nonlinear explicit dynamic analysis is performed. In this analysis, the system is analyzed for a time period of 1 second. From Chapter 4, it can be noticed that the actual shock loading takes place only up to 0.01 second, thereafter the system response to the actual shock is observed up to 1 second. Simulation trials were conducted for higher time periods and 1 second was chosen as the optimum period of observation. As discussed in Sec. 2.4, the linear and quadratic bulk viscosity parameters are chosen to be 0.06 and 1.2 respectively.

Incrementation: In Abaqus explicit, it is advised to use Automatic time increment. A global stable increment estimator is chosen to determine the stability limit as the step proceeds. In the global estimation algorithm, the current dilatational wave speed is used to determine the maximum frequency of the entire model. The other algorithm available is Element-by-element, whose estimate is conservative and provides a smaller stable time increment to the true stability limit. This is because it uses the highest element frequency in the whole model to determine stability. The effectiveness of the global estimation algorithm is monitored, and if the computational cost is more than its benefit, the program shifts to element-by-element estimates to save computational time. Time increment provided by Abaqus algorithms can be modified using a scaling factor, which is set to 1 by default. The equations involved in determining the explicit time increment is given in Sec. D.3.1.

FIELD OUTPUT REQUESTS

Acceleration of the objective mass and von Mises stress observed in the shock mount and metal interface are the two important results from this analysis. Both these results are extracted at suitable intervals, which is determined using a sampling frequency study as shown in Sec. 7.1.

5.3.4. MESHING

The CAD part model is meshed using the Abaqus mesh module. Because restart is used and there is an interface between two models, the mesh used in the static implicit model and explicit dynamic model should be the same. The solution is compared using implicit and explicit quadrilateral mesh for the implicit analysis and results were observed to be similar.

The complete geometry of Design 1.0 and Design 2.0 is meshed using CAX4R Explicit Element. CAX4R is a first-order axisymmetric (CAX), 4-noded (4) solid element with reduced-integration (R). The element type is chosen as quad with enhanced hour-glass control. Under the mesh generation controls, the element shape is chosen to be Quad (Quadrilateral) to force all the elements to be CAX4R and a structured mesh control technique is requested. If Quad is not chosen explicitly in mesh controls, some elements might be Tri (Triangular), which changes the element to CAX3. Mesh sizes used for different faces along with a mesh convergence study is shown in Sec. 7.2.

MESHING IN 3D

Meshing the part in 3D is not as straight-forward as in 2D. When the complete part without modification is used, a full hexahedral mesh is not generated and few tetrahedral elements accompany it. Therefore the part needs to be partitioned to create a quality uniform hexahedral mesh. The part has its centerline along the y-axis and a revolution along the y-axis as discussed earlier. The part is partitioned along the XY and YZ plane dividing the whole part further into 4 sections (The final part has 8 sections in Design 1.0 and 14 sections in Design 2.0, along with the partitions defined earlier for objective mass and metal interface and is shown in Sec. D.4).

The complete geometry of Design 1.0 and Design 2.0 is meshed using C3D8R Explicit Element. C3D8R is a 3D stress (3D), 8-noded (8) linear brick element with reduced-integration (R). The element type is chosen as Hex with enhanced hour-glass control. Under the mesh generation controls, the Hexahedral element shape (Hex) with a mesh sweep technique is used to generate a complete Hex mesh of type C3D8R. An advanced front algorithm with a mapped mesh is used to create a quality mesh. This algorithm generates Hex elements at the boundary and systematically generates Hex elements as it moves systematically to the interior of the geometry. This creates a structured mapped mesh at the boundaries making load transfer into the geometry uniform.

Other mesh parameters for 3D remains similar to that of 2D, the difference being faces turn into cells (Volume).

5.3.5. INTERACTIONS

The general contact property is defined using two interaction properties. The first interaction property of tangential behavior is approximated to be frictionless. The second interaction property of normal behavior is taken to be hard and separation after contact is allowed. For the static implicit and explicit dynamic study, general contact standard and general contact explicit are applied respectively. The contact property is applied to the complete surface domain including self contact valid across all steps.

REFERENCE POINTS AND RIGID BODY

There is no need to extract the stress information from the objective mass. This can be done by modeling the objective mass as a rigid body. The objective mass is applied with a rigid body constraint. This process will request for a reference point, where the Center of Gravity (CG) is located. As the analysis is approximated as an asymmetric model, the x-coordinate of the CG is located along the center axis/axis of revolution (x=0, z=0) and the y-coordinate is the geometric center y-coordinate of the rectangular mass. This makes the objective mass to move along the y-axis without any rotations w.r.t z-axis.

5.3.6. BOUNDARY CONDITIONS AND LOADS

The boundary conditions (BC) and loads are the important aspects of the analysis, which drives the solution. Abaqus uses the "findat" function when defining BC and loads. In a dynamic simulation "findat" can create a lot of ambiguity and confusion during run time in determining the correct edges. Therefore it is wise to apply edge BC and loads at the nodes rather than using the line geometry. This can be achieved by defining the nodes at the application of BC and loads using sets, as defined in the next section.

DEFINING SETS

The Edge 5 geometry in Fig. 5.2 is saved as an edge and the corresponding nodes are extracted after the meshing to form a node-set. This set is named as SupportNodes. The nodes of Edge 2, Edge 4, and Edge 5 geometry in Fig. 5.2 are combined to form a node-set and is named SideNodes. The Vertex 1 geometry in Fig. 5.2 is extracted as a node and its node number is saved as a node-set named AccNode.

ASSIGNING BC TO NODE SETS

Every node in the 2D axisymmetric models has 3 Degrees Of Freedom (DOF); u1=ux is the displacement component along the x-axis, u2=uy is the displacement along the y-axis and ur3=urz is the angular displacement about the z-axis.

Static Implicit Analysis The SupportNodes node-set is assigned with zero displacements along the y-axis (u2=0) and all other DOF are left free (u1=UNSET, uz3=UNSET). The SideNodes node-set is assigned with zero displacement along x-axis (supported on the vertical interface as discussed in Sec. 3.5) and zero angular displacement about z-axis (u1=0, ur3=0 , u2=UNSET (frictionless/lubricated as discussed in Sec. 3.5). Because Edge 5 overlaps in both node-sets, SupportNodes and SideNodes, it is constrained in all DOF forming a fixed constraint. This ensures all horizontal interfaces are constrained as discussed in Sec. 3.5. Only one DOF is allowed on the rigid body reference point, discussed in Sec. 5.3.5, allowing it to displace only along the x-axis (u1=0, ur3=0, u2=UNSET). All these BC remain active for all the static steps defined in Sec. 5.3.3.

A gravity load of -9.81 m/s^2 is applied along the y-axis, with a distribution type uniform in the whole body. This ramp loading (0 to -9.81 m/s^2) is created in the first step of static implicit study which is executed for a period of 0.8. The amplitude at the end of the first step is extended for the second step creating a constant magnitude of the load. The reason for this procedure is already discussed in Sec. 5.3.3.

Explicit Dynamic Analysis The boundary conditions applied to the SideNodes and rigid body reference point is similar to the static implicit analysis. A gravity load of -9.81 m/s^2 is applied along the y-axis, with a distribution type uniform in the whole body. The SupportNodes node-set is assigned with the displacement load as a function of time using tabular amplitude. The tabular amplitude is based on the equation Eq. 4.14 and the python code used for this is shown in Sec. C.1. The analysis is performed for varying magnitudes of displacement loads for a time period of 1 second. As the explicit dynamics analysis has only one step for a time period of 1 second, all the BC and loads are applied to this step.

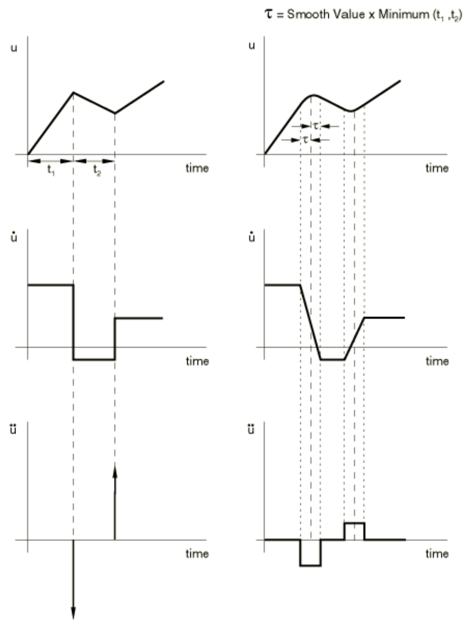

(a) without smoothing (b) with smoothing

Figure 5.3: Piecewise linear definitions with and without smoothing[7].

When defining the displacement time history using a piecewise linear amplitude variation (tabular amplitude definition), its corresponding velocity is a piecewise constant and its acceleration is singular (infinite) at the end of each time interval, as shown in Fig. 5.3(a). This behavior is undesirable. As a solution to this, the piecewise linear displacement is modified into a combination of piecewise linear and piecewise quadratic variations by using the process of smoothing. This ensures continuous variation of velocity in the time period and the acceleration is no longer singular, as shown in Fig. 5.3(b). The Abaqus FEA solver asks for t, the fraction of time interval before and after at each time point to be replaced by a smooth quadratic time variation in a linear time variation. By default, the Abaqus/Standard (Implicit) solver has a t = 0.25, and Abaqus/Explicit solver has a t = 0.0. The Abaqus/Explicit has a default t = 0.0 as finite differences are used to calculate the time derivatives of amplitude curves, hence there is some inherent smoothing in the time discretization.

Boundary Conditions and Loads in 3D

The boundary conditions in 3D are similar to 2D axisymmetric. The loads remain the same. The extra DOF introduced in the 3D analysis is constrained such that they match the behavior of the 2D analysis.

5.4. SOLVER FAILURES

During the course of the performing multiple simulations, various solver failures were observed and solutions are found accordingly. Standard error codes were returned during the analysis to understand the type of failure.

5.4.1. GEOMETRY GENERATION

Due to automation involved in the geometry generation, sometimes failure was observed in the shell face generation. The error was the non-availability of a closed sketch. The data to the command line during execution is given as a string. Inside the python script, this string was type converted back into a float, during this process the variables lose a bit of their precision. This is very uncommon and a fix was not needed in the long run. An attempt to round-off the input parameters was done, but it was found to influence the optimization process significantly.

5.4.2. STATIC FAILURE

The failure during static implicit analysis was due to buckling/bifurcation involved compression. The solver does handle mild bifurcations with a positive load-displacement curve. But at the point of bifurcation multiple positive and negative slopes were found and the solver fails to converge to a solution. To solve this, the Riks method, which is based on the arc length method was used instead of newton. But that analysis comes with its issues. The method back-traced its path at the point of bifurcation, this can be fixed manually by varying the increment radius. But it was found unsuitable for automation of the analysis. In summary, if the analysis fails in the static analysis, it is considered solver failure, and an error code is returned.

5.4.3. DYNAMIC FAILURE

The failure during explicit dynamic analysis can be mostly traced to 2 issues.

The first error is with the deformation speed. "The ratio of deformation speed to wave speed exceeds 1.0000 in at least one element." This is a highly localized error occurring for a very short period. This error can be converted into a warning by modifying the input file, by setting a higher cutoff ratio under the deformation speed check.

The second type of error is due to excessive deformation observed in a few elements of the mesh, and the solver fails to converge to a solution. This error can mostly be fixed by playing with the solver parameters manually. Sometimes by virtue of the geometric shape, there could be some localized load concentrations leading to excessive deformation in a few parts of the geometry. Manually fixing multiple simulations is not feasible in an optimization analysis or a parametric analysis with 100 analysis. Therefore, if the analysis fails in the second type, it is considered solver failure, and an error code is returned. The error codes are then looked-up in the final output to detect the type of failure and determine if it could be solved.

5.5. EXECUTION

The entire FE modeling and analysis are scripted in python, with the help of Abaqus documentation [32] [33], macros, and replay files. Abaqus CAE, in the command line, is used to execute this python script to generate the geometry and setup the FE environment. Abaqus input file is generated at the end of Abaqus CAE execution. This input file, whose solution is the most time-consuming part of the analysis, is then submitted as an Abaqus Job using the command line. This helps in freeing up the Abaqus CAE license. Later the results are extracted using Abaqus CAE and saved as a CSV output. All the individual steps in the analysis are programmed as modules in python and executed parallelly if found effective.

This page is intentionally left blank.

6

OPTIMIZATION METHOD

6.1. INTRODUCTION

In a structural optimization problem, three features of size, shape, and topology can be optimized in a structure. In size optimization, member cross-sectional dimensions are treated as design variables. Shape optimization takes joint coordinates and geometric dimensions as design variables apart from cross-sectional dimensions. The optimum structural shape is obtained as the solution to such a problem. Topology optimization deals with the optimization of the material layout within the shape of the structure[34].

To obtain the optimal solution, optimization algorithms are divided into two, gradient-free method (or Derivative Free Optimization [DFO]) and gradient-based method (which require additional sensitivity information). Analytical gradients are hard to implement but computationally more efficient, whereas numerical gradients obtained using finite difference is easy to implement but computationally expensive[35]. BOBYQA, a gradient-free method is chosen for the current shape optimization problem. Numerical experiments show that Py-BOBYQA is comparable or better than existing general DFO solvers for noisy problems[36].

6.1.1. DERIVATIVE-FREE OPTIMIZATION (DFO)

DFO algorithms are useful when the function evaluations are expensive making finite differencing too costly or when the function evaluations are noisy making an accurate evaluation of derivatives impossible. "Model-Based Methods" are state-of-the-art DFO algorithms, which performs iterative minimization of local models for the objective over the trust-region. The local models are constructed using interpolation. This differs from a classical trust-region method, which uses derivative information to construct local models. Objective values are captured well when using Model-Based DFO solvers [37]. It is also known to have good practical performance over Nelder-Mead (NMSMAX) and Pattern Search (APPSPACK)[38].

6.2. BOUND OPTIMIZATION BY QUADRATIC APPROXIMATION

BOBYQA is an iterative algorithm to find the minimum of an objective function $F(\underline{x}), \underline{x} \in \mathbb{R}^n$, subject to simple bound constraints,

$$\underline{a} \leq \underline{x} \leq \underline{b} \tag{6.1}$$

on the components of the design variable, x. n is the number of design variables.

An user subroutine returns the value $F(\underline{x})$ for any feasible x. Derivative information on the objective function is are not required. Every iteration k of BOBYQA employs a quadratic approximation $Q(\underline{x}), \underline{x} \in \mathbb{R}^n$ to $F(\underline{x}), \underline{x} \in \mathbb{R}^n$. The interpolation points $\underline{y}_j$ are chosen and adjusted automatically. The approximation Q is available at the beginning of the k-th iteration, the interpolation equations have the form

$$Q(\underline{y}_j) = F(\underline{y}_j), \qquad j = 1, 2, ..., m \tag{6.2}$$

Where, m, number of interpolation conditions, is a constant integer from the interval $[n+2, \frac{1}{2}(n+1)(n+2)]$ and k is the iteration number [39][40].

The python implementation of BOBYQA (Py-BOBYQA) determines the step using the trust-region framework and iteratively constructs an interpolation-based model for the objective [41].

6.2.1. GLOBAL OPTIMIZATION

The multiple restart mechanism is used in this method. This method repeatedly re-initializes Py-BOBYQA from the best point found so far but using a larger trust-region radius every time. It is shown with the help of numerical experimentation, restarting the solver when stagnation is detected is an effective and cheap technique to achieve robustness oversampling and regression techniques[39]. Two main types of restart which the algorithm can perform is given below:

- Hard Restart: This procedure resets the trust-region radius to its initial values, and rebuilds the model from scratch. This requires the fresh computation of the interpolation points and is very costly when combined with FE analysis. This is helpful when the objective function has stochastic noise. The stochastic noise is present if the objective function gives different results for the same value of x.
- Soft Restarts: Once a soft restart is initiated, the algorithm moves x_k to a geometrically improving point in the new trust region. Instead of resetting the trust-region radius to the initial value, this allows for the trust-region radius to increase by a constant factor (the default value is 1.1) every time the earlier restart fails to produce a reduction in the objective. Thus the trust region is increased progressively.

6.2.2. OPTIMIZER PARAMETERS

The following parameters used in the current optimization to control the py-BOBYQA optimizer is shown below:

1. 'scaling_within_bounds' is the parameter flag used to indicate the solver whether the algorithm should internally shift and scale the entries of x, such that the variable bounds become $0 \leq x \leq 1$. This is convenient when the bounds on the design variables have different orders of magnitude. In the current optimization study, this flag is set to 'True'.
2. 'objfun_has_noise' is the parameter flag to indicate if the objective function has stochastic noise. The FE solution does not have any stochastic noise and hence this flag is set to 'False'.
3. 'restarts.soft.move_xk' is the flag parameter that determines whether to preserve x_k or move it to the best new point evaluated for soft restarts. In the current optimization study, this flag is set to 'False'. This helps to avoid an abrupt change in the design variable values and provides smoother progress in the design space.
4. 'general.rounding_error_constant' is a parameter to reduce the risk of round off errors. The default value of this constant in BOBYQA is $1e-3$.
5. 'seek_global_minimum' is the parameter flag set to indicate if the solver needs to look for a global minimum. Py-BOBYQA only implements a heuristic method, therefore it does not guarantees it will end up in a global minimum. But, using this flag will help escape local minima, if there are better values nearby. In the current optimization study, this flag is set to 'True'. The methods used to implement this is given in Sec. 6.2.1.
6. When 'objfun_has_noise=False', the default number of interpolation points is set to 2n+1. Which is the rule of thumb, a polynomial of order n can be solved by using 2n+1 interpolation points.
7. The value of initial trust region radius is set to $0.1\big(\max(\|x_0\|_\infty, 1)\big)$.

6.2.3. OPTIMIZER TERMINATION

The Py-BOBYQA optimizer can be terminated using the following conditions.

1. Termination on small objective value: Tolerance is set on the value of the objective function ($f(x_k)$) at any given k^{th} iteration. The analysis terminates if the calculated $f(x_k)$ is below this tolerance. By default the value is -10^{20}, and can be modified using 'model.abs_total'.
2. Termination on slow progress: Three parameters control termination. First, the history up to which the solver needs to check for slow iteration to determine if the current iteration is 'slow' needs to be specified. By default, this value is 5, and can be modified using 'slow.history_for_slow'. In the current

optimization study, this value is set to 2. The threshold set on the decrease in the objective function is the criteria to determine if the current iteration is ‘slow’. By default, this value is 10^{-8}, and can be modified using ‘slow.thresh_for_slow’. In the current optimization study, this value is set to 10^{-4}. The number of consecutive slow successful iterations before termination is the parameter that finally terminates the analysis based on the results of the other two parameters. The default value is 20 x Number of design variables, and can be modified using ‘slow.max_slow_iters’. In the current optimization study, this value is set to 3.

3. Minimum allowed value of trust-region radius can be used to flag a successful termination. By default, this value is 10^{-8} and can be modified using ‘rhoend’. In the current optimization study, this value is set to 10^{-4}.
4. The optimization can be terminated when the maximum number of iterations set is reached. This is the final termination condition when every other condition fails. The default value is min(100(n+1),1000)), where n is the number of design variables and can be modified using ‘maxfun’. In the current optimization study, this value is set to 100.

6.3. VALIDATION

A nonsmooth minimization objective function, as shown in Eq. 6.3, with multiple local optima is used to validate the Py-BOBYQA optimizer. It is a bounded optimization problem with bound $0 \le x, y \le 50$ on the two design variables.

$$f = \underbrace{\min}_{0\le x,y\le 50} \left(\frac{(x-25)^2 + (y-25)^2 + \sin\big((x-25)^2 + (y-25)^2\big)}{1000} \right) \tag{6.3}$$

(6.4)

here, the objective function is normalized with a factor 1000. The plot of the objective function over the entire design space is shown in Fig. E.1.

Analytically the minimum of the objective function is zero and exists at $(x, y) = (25{,}25)$. The minimum objective function values and optimized design variables obtained while using different optimization algorithms is compared in Tab. 6.1, Tab. E.1, Tab. E.2, Tab. E.3, when the optimization algorithm is initialized from multiple points respectively. For all the algorithms studied the termination tolerance threshold on the design variables is set at 10^{-}6 for equal comparison.

Algorithm	No. Of Fn. Eval.	No. Of Iter.	f$_{min}$	x_{min}
Py-BOBYQA	45	2	4.46e-13	[25.00001105 24.99998996]
BFGS	56	3	5.42e-09	[24.99887914 25.00120598]
Nelder - Mead	194	103	1.52e-16	[24.99999987 25.00000024]
Powell	88	4	0.0	[25.0 25.0]
COBYLA	77	1	3.32e-11	[24.99991988 25.00010102]

Table 6.1: Initial Point: [0,50]

6.3.1. DISCUSSION

From the comparison tables of Tab. 6.1 and Tab. E.1, Tab. E.2 it can be inferred that the Py-BOBYQA algorithm outperforms other algorithms for the given optimization problem. It requires the least number of function evaluations and hence saves on computation cost. The accuracy of the optimal design point is also comparable to the analytical results given the tolerance on the design variables. But, it is also interesting to notice from Tab. E.3 that the algorithm even though performs better, loses to other algorithms when starting the optimization from the optimal point. This is because the optimizer seeks a global minimum and hence searches more in the design space. The overall performance of Py-BOBYQA is satisfactory when working with nonsmooth surfaces which is locally non-convex and can be used in the shape optimization of structural shock mounts.

This page is intentionally left blank.

7

FINITE ELEMENT VERIFICATION AND PERFORMANCE

The objective of this section is to determine the critical FE parameters using convergence studies and verify their performance. This chapter covers two convergence studies. The first study gives the optimum rate at which the analysis results need to be sampled. The second study gives the optimum mesh size for different faces in the geometry. The study begins with the setting up of the environment and ends with a discussion on the results. The results shown here are the final results obtained after once cycle iteration, that is the sampling convergence study is performed with the optimal mesh size and the mesh convergence study is performed with the optimal number of sampling points.

7.1. SAMPLING CONVERGENCE STUDY

It takes around a million iterations to solve the problem and it is inefficient to store the data at all iterations. Storing the results at an iteration involves processing time and memory which significantly influences the analysis time. Therefore results need to be sampled at suitable intervals for it to be accurate and precise. This study was undertaken as initial mesh convergence results were highly non-smooth and the smoothness of the curves improved significantly after this analysis.

7.1.1. RESULT EXTRACTION

Acceleration of the objective mass and von Mises stress observed in the shock mount and metal interface are the two important results from this analysis.

ACCELERATION

The acceleration needs to be determined in the objective mass. As the objective mass is modeled as a rigid body with the reference point at the center of mass, the whole objective mass experiences the same acceleration. That is all the nodal points in the mesh of the objective mass experience the same acceleration. Hence it is sufficient to extract the results from any one node in the objective mass, it is good to save this node as a node-set which makes result extraction easier. This saves disk space and makes the analysis faster as the time taken to transfer the results is minimized. In the output variables section, Translational Acceleration (AT) is chosen as the field variable.

STRESS

The stress experienced by the shock mount is the limiting constraint in the design and optimization of the shock mount, and this needs to be obtained for Design 1.0 and Design 2.0, and also the metal interface for Design 2.0. Both these faces are made into individual sets and a separate field output is requested for individual faces. In the output variables section, von Mises stress (MISES) is chosen as the field variable.

In the field output requests, the set domain is chosen with output at approximate times. The frequency is chosen to be evenly spaced time intervals and this number of intervals (numIntervals) parameter is swept in python from 1000 to 20000 for determining the optimum parameter value. The result of the sweep is shown in the next subsection.

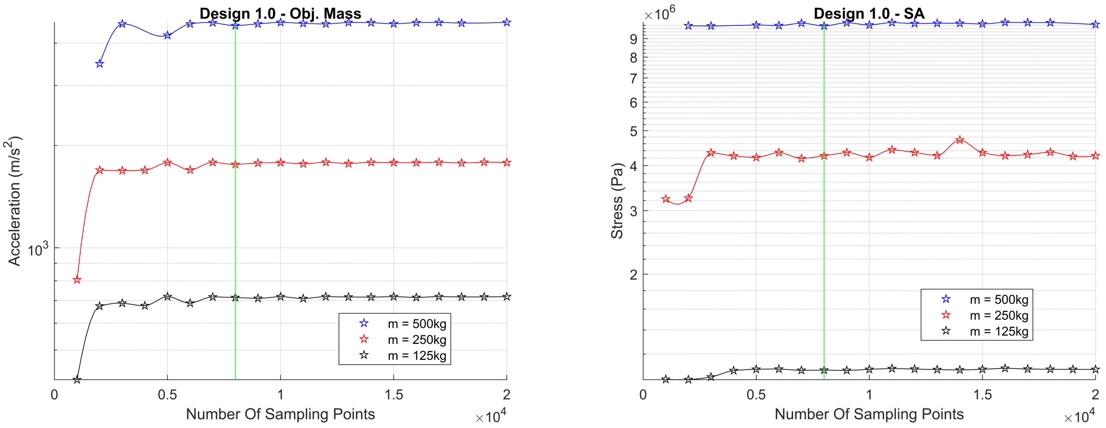

(a) Acceleration of objective mass (b) von-Mises stress in the shock mount

Figure 7.1: Sampling frequency convergence for Design 1.0 .

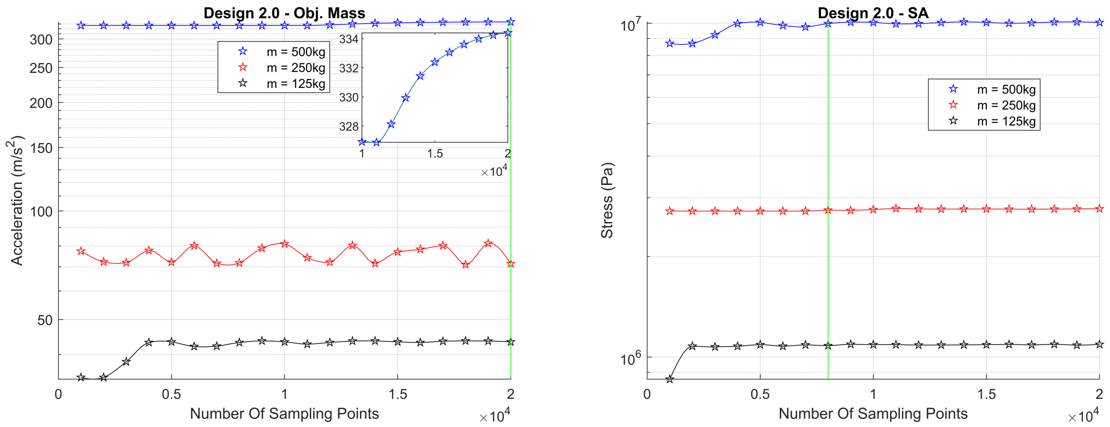

(a) Acceleration of objective mass (b) von-Mises stress in the shock mount

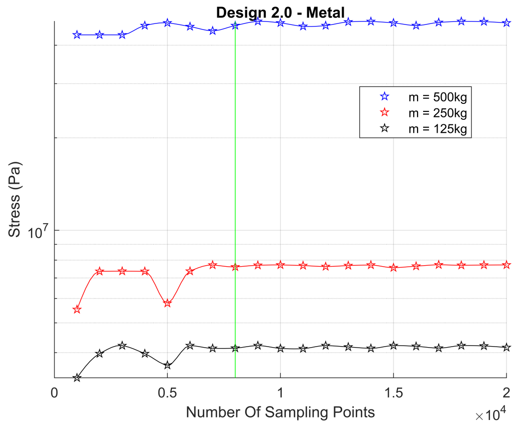

(c) von-Mises stress in the metal interface

Figure 7.2: Sampling frequency convergence for Design 2.0 .

7.1.2. RESULTS AND INFERENCE

The number of intervals parameter sweep convergence results are obtained for 500kg, 250kg, and 125kg mass of the explosive charge using both the designs. The results obtained from the analysis using Design 1.0 are plotted in Fig. 7.1 and Design 2.0 is plotted in Fig. 7.2.

It can be observed from the results of Design 1.0 in Fig. 7.1, that sampling at 8000 intervals will be the optimum for both the acceleration and stress and is marked with a green line. The values are almost stable after this point. Choosing any larger number of sampling points to improve the results can impact the analysis time and memory significantly. From the results of Design 2.0 in Fig. 7.2, it is observed that sampling at 8000 intervals will be the most optimum for von-Mises stress in the shock mount and metal interface. Whereas for the acceleration the values appear to converge after 20000 sampling intervals. It is also very hard to achieve a sampling rate beyond 20000Hz in reality. Therefore for acceleration, the sampling intervals are set to 20000. It can be observed that for some lower values of explosive mass the convergence is earlier than the higher explosive mass. So it can be inferred that when working with large shocks, a higher number of sampling points are needed. For uniformity in the analysis of the shock mount, the optimal values obtained from the large shock is applied for all lower shocks. To be on the safer side, a little higher than optimal sampling points is chosen as these values can vary a little during geometry changes. The results are significant, the default value in Abaqus is 20 sampling points which is way lesser than the optimum obtained from this analysis.

7.2. MESH CONVERGENCE

Meshing is one of the most critical parts of the finite element analysis. It determines at what level of refinement the numerical approximations no longer significantly influence the result of the analysis. The analysis is swept from a coarse mesh to a fine mesh. Result extraction is similar to that used in Sec. 7.1.1, with the optimal values of sampling points applied in their respective fields.

7.2.1. PREPARING THE MESH

For Design 1.0 and Design 2.0: The shock mount, i.e Face 2 in Fig. 5.2a and Fig. 5.2b, the approximate global mesh size is chosen to be M, with a deviation factor of 0.1 and minimum size factor of 0.1.

For Design 1.0 and Design 2.0: The objective mass, i.e Face 1 in Fig. 5.2a and Fig. 5.2b, the approximate global mesh size is chosen to be $H3$ (i.e one element size), with a deviation factor of 0.1 and minimum size factor of 0.1. Being a rigid body the mesh size of the objective mass does not have much influence in the acceleration results. This can be observed from the results in Tab. 7.1.

Mesh Size	Acceleration (m/s^2)	Stress-SA(MPa)	Time For Analysis (min)
One element thick (H3)	4503.90	9.7598	50
Using Full Mesh Size (M)	4532.90	9.7569	113

Table 7.1: Mesh convergence in the objective mass.

For Design 2.0: The metallic interface, i.e Face 3 in Fig. 5.2b, is applied with the approximate global mesh size of $M \times 1.5$, with a deviation factor of 0.1 and minimum size factor of 0.1. The value of $M \times 1.5$ for mesh size is chosen as a result of the trade-off between the time taken for the simulation and error in the result when compared with the results of the original mesh. This can be observed from the results in Tab. 7.2. This increase in mesh size is performed as the mesh size has a direct relation to the analysis time increment as shown in Sec. 5.3.3, which in turn influences the run time of the analysis.

Mesh Size	Acceleration (m/s^2)	Stress-SA(MPa)	Stress-Metal(MPa)	Time (min)
M	167.70	7.405	29.83	152
M x 1.5	162.13	7.404	27.756	122
M x 2.5	140.00	7.408	20.688	119

Table 7.2: Mesh convergence in the metal interface.

Using the generated meshed model, a mesh convergence study is performed by sweeping the mesh size parameter (M). The results of the mesh convergence study are shown in the next subsection.

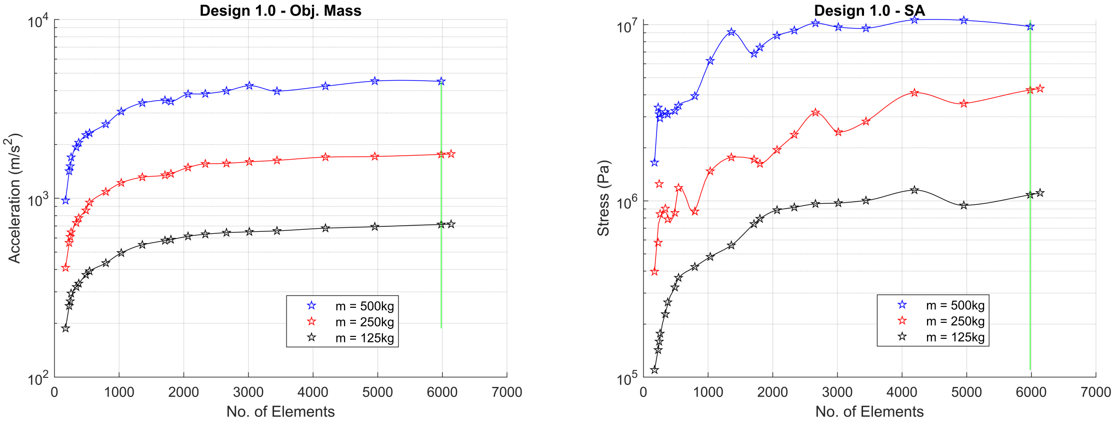

(a) Acceleration of objective mass (b) von-Mises stress in the shock mount

Figure 7.3: Mesh convergence for Design 1.0 .

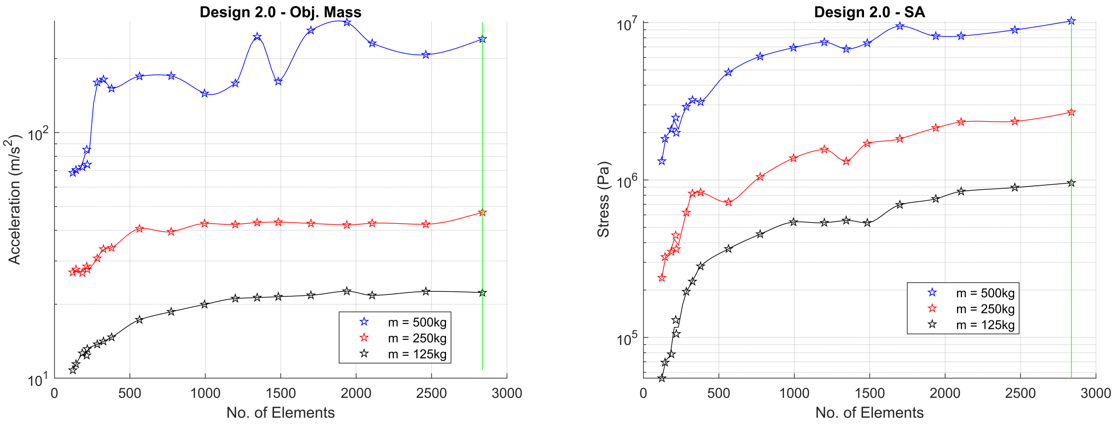

(a) Acceleration of objective mass (b) von-Mises stress in the shock mount

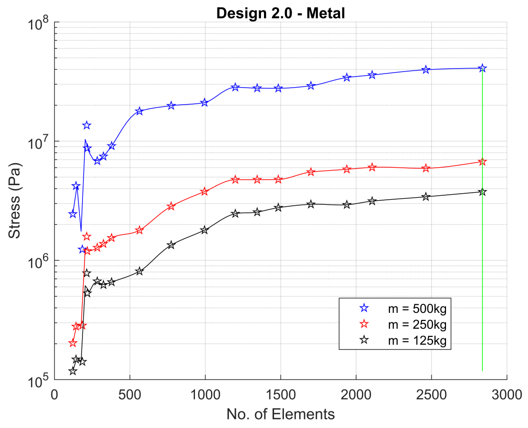

(c) von-Mises stress in the metal interface

Figure 7.4: Mesh convergence for Design 2.0 .

7.2.2. RESULTS AND INFERENCE

The mesh convergence results are obtained for 500kg, 250kg, and 125kg mass of the explosive charge using both the designs. The results obtained from the analysis using Design 1.0 are plotted in Fig. 7.3 and Design 2.0 is plotted in Fig. 7.4.

It can be observed from the results of Design 1.0 in Fig. 7.3, that a mesh size of 0.005m corresponding to 5982 elements will be the optimum for both the acceleration and stress and is marked with a green line. From the results of Design 2.0 in Fig. 7.4, that a mesh size of 0.006m corresponding to 2837 elements will be the optimum for both the acceleration and stress and is marked with a green line. It can be observed that for some lower values of explosive mass the convergence is earlier than the higher explosive mass. Even then a lower mesh size (finer mesh) is chosen to bring uniformity in the analysis. It will also help the model perform better during design changes. Choosing a still finer mesh to improve the results increases the analysis time and memory consumption significantly. The finest mesh analyzed is selected based on the failure of the solver at that mesh. It was observed that as the mesh becomes finer the probability of solver failure increases, returning an error stating excessive element distortion. This means that the finest mesh is unable to withstand the amount of impact energy and distorts excessively making the solver unable to converge to a solution.

7.3. CONCLUSIONS

The optimal number of sampling points and the optimal mesh size is determined for Design 1.0 and Design 2.0. Using a higher sampling point and smaller mesh size might further increase the accuracy of the result from the optimal point, but at a higher computation cost.

This page is intentionally left blank.

8

Shock Mount Design Optimization Results

8.1. Introduction

The results section discusses four studies analyzing the proposed designs. The first two studies of parametric analysis and structural shape optimization are performed using the 2D axisymmetric model. The third study is performed using the complete 3D model to verify the 2D axisymmetric results. Finally, special cases of analysis using the 3D geometries are discussed to validate the robustness of the design.

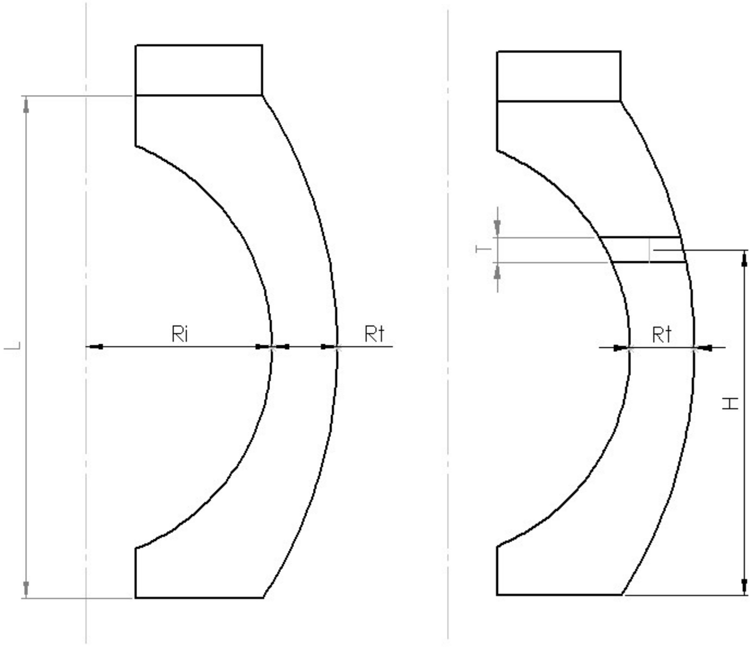

(a) Design 1.0

(b) Design 2.0

Figure 8.1: Shock mount geometry with chosen study parameters.

8.2. Parametric Analysis

The focus of this study is on understanding the design space of the parameters used to model the shock mount. The parameters used in the analysis for Design 1.0 and Design 2.0 are shown in Fig. 8.1a and Fig. 8.1b respectively. The design parameters used for Design 1.0 are chosen such that the shock mount design can be varied largely using these three parameters. The design parameters for Design 2.0 are selected to study the metal interface better and represent the design variation possible in modeling it. The FE analysis is performed according to the procedure described in Chapter 5. Suitable FE parameters such as mesh size and frequency of sampling as found in Chapter 7 are applied in the analysis. The parameter design space used is given in the next subsection. The methodologies used in the python scripting of the parametric analysis are given in Sec. F.1.1.

8.2.1. DESIGN SPACE

The design space is represented here as $\mathbb{R}^3$ for both designs, Design 1.0 and Design 2.0. To facilitate a better comparison of the results, the same design space is used for all the analysis (under various loading conditions) involving one particular shock mount design. The design space used in the analysis of both the designs is shown in the next subsections. The total number of design points to be evaluated in the design space is kept around 100 (total discretization of the design space), considering the computation cost involved in the analysis.

DESIGN 1.0

The three parameters used in the parametric study of Design 1.0 are R_i, R_t, and L. The discretization and bounds used for the design parameters are shown below.

- R_i - Inner curvature radius - $0.1\text{m} \le R_i \le 0.4\text{m}$ with a discretization size of 0.05m, giving 7 design points.
- R_t - Thickness at mid curvature - $0.08\text{m} \le R_t \le 0.16\text{m}$ with a discretization size of 0.02m, giving 5 design points.
- L - Length of the shock mount - $0.9\text{m} \le L \le 1.1\text{m}$ with a discretization size of 0.1m, giving 3 design points.

The bounds for R_i and R_t are chosen by trail, their design set was found to be most sensitive to the results. The analysis was found to fail statically for lower R_t under few parameter combinations. The lower bound of R_i is chosen such that there is no linear solid connecting the objective mass with the support. The parameter L has few and close design points, as the length has no large influence on the performance. The parametric study of Design 1.0 involves 105 (7x5x3) design points. The FE results are evaluated at all these design points and the results are shown in the next section.

DESIGN 2.0

The three parameters used in the parametric study of Design 2.0 are R_t, H, and T. The discretization and bounds used for the design parameters are shown below.

- R_t - Thickness at mid curvature - $0.08\text{m} \le R_t \le 0.16\text{m}$ with a discretization size of 0.02, giving 5 design points.
- H - Position of the metal interface from the base - $0.2\text{m} \le H \le 0.8\text{m}$ with a discretization size of 0.15, giving 5 design points.
- T - Thickness of the metal interface - $0.005\text{m} \le T \le 0.035\text{m}$ with a discretization size of 0.01m, giving 4 design points.

The parametric study of Design 2.0 involves 100 (5x5x4) design points. The FE results are evaluated at all these design points and are shown in the next section.

8.2.2. RESULTS

The FE analysis is performed in the discretized design space. The acceleration of the objective mass due to the applied shock load generated during the blast of 500kg, 250kg, and 125kg of the explosive charge is determined and is shown in Fig. 8.2, Fig. 8.3 and Fig. 8.4 respectively. The von-Mises stress experienced by the shock mount due under the applied shock load generated during the blast of 500kg, 250kg, and 125kg of the explosive charge is determined and is shown in Fig. 8.5, Fig. 8.6 and Fig. 8.7 respectively. The von-Mises stress experienced by the metal interface as a result of the applied shock load generated during the blast of 500kg, 250kg, and 125kg of the explosive charge is determined and is shown in Fig. 8.8. The figures show the results for Design 1.0 and Design 2.0, with the acceleration and stress values scattered using the color bar at their respective design points. The unfilled scattered points with black circles, represent FEA failure.

The failure is caused due to the conditions described in Sec. 5.4. The results obtained from the analysis are discussed in the next subsection.

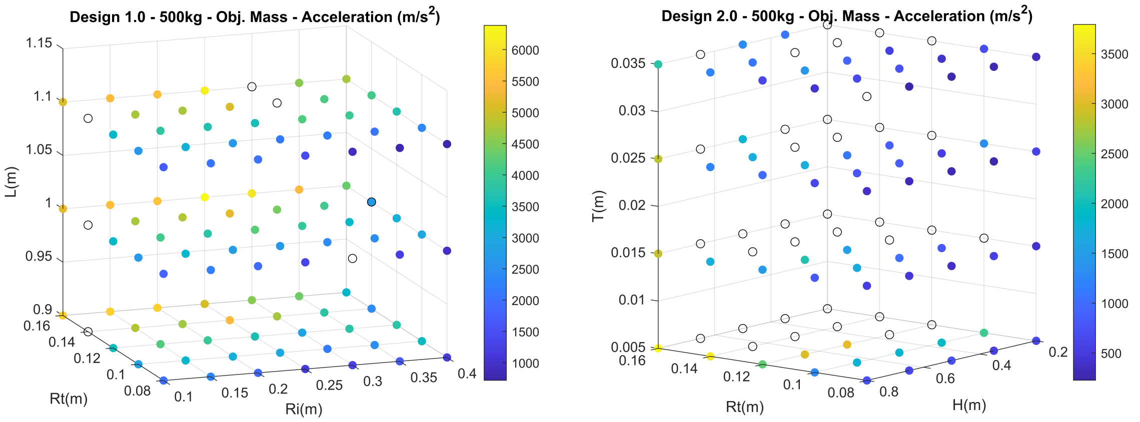

(a) Design 1.0

(b) Design 2.0

Figure 8.2: Parametric analysis with acceleration of objective mass for a 500kg TNT explosive charge.

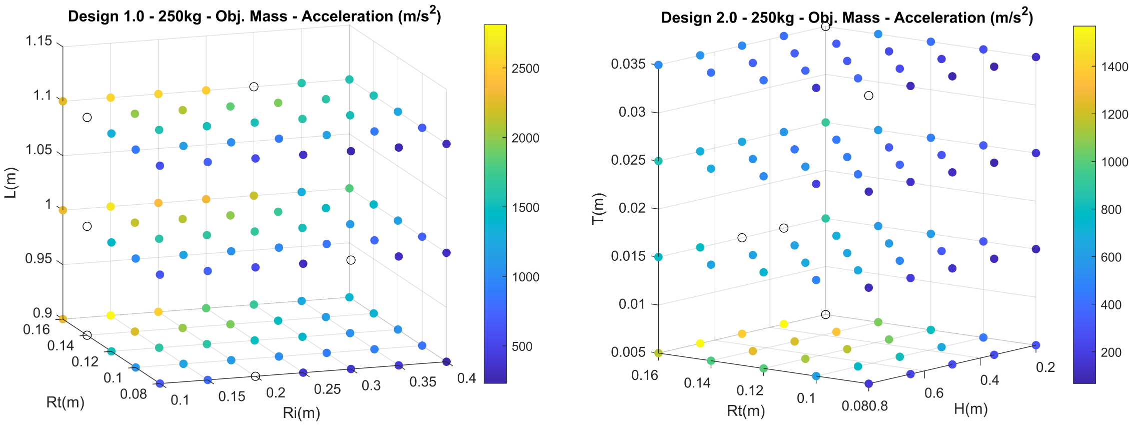

(a) Design 1.0

(b) Design 2.0

Figure 8.3: Parametric analysis with acceleration of objective mass for a 250kg TNT explosive charge.

The lowest acceleration response values obtained from the parametric study, with a feasible stress level, is tabulated in Tab. 8.1 and Tab. 8.2 for Design 1.0 and Design 2.0 respectively.

Explosive Charge (kg)	R_i(m)	R_t(m)	L(m)	A_{min} (m/s^2)	σ(Pa)
500	0.1	0.08	1.1	1698.20	6.39×10^6
250	0.3	0.08	1.1	230.09	3.77×10^6
125	0.4	0.08	1.1	112.73	1.18×10^6

Table 8.1: Design parameters with lowest feasible acceleration values for Design 1.0 .

Explosive Charge (kg)	R_t(m)	H(m)	T(m)	A_{min} (m/s^2)	σ(Pa)	σ_{metal}(Pa)
500	0.1	0.35	0.035	408.23	8.46×10^6	114.44×10^6
250	0.08	0.35	0.035	66.56	2.64×10^6	12.52×10^6
125	0.08	0.35	0.035	20.72	0.82×10^6	6.54×10^6

Table 8.2: Design parameters with lowest feasible acceleration values for Design 2.0 .

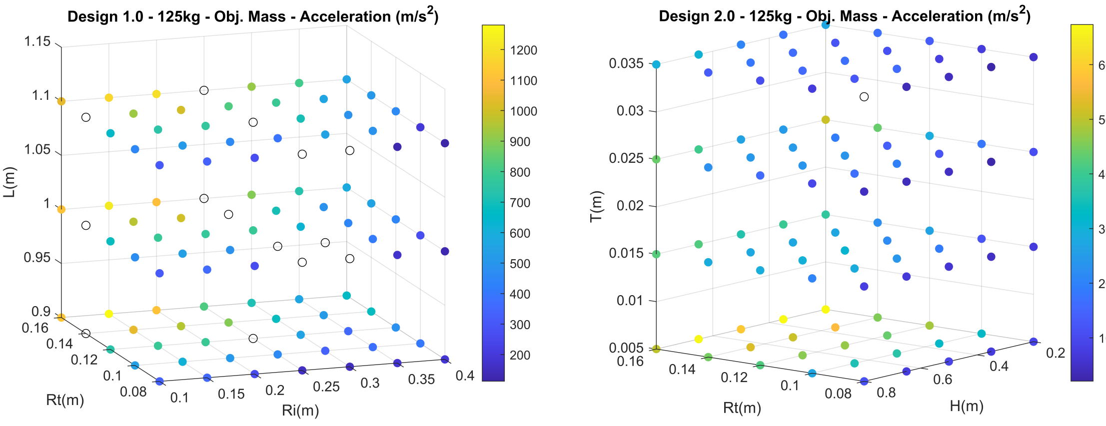

(a) Design 1.0

(b) Design 2.0

Figure 8.4: Parametric analysis with acceleration of objective mass for a 125kg TNT explosive charge.

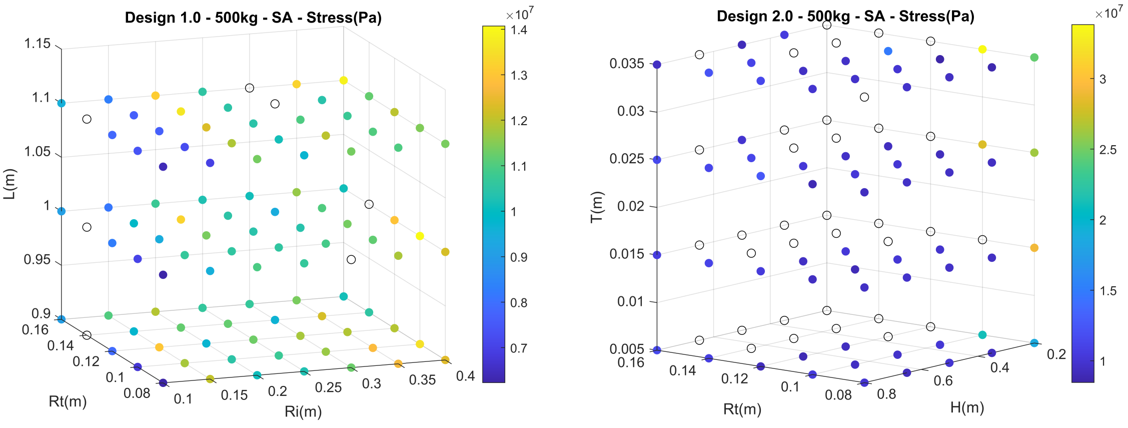

(a) Design 1.0

(b) Design 2.0

Figure 8.5: Parametric analysis with von-Mises stress sustained in the shock mount for a 500kg TNT explosive charge.

8.2.3. DISCUSSION

This parametric study has helped in understanding the nature of the design space of the problem. Reducing the acceleration response of the objective mass is the main end goal. It can be observed from the plots of Fig. 8.2, Fig. 8.3 and Fig. 8.4 that the length of the shock absorber (L) and thickness of the metal (T) have the least sensitivity for the acceleration of objective mass among the parameters in Design 1.0 and Design 2.0 respectively. The inner curvature radius (R_i) and the thickness at mid curvature (R_t) have the highest sensitivity for the acceleration of objective mass in Design 1.0 and Design 2.0 respectively.

From the parametric study, it can be observed that the acceleration and stress plots are almost inverse curves. As the acceleration response of objective mass decreases the von-Mises stress observed in the shock mount and metal interface increases. So there should exist an optimal design point as a balance between acceleration and the stresses if the stresses are above the maximum tensile stress. Else the point of minimum acceleration is the best design point. It can be observed from the plots of Design 1.0, that the optimal value of minimum objective mass acceleration response requires a higher R_i, lower R_t, and a lower L. Similarly, for Design 2.0, the minimum acceleration of the objective mass is observed next to a higher R_t, lower H, and a lower T.

The analysis of Design 2.0 experiences multiple failures due to the causes mentioned in Sec. 5.4, for a larger R_t and lower H. This is due to the presence of a heavy metal interface very close to the ground, this forces very

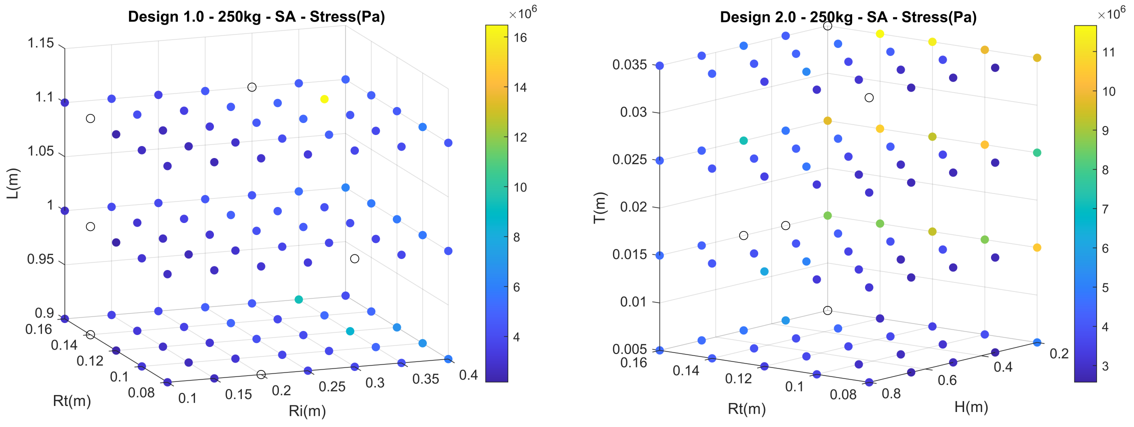

(a) Design 1.0 (b) Design 2.0

Figure 8.6: Parametric analysis with von-Mises stress sustained in the shock mount for a 250kg TNT explosive charge.

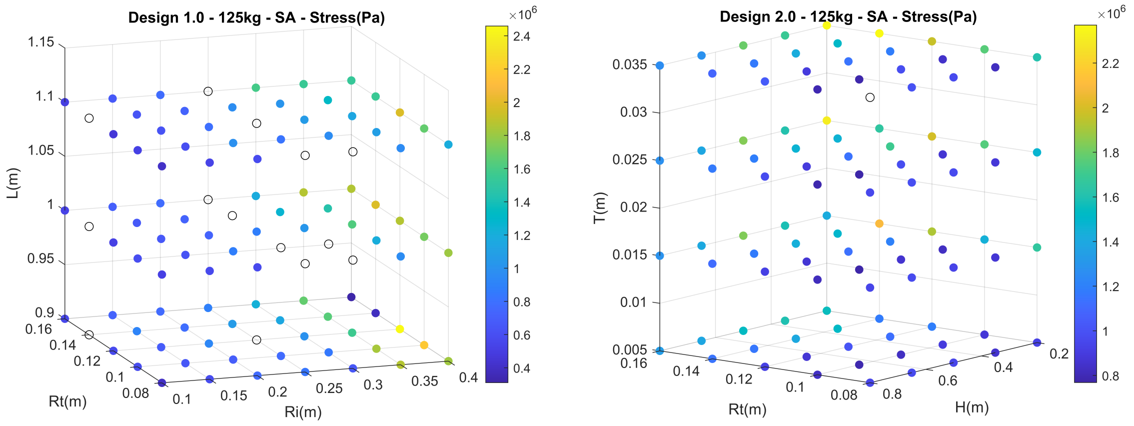

(a) Design 1.0 (b) Design 2.0

Figure 8.7: Parametric analysis with von-Mises stress sustained in the shock mount for a 125kg TNT explosive charge.

little hyperelastic material to withstand all the reflected waves from the metal interface and also the incident shock. This brings in very large distortions in the elements between the metal interface and the ground as shown in Fig. 8.16(b), causing solver failure. The stress levels experienced by the metal interface as shown in Fig. 8.8 is well below the yield strength for structural steel and hence safe to operate. From the stress plots of Fig. 8.5, Fig. 8.6 and Fig. 8.7, it can be seen that for higher shock loads there is a region in the design space where the von-Mises stresses levels are above the tensile stress of neoprene material. This is undesirable, and more on this is discussed in the next section under optimization.

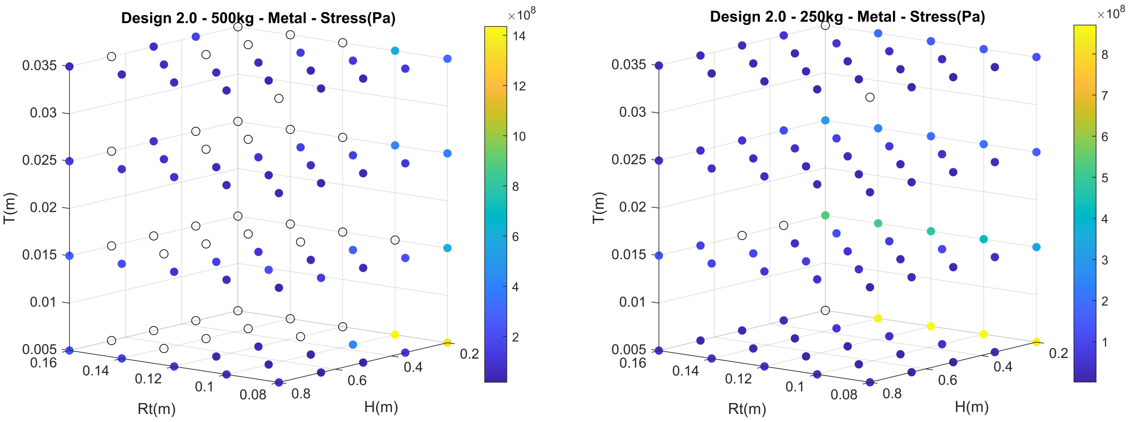

(a) 500kg explosive charge

(b) 250kg explosive charge

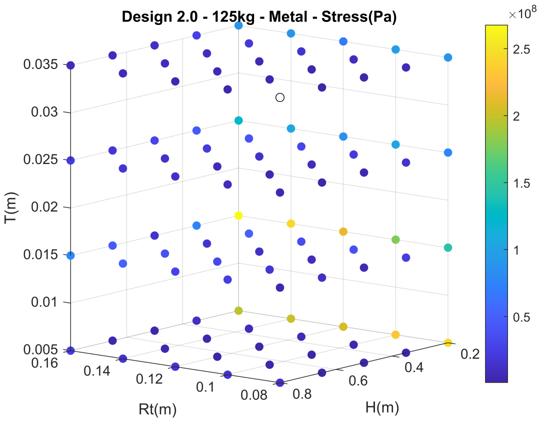

(c) 125kg explosive charge

Figure 8.8: Parametric analysis with von-Mises stress sustained in the metal interface for Design 2.0.

8.3. SHAPE OPTIMIZATION

The objective of this study is to perform a structural shape optimization and determine the optimal design parameters from the design space. The parameters used in the shape optimization are similar to the ones used in the parametric analysis performed in Sec. 8.2. This study is performed using the BOBYQA optimizer discussed in Chapter 6. The methodologies used in the python scripting of the optimization analysis are given in Sec. F.1.1.

8.3.1. PROBLEM

The optimization problem contains three variables that control the geometry in the finite element problem. The objective is to minimize the acceleration response experienced by the objective mass, while constrained by the maximum allowable stress in the shock mount. There are also bounded constrains on the design variables. To be fair with the analysis all the optimization algorithms are executed from 3 initial conditions, from the lower bound, midpoint, and upper bound of the design space respectively. The design space is represented here as $\mathbb{R}^3$ for both designs, Design 1.0, and Design 2.0. The optimization problem formulations for Design 1.0 and Design 2.0 are shown below.

8.3.2. DESIGN 1.0

The optimization problem used in the analysis of Design 1.0 is stated formally in the negative null form as:

$$\begin{aligned} \min_{R_i,R_t,L} \ & f = \frac{a}{a_{max}} \\ \text{st.} \ & \frac{\sigma^n}{\sigma^n_{max}} - 1 \le 0 \\ & 0.1 \le R_i \le 0.4 \\ & 0.06 \le R_t \le 0.16 \\ & 0.9 \le L \le 1.1 \end{aligned} \tag{8.1}$$

here, a is the acceleration response experienced by the objective mass obtained from the FE analysis, a_{max} is the maximum expected acceleration used to normalize the obtained acceleration, σ^n is the von-Mises stress experienced by the shock mount (n->neoprene) as obtained from the FE analysis and σ^n_{max} is the maximum allowable stress in the neoprene hyperelastic material after a factor of safety (FOS).

8

But the BOBYQA optimizer is a bounded unconstrained optimizer, therefore the constraints are included along with the objective. There are two ways to do this, the best one is by using penalty functions and the other is using barrier functions. The disadvantage with barrier functions is that the optimizer needs to start from a feasible initial condition, which is not guaranteed in this study. Therefore penalty functions are used to modify the constrained optimization problem into an unconstrained optimization problem and the formulation is given below. The penalty factor/constant of 10000 is chosen using trial and error, based on the slope of the constraint values if it is violated.

$$\begin{aligned} \min_{x=[R_i,R_t,L]} \ & f = \frac{a}{a_{max}} + 10000 \times \max\left(0, (\frac{\sigma^n}{\sigma^n_{max}} - 1)\right)^2 \\ & 0.1 \le R_i \le 0.4 \\ & 0.06 \le R_t \le 0.16 \\ & 0.9 \le L \le 1.1 \end{aligned} \tag{8.2}$$

The results for the optimization using Design 1.0 is shown in the next section. There are three optimization cycles performed for three different loading conditions. Those three optimization cycles differ in their initial condition as given below.

1. $x_0 = [R_i, R_t, L]_0 = [0.1, 0.06, 0.9]$; Lower bound.
2. $x_0 = [R_i, R_t, L]_0 = [0.25, 0.11, 1]$; Mid point.
3. $x_0 = [R_i, R_t, L]_0 = [0.4, 0.16, 1.1]$; Upper bound.

MAX. PARAMETERS

Different parameters for A_{max} and σ^n_{max} are used for different loading conditions which are shown in the table Tab. 8.3. The shock mount is modelled using hyper elastic neoprene material. The tensile strength of neoprene rubber is between 12MPa - 24MPa and the compressive strength is estimated to be between 14.4MPa - 28.8MPa[14]. The FOS ($\text{FOS}_{\sigma^n} = \frac{\sigma^n_T}{\sigma^n_{\text{max}}}$ is determined based on the lowest tensile strength of neoprene rubber, $\sigma^n_T = 12\text{MPa}$.

Explosive Charge (kg)	A_{max} (m/s^2)	σ^n_{max}(Pa)	FOS_{σ^n}
500	5000	8×10^6	1.5
250	2000	6×10^6	2
125	800	4×10^6	3

Table 8.3: Normalization parameters used in the optimization for Design 1.0 .

8.3.3. DESIGN 2.0

The optimization problem used in analysis of Design 2.0 is stated formally in the negative null form as:

$$
\begin{aligned}
\min_{R_t,H,T} f &= \frac{A}{A_{max}} \\
\text{st.} \quad & \frac{\sigma^n}{\sigma^n_{max}} - 1 \leq 0 \\
& \frac{\sigma^m}{\sigma^m_{max}} - 1 \leq 0 \\
& 0.06 \leq R_t \leq 0.15 \\
& 0.2 \leq H \leq 0.8 \\
& 0.005 \leq T \leq 0.05
\end{aligned}
\tag{8.3}
$$

here, A is the acceleration response experienced by the objective mass obtained from the FE analysis, A_{max} is the maximum expected acceleration used to normalize the obtained acceleration, σ^n and σ^m are the von-Mises stress experienced by the neoprene hyperelastic shock mount (n->neoprene) and the metal interface present in the shock mount (m->metal) respectively. These values are obtained from the FE analysis. σ^n_{max} and σ^s_{max} are the maximum allowable stress in the neoprene hyperelastic material and the structural steel metal interface respectively after a factor of safety (FOS).

Similar to the Design 1.0 optimization, the penalty functions are used to modify the constrained optimization problem into an unconstrained optimization problem and the formulation is given below. The penalty factor/constant of 10000 is chosen using trial and error, based on the slope of the constraint values if it is violated.

$$
\begin{aligned}
\min_{x=[R_t,H,T]} f = \frac{A}{A_{max}} + 10000 \times \max\Big(0, (\frac{\sigma^n}{\sigma^n_{max}} - 1)\Big)^2 + 10000 \times \max\Big(0, (\frac{\sigma^m}{\sigma^m_{max}} - 1)\Big)^2 \\
0.06 \leq R_t \leq 0.15 \\
0.2 \leq H \leq 0.8 \\
0.005 \leq T \leq 0.05
\end{aligned}
\tag{8.4}
$$

The results for the optimization using Design 2.0 is shown in the next section. There are three optimization cycles performed for three different loading conditions. Those three optimization cycles differ in their initial condition as given below.

1. $x_0 = [R_t, H, T]_0 = [0.06, 0.2, 0.005]$; Lower bound.
2. $x_0 = [R_t, H, T]_0 = [0.105, 0.5, 0.0275]$; Mid point.
3. $x_0 = [R_t, H, T]_0 = [0.15, 0.8, 0.05]$; Upper bound.

MAX. PARAMETERS

Different parameters for A_{max}, $\sigma^n_{\max}$ and $\sigma^m_{\max}$ are used for different loading conditions which are shown in the table Tab. 8.4. The shock mount is modelled using hyper elastic neoprene material. The tensile strength of neoprene rubber is between 12MPa - 24MPa and the compressive strength is estimated to be between 14.4MPa - 28.8MPa[14]. The FOS (FOS$_{\sigma^n} = \frac{\sigma^n_T}{\sigma^n_{\max}}$ is determined based on the lowest tensile strength of neoprene rubber, $\sigma^n_T = 12$MPa. The tensile yield strength of structural steel used to model the metal interface is given to be $\sigma^n_T = 350$MPa[14]. The FOS of this metal interface is given by, FOS$_{\sigma^m} = \frac{\sigma^m_T}{\sigma^m_{\max}}$.

Explosive Charge (kg)	$A_{\max}$ (m/s^2)	$\sigma^n_{\max}$(Pa)	FOS$_{\sigma^n}$	$\sigma^m_{\max}$(Pa)	FOS$_{\sigma^m}$
500	500	8×10^6	1.5	175×10^6	2
250	100	6×10^6	2	175×10^6	2
125	50	6×10^6	2	175×10^6	2

Table 8.4: Normalization parameters used in the optimization for Design 2.0 .

8.3.4. OPTIMIZATION ALGORITHM SETUP

The optimizer is setup as described in Sec. 6.2. The optimizer control parameter values as described in Sec. 6.2.2 and Sec. 6.2.3 is used in the study, and a summary of it is given in the table. Other parameters are not found to influence the result much, and therefore default parameter values are considered in the study.

Control Parameter	Values / Flag
‘scaling_within_bounds’	‘True’
‘objfun_has_noise’	‘False’
‘restarts.soft.move_xk’	‘False’
‘general.rounding_error_constant’	$1e-3$
‘seek_global_minimum’	‘True’
‘slow.history_for_slow’	2
‘slow.thresh_for_slow’	10^{-4}
‘slow.max_slow_iters’	3
‘rhoend’	10^{-4}
‘maxfun’	100

Table 8.5: Optimization algorithm control parameters.

8.3.5. RESULTS

The optimization algorithm is executed and FE results for the respective design points are found. The results are then fed back to the algorithm and the algorithm drives the design point towards the location of objective minimum. The solution path taken by the algorithm during the shape optimization of the shock mount under the impact of a shock wave created during the blast of an underwater explosive of charge 500kg, 250kg and 125kgare shown respectively in Fig. 8.9, Fig. 8.10 and Fig. 8.11 for Design 1.0 and Design 2.0. The results show the variations in the objective function and acceleration for respective design and shock loads as the optimization algorithm drives the analysis. The function values are represented using the color bar on a scattered plot at their respective design points. The plots in Fig. 8.12, Fig. 8.13 and Fig. 8.14 gives the value of the objective function over the iteration number. It can be seen that all the analysis utilized the maximum function iteration ‘maxfun’ to terminate the analysis. Therefore a linear search is performed over the obtained objective function values to determine the actual local optima and its corresponding iteration number in-turn the optimal design point.

The optimal design point obtained from the optimization algorithm for each analysis is tabulated in Tab. 8.6 and Tab. 8.7 for Design 1.0 and Design 2.0 respectively. The corresponding values of the objective function, acceleration of objective mass, and stresses in the shock mount and metal interface are also shown in the table.

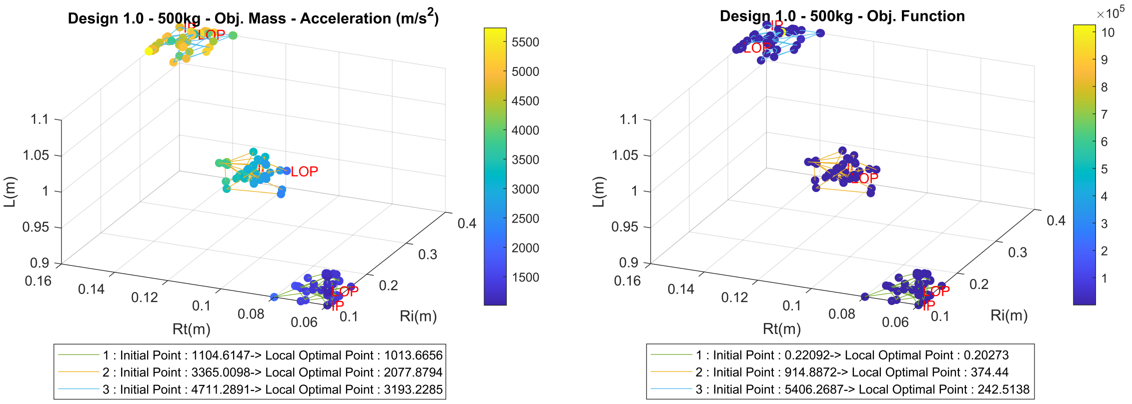

(a) Acceleration @ Design 1.0 (b) Objective function @ Design 1.0

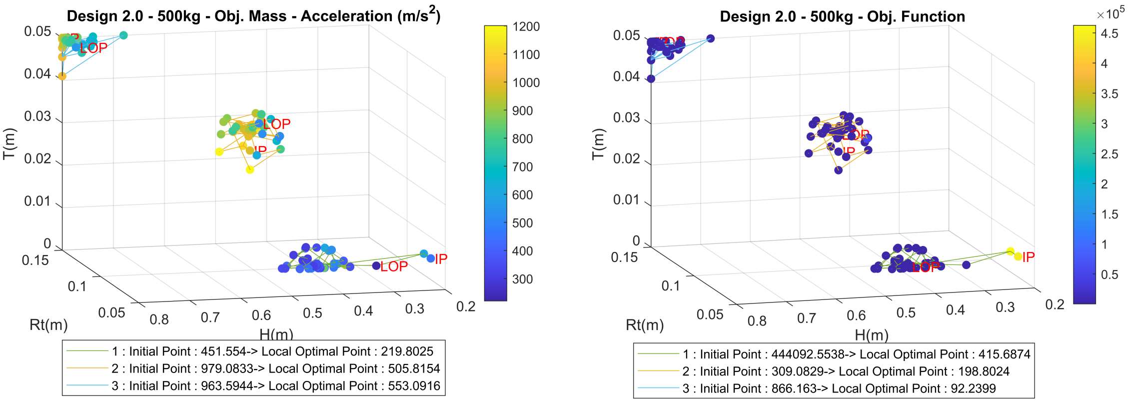

(c) Acceleration @ Design 2.0 (d) Objective function @ Design 2.0

Figure 8.9: Acceleration and objective function values along with their design points as a result of minimization of the objective function for 500kg explosive charge.

Explosive Charge (kg)	Opti.	R_i(m)	R_t(m)	L(m)	A (m/s^2)	σ^n(Pa)	Obj. fn
500	1	0.1	0.06	0.9201	1013.66	6.12×10^6	0.2027
500	2	0.217	0.103	1	2899.42	9.55×10^6	374.44
500	3	0.33	0.16	1.099	4664.43	9.24×10^6	242.51
250	1	0.2533	0.0633	0.9006	143.17	3.67×10^6	0.0715
250	2	0.2273	0.06	0.9674	164.78	3.17×10^6	0.0823
250	3	0.313	0.1506	1.099	1308.44	5.07×10^6	0.6542
125	1	0.1	0.06	1.0227	182.56	5.16×10^6	0.2282
125	2	0.2712	0.06	1	56.53	0.99×10^6	0.0706
125	3	0.3945	0.1456	1.069	431.76	1.56×10^6	0.5397

Table 8.6: Results for the objective function minimization problem using Design 1.0 .

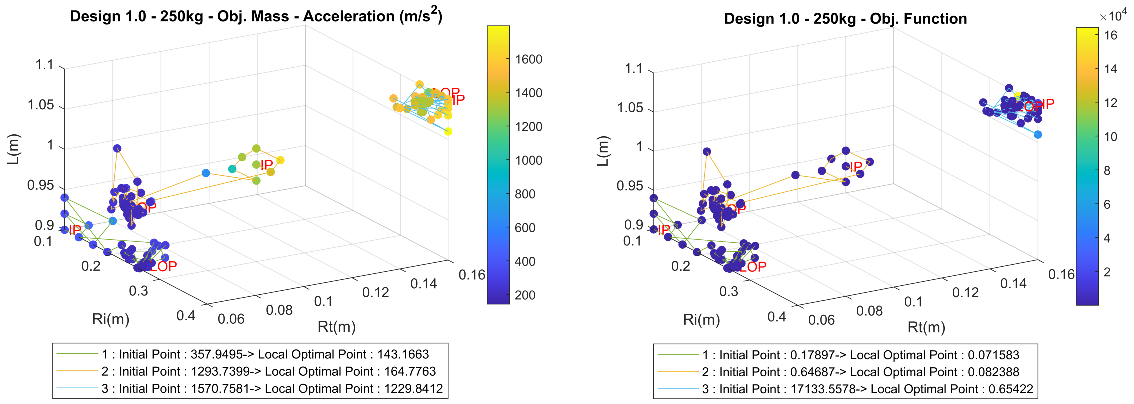

(a) Acceleration @ Design 1.0

(b) Objective function @ Design 1.0

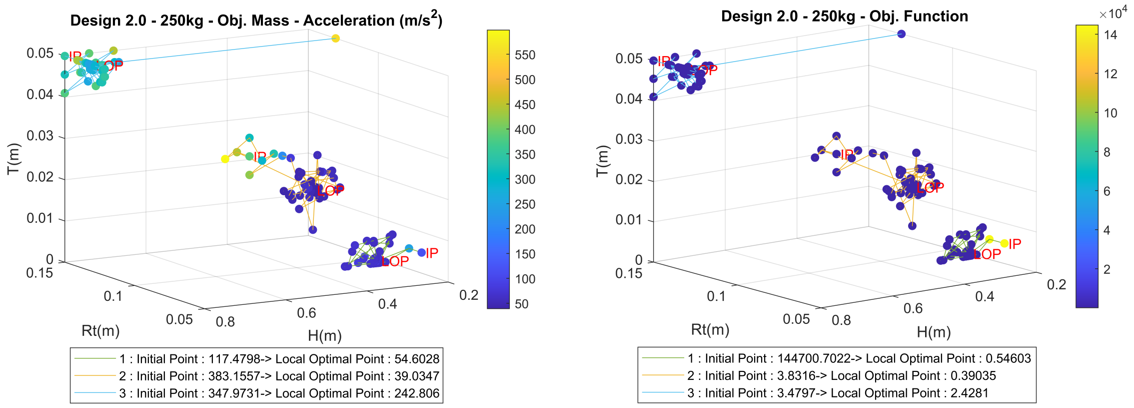

(c) Acceleration @ Design 2.0

(d) Objective function @ Design 2.0

Figure 8.10: Acceleration and objective function values along with their design points as a result of minimization of the objective function for 250kg explosive charge.

Ex. Charge (kg)	Opti.	R_t(m)	H(m)	T(m)	A (m/s^2)	σ^n(Pa)	σ^m(Pa)	Obj. fn
500	1	0.06	0.437	0.00537	369.39	9.63×10^6	23.34×10^6	415.68
500	2	0.104	0.5026	0.03188	930.04	9.12×10^6	45.64×10^6	198.8
500	3	0.15	0.7961	0.05	963.49	8.76×10^6	28.00×10^6	92.24
250	1	0.06	0.3395	0.00556	54.60	2.87×10^6	6.00×10^6	0.546
250	2	0.06	0.4981	0.0243	39.64	2.53×10^6	4.44×10^6	0.3964
250	3	0.1306	0.8	0.05	242.80	5.30×10^6	7.41×10^6	2.428
125	1	0.06	0.328	0.0053	20.20	9.68×10^6	1.21×10^6	0.404
125	2	0.0775	0.3495	0.0469	15.31	8.22×10^6	3.55×10^6	0.306
125	3	0.0997	0.7719	0.05	33.32	7.77×10^6	1.18×10^6	0.666

Table 8.7: Results for the objective function minimization problem using Design 2.0 .

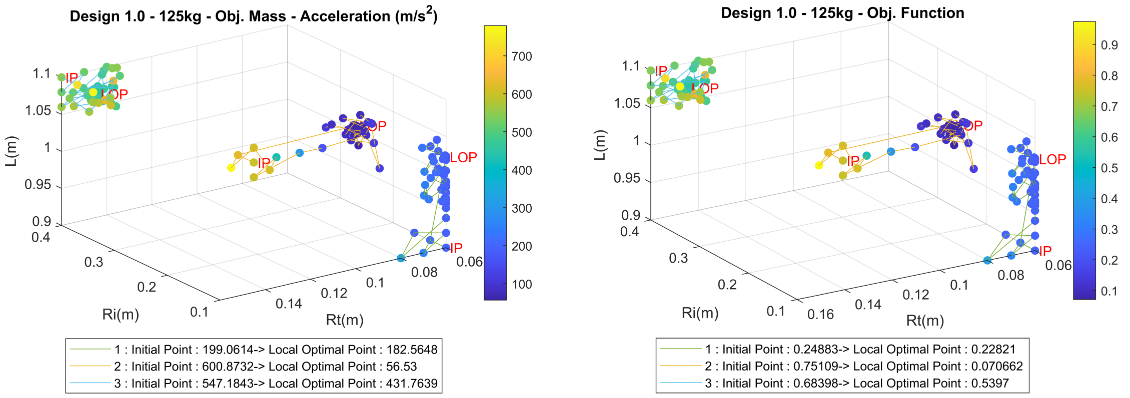

(a) Acceleration @ Design 1.0

(b) Objective function @ Design 1.0

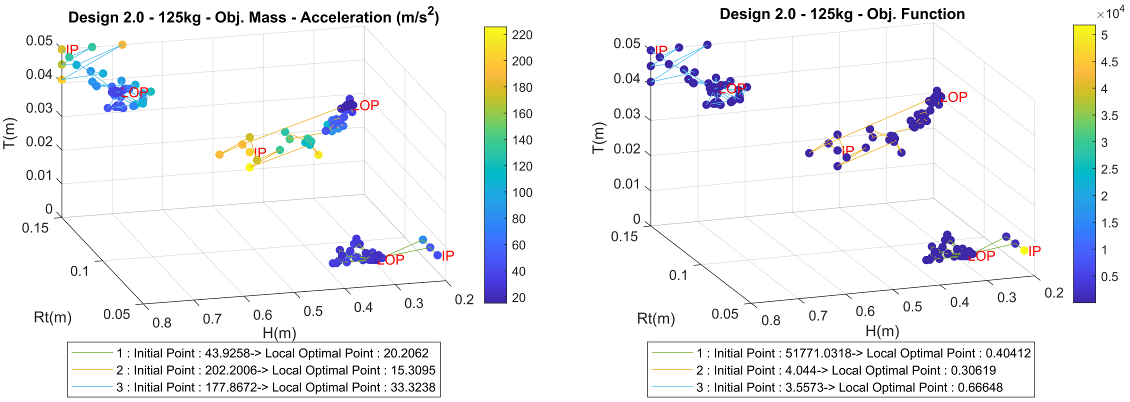

(c) Acceleration @ Design 2.0

(d) Objective function @ Design 2.0

Figure 8.11: Acceleration and objective function values along with their design points as a result of minimization of the objective function for 125kg explosive charge.

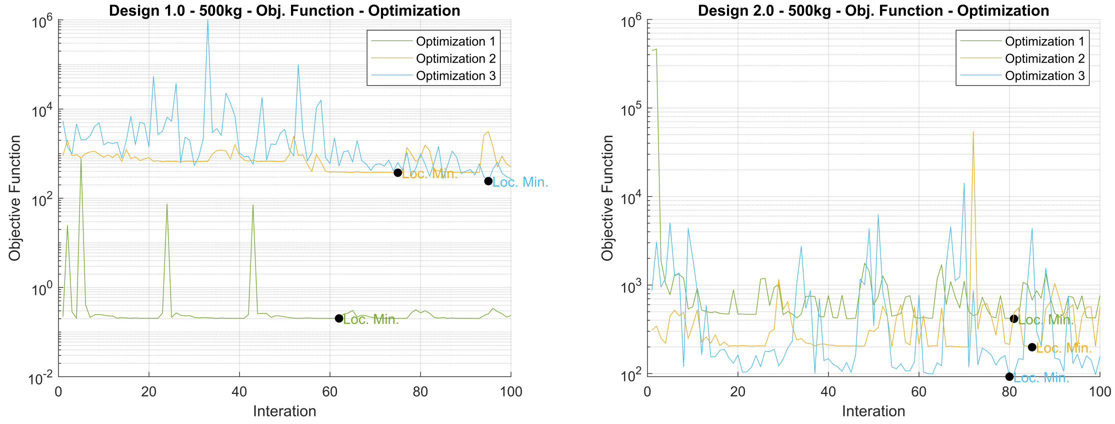

(a) Design 1.0

(b) Design 2.0

Figure 8.12: Objective function values as a function of optimizer iteration for a 500kg explosive charge.

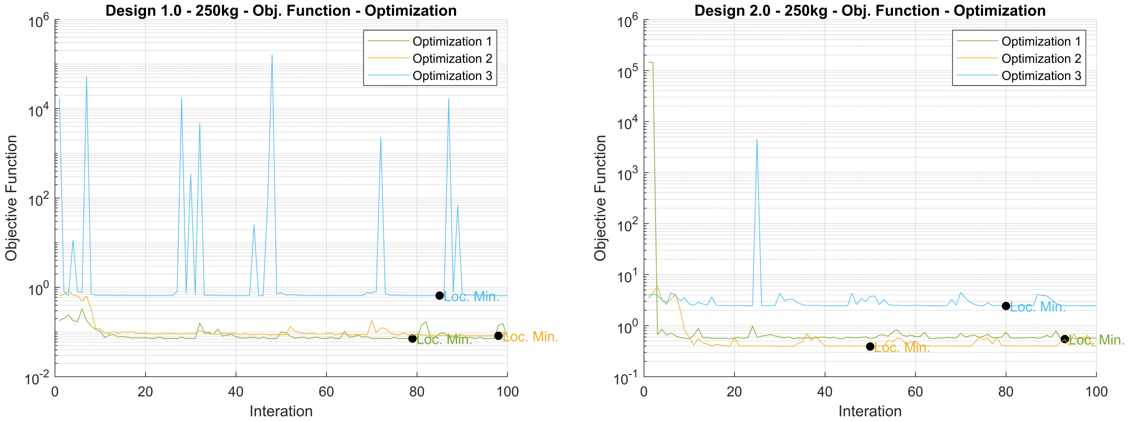

(a) Design 1.0

(b) Design 2.0

Figure 8.13: Objective function values as a function of optimizer iteration for a 250kg explosive charge.

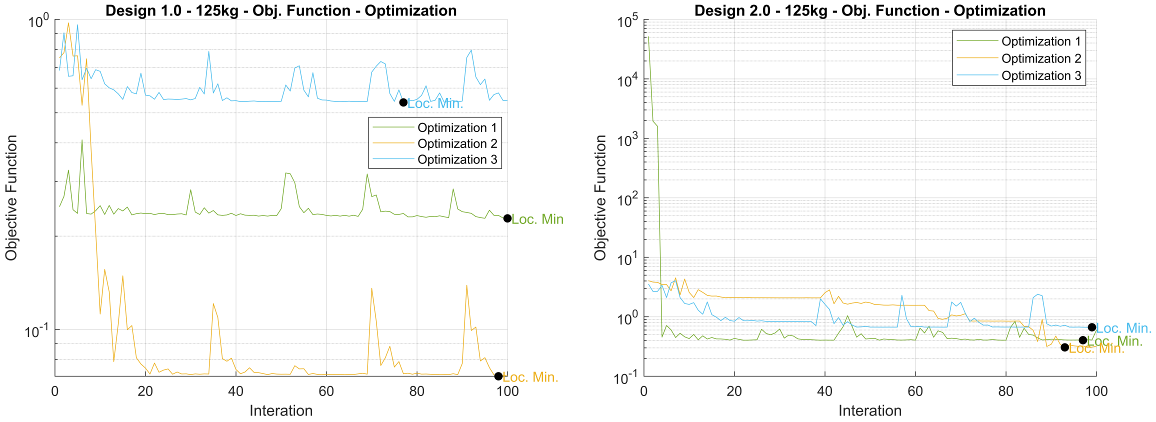

(a) Design 1.0

(b) Design 2.0

Figure 8.14: Objective function values as a function of optimizer iteration for a 125kg explosive charge.

8.3.6. DISCUSSION

It is definite that the optimizer has converged to a better optimum than the initial condition. In no case has the optimizer converged to an optimal solution and global optimum is never reached. In all the cases the optimization solver has terminated due to the limit on the number of function evaluations. The best minimum objective function achieved by the optimizer is then chosen from the generated functional values using a line search. This gives the local minima leading to the local optimum design variable. It could be that the solver could converge to a unique optimum when executed for further function evaluations, but it is not feasible considering the time involved in the optimization process. Almost all the simulations took 3-4 days for Design 1.0 and 4-5 days for Design 2.0 to calculate 100 function evaluations. The inability to converge could be due to multiple reasons. There could be a high degree of numerical noise, considering the meshes and sampling rates involved.

It is observed from Fig. 8.10 and Fig. 8.11, for both the designs the optimizer has pulled the design point to the lowest R_t for Optimization 1 and 2. This also says that the lower magnitude of shocks converge better in the optimization study because they suffer from very little noise due to the finite element approximations. Hence, the magnitude of incident shock loading also plays a major role in the optimization study. The numerical noise experienced by the problem is very clear from Fig. 8.12, Fig. 8.13 and Fig. 8.14. Where, the optimizer tries to proceed in the direction of decreasing objective minima, where it suddenly encounters a peak in the objective function. But the optimizer quickly recovers from the peak and searches for minimum values around. This creates a concentrated cloud of computed points as shown in Fig. 8.9, Fig. 8.10 and Fig. 8.11. This is very much evident from Fig. 8.9, where the shock loading is maximum.

For the 500kg explosive charge shock, from Fig. 8.12, it is evident that the optimizer slowly did proceed towards a minimum as a downward slope in the overall graph can be observed, but did suffer considerably from very high numerical noise. This has translated the global search for an optimum point to a local search, as observed from the scattered clouds close to the initial condition from Fig. 8.9. It is also interesting from the optimization of the 500kg explosive charge, where almost all the optimization problems were initiated from the point of constraint violation (infeasible region). Still, it was able to give a better minimum objective and Optimization 1 in Fig. 8.9 moved into the feasible region with 10 iterations. Other optimizations could not get into the feasible region as such a region is far from its location. It could have got there given a larger limit on the number of function evaluations as the slope has a decreasing trend, but such a problem is inturn infeasible considering computation cost.

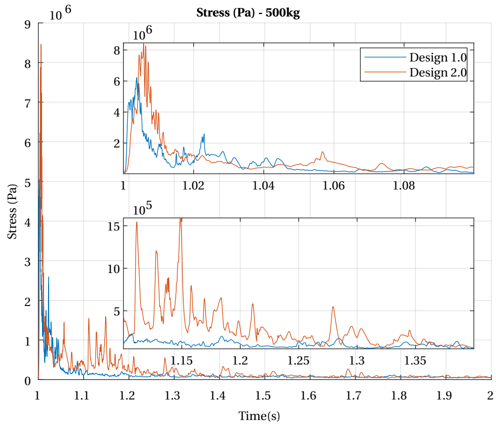

Figure 8.15: Stress response in Design 1.0 and Design 2.0 shock mounts for a shock impact under 500kg explosive charge.

From Tab. 8.6 and Tab. 8.7, the virtual global optima can be chosen using the best results of local optima. It is positive that all but one design have a feasible local optimum. The problem with Design 2.0 loaded under 500kg explosive charge does not have a feasible local minimum. The reason being the constraint on the von-Mises stress experienced by neoprene rubber is above its FOS. The current FOS for the most feasible problem is 1.37 against the requested 1.5. This is acceptable considering the amount of load that the shock mount withstands. The stress response is shown in Fig. 8.15, and the stress is observed to peak out for a very short period. The virtual global optimum values obtained from this analysis are compared with the results from the parametric study in the next section, to come up with the most optimum design for 3D verification and further studies.

8.4. DESIGN SELECTION

The geometric parameters are finalized in this section, to freeze the geometry and perform further analysis. The results of the parametric study and the virtual global minimum results from the optimization study are compared to obtain the best possible geometry for various loading conditions. The results are compared using table Tab. 8.8 and table Tab. 8.9 for Design 1.0 and Design 2.0 respectively, and the best results are highlighted in green. The design parameters in green are the finalized geometric parameters that are used for further verification and analysis. The acceleration analysis results at a maximum acceleration of objective mass using the final optimal design parameters for both designs loaded with a given mass of explosive charge are shown in Fig. 8.16. From Fig. 8.16 it is seen that the impact energy traverses through the shock mount is similar to that of waves. This phenomenon is enhanced for higher magnitude loads. Comparing Fig. 8.16(d)(f) with Fig. 8.16(a)(c)(e), it can be inferred that the metal interface attenuates the acceleration wave, as not much wave disturbance is observed crossing the interface. From Fig. 8.16(b) it can be observed that when the magnitude of shock is larger, there is a significant transmission of energy across the metal interface. The amount of energy reflected is also huge, creating large deformations below the metal interface. More results on acceleration, stress, and displacement are added to Sec. F.2.

Parametric / Optimization	R_i(m)	R_t(m)	L(m)	A (m/s^2)	σ^n(Pa)	Obj. fn
500kg						
Optimization	0.1	0.06	0.9201	1013.66	6.12×10^6	0.2027
Parametric	0.1	0.08	1.1	1698.20	6.39×10^6	0.339
250kg						
Optimization	0.2533	0.0633	0.9006	143.17	3.67×10^6	0.0715
Parametric	0.3	0.08	1.1	230.09	3.77×10^6	0.115
125kg						
Optimization	0.2712	0.06	1	56.53	0.99×10^6	0.0706
Parametric	0.4	0.08	1.1	112.73	1.18×10^6	0.141

Table 8.8: Result comparison between parametric and optimization study for Design 1.0 .

Parametric / Optimization	R_t(m)	H(m)	T(m)	A (m/s^2)	σ^n(Pa)	σ^m(Pa)	Obj. fn
500kg							
Optimization	0.15	0.7961	0.05	963.49	8.76×10^6	28.00×10^6	92.24
Parametric	0.1	0.35	0.035	408.23	8.46×10^6	114.44×10^6	33.82
250kg							
Optimization	0.06	0.4981	0.0243	39.64	2.53×10^6	4.44×10^6	0.3964
Parametric	0.08	0.35	0.035	66.56	2.64×10^6	12.52×10^6	0.665
125kg							
Optimization	0.0775	0.3495	0.0469	15.31	8.22×10^6	3.55×10^6	0.306
Parametric	0.08	0.035	0.035	20.72	0.82×10^6	6.54×10^6	0.414

Table 8.9: Result comparison between parametric and optimization study for Design 2.0 .

8.5. 3D ANALYSIS AND VERIFICATION

The analyses performed in the previous sections are modeled using the 2D axisymmetric model approximation. In this section, the analysis is performed using the corresponding 3D geometry and FE model. The 3D geometry is generated based on the best parameter results obtained from Sec. 8.4. The FE modeling and analysis using the 3D model are performed according to the procedure and analysis parameters discussed in Chapter 5. The appropriate mesh sizes are chosen after a brief mesh convergence study. The results of 2D

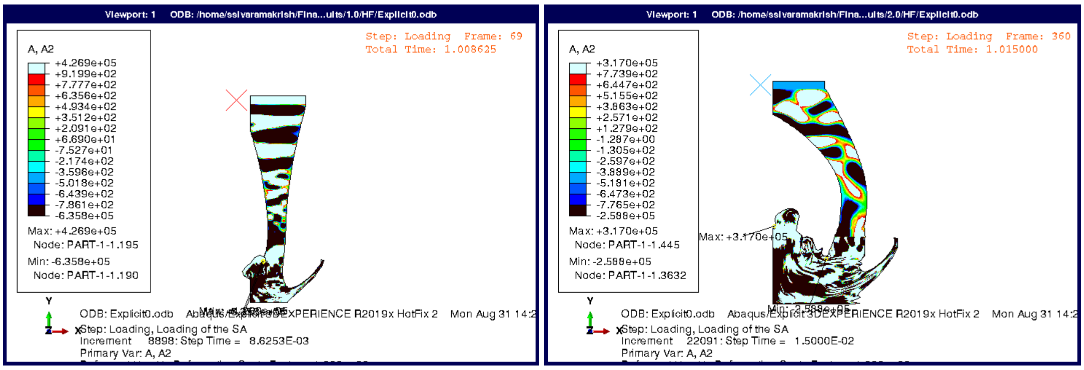

(a) Design 1.0 - 500kg (b) Design 2.0 - 500kg

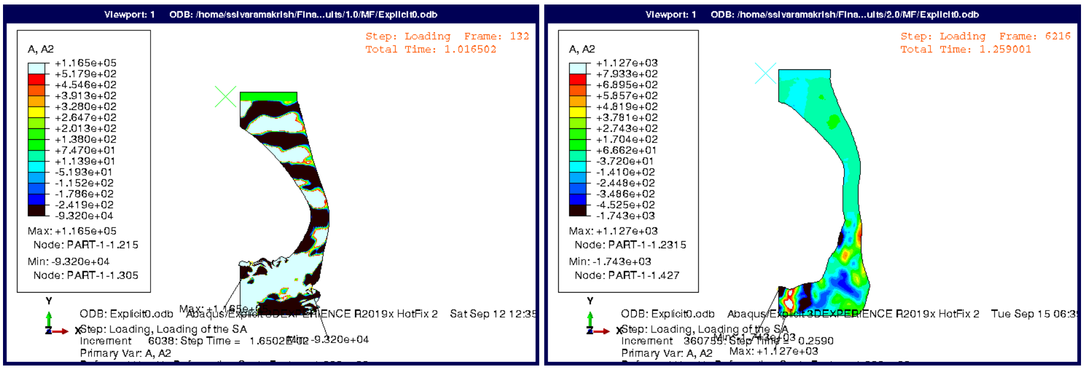

(c) Design 1.0 - 250kg (d) Design 2.0 - 250kg

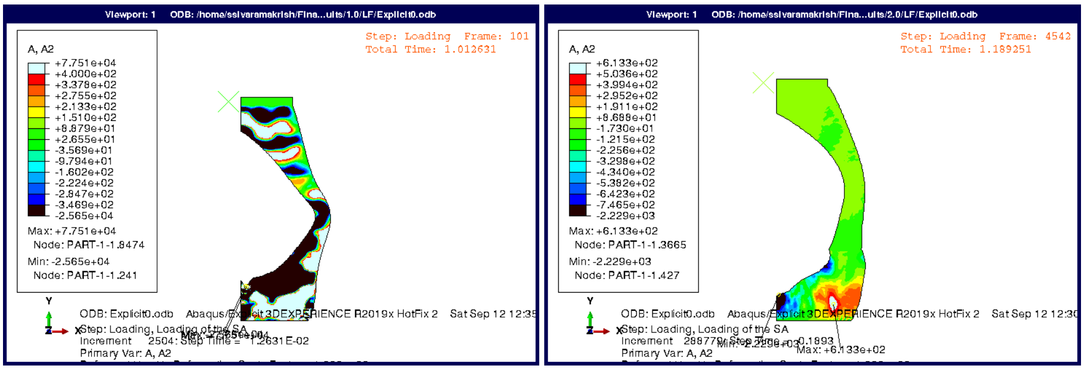

(e) Design 1.0 - 125kg (f) Design 2.0 - 125kg

Figure 8.16: Acceleration results at maximum acceleration of objective mass using the final optimal design parameters for both designs loaded with a given mass of explosive charge.

and 3D analyses are compared in the next section.

8.5.1. COMPARISON OF 2D AND 3D RESULTS

The acceleration response of the objective mass under different masses of explosive charges using Design 1.0 and Design 2.0 when analyzed using 2D axisymmetric and corresponding 3D verification analysis is shown in Fig. 8.17. The responses are almost similar in both studies. The 3D analysis reports a slightly lower amplitude due to the use of a lower number of elements to solve the problem. The analysis has shown that 3D response has some damping behavior to numerical noise and the response curves are smoother than the 2D analysis. The accelerations in Fig. 8.17(a) appear to settle, but in magnitude they are higher than lower magnitude shock profiles for the same time. The 3D analysis traces the 2D axisymmetric analysis better for lower shock loading conditions. The maximum objective mass acceleration results for 3D analysis are shown in Tab. 8.10 and are compared with the 2D results from Tab. 8.8 and Tab. 8.9. In some cases, the results could get no better because of the computational issues involved in handling data and numerical issues faced in working with very fine meshes.

An FFT is performed on the time response data in Fig. 8.17, to obtain the frequency response spectrum of the acceleration which is shown in Fig. 8.18. The devices mounted on board of the ship have their shock response frequencies greater than 25Hz and 37Hz when installed without and with the mounting hardware between the device and the ship structure. Devices with lower response frequencies need approval[42]. Therefore the frequency response of the shock mounts should be below 37Hz to avoid resonance with the on-board devices. From the plots of Fig. 8.17 it is observed that 3D analysis has a lower frequency response and hence a larger bandwidth than the corresponding 2D analysis. This can be attributed to the damping of numerical noise as observed from the time history plots. The Shock Response Frequency (SRF) of Design 1.0 is well over 37Hz in 2D and is below 37Hz in the 3D analysis. For Design 2.0, the SRF is above 37Hz in both 2D and 3D analysis for 500kg of the explosive charge. The SRF is below 37Hz for the analysis of Design 2.0 under 250kg and 125kg of the explosive charge. Both designs have marginally satisfied the frequency response. Therefore this design is only suitable for devices with their response frequencies above the SRF. In Fig. 8.18, high-frequency responses as observed in Design 1.0 is absent in Design 2.0, the reason for this could be that the metal interface filters out the high-frequency components. This proves Design 2.0 superior to Design 1.0 under frequency response.

For general basic comparison, an optical memory hard drive can withstand 300-400Gs acting for 2ms under operating conditions and 650-1000Gs acting for 1ms under nonoperating conditions[43]. From Tab. 8.10, the obtained maximum acceleration value stands at 1013.66m/s^2(103Gs). Therefore both the shock mount designs can protect the device from the largest blast shock wave.

Explosive Charge	500kg	250kg	125kg
Design 1.0 (m/s^2)	1002.90 (1013.66)	151.23 (143.17)	49.73 (56.53)
Design 2.0 (m/s^2)	358.43 (408.23)	35.05 (39.64)	14.40 (15.31)

Table 8.10: Maximum objective mass acceleration results obtained from the 3D analysis for both the designs, 2D results are shown in the bracket.

8.5.2. OBLIQUE SHOCK

The procedure for this 3D analysis is similar to that performed in Sec. 8.5.1, except that it is loaded using an oblique shock instead of a pure vertical load. The displacements u_x and u_z corresponding to x and z directions are loaded with 10% of the displacement amplitude load applied in the y-direction, u_y. The results obtained from the analysis are tabulated in Tab. 8.11.

Explosive Charge	500kg	250kg	125kg
Design 1.0 (m/s^2)	Failure (1002.90)	114.45 (151.23)	27.41 (49.73)
Design 2.0 (m/s^2)	Failure (358.43)	28.59 (35.05)	11.20 (14.40)

Table 8.11: Maximum objective mass acceleration results obtained from the 3D analysis under oblique shock for both the designs, 3D results with pure vertical loading are shown in the bracket.

From Tab. 8.11, the analysis fails for the highest magnitude of loading. The shock mount suffers large distortion in few elements due to the applied magnitude of the shock and the solver fails with an error. The analysis was successful with the lower magnitude of shocks. Design 2.0 shows a better response to an oblique shock than Design 1.0. The shock mounts can operate feasibly under a 10% oblique shock up to moderate shock levels.

8.5.3. VARIATION IN THE MASS

The procedure for this 3D analysis is similar to that performed in Sec. 8.5.1, except that the weight of the objective mass is lowered. This is done by reducing the height of the objective mass from 0.3m to 0.2m. This in turn reduces the objective mass from 44.39kg to 29.59kg. The results obtained from the analysis are tabulated in Tab. 8.12.

From Tab. 8.12, the analysis fails for the highest magnitude of loading. This is because the shock mount does not have sufficient preload to withstand the shock and undergoes large element distortions. The analysis was successful with the lower magnitude of shocks. The acceleration results for reduced objective mass (29.59kg) were similar or higher when compared with the analysis of 44.39kg of objective mass. This increase is due to

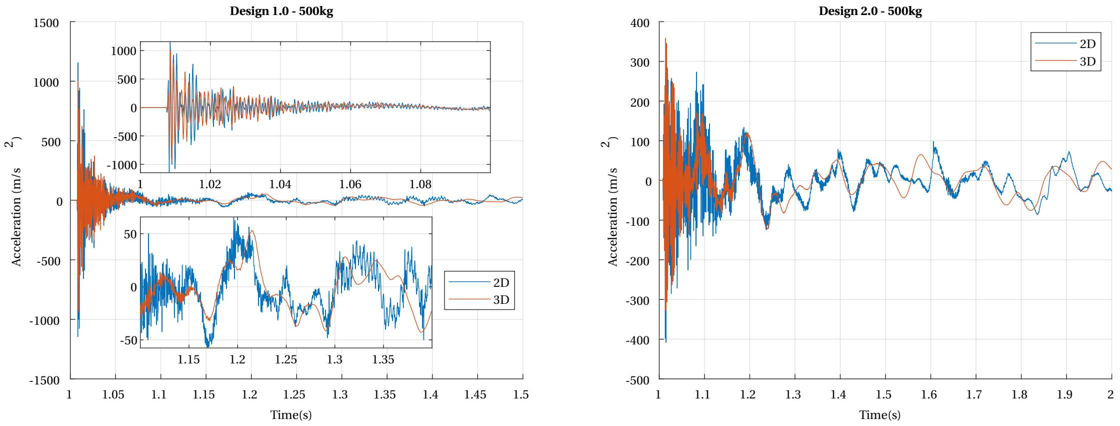

(a) Design 1.0 (b) Design 2.0

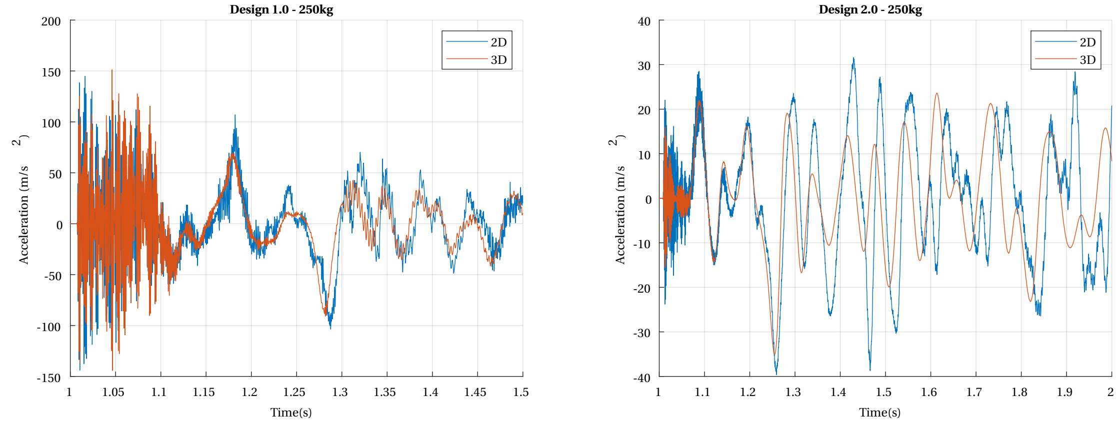

(c) Design 1.0 (d) Design 2.0

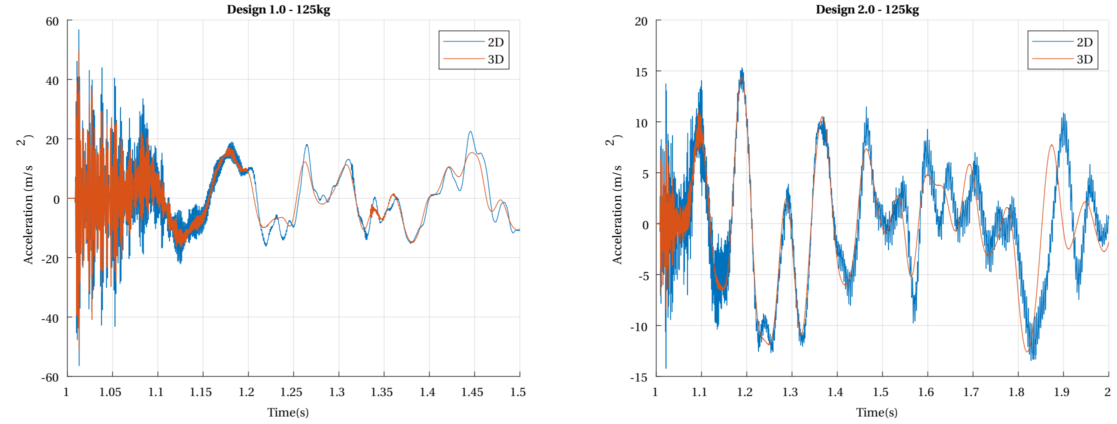

(e) Design 1.0 (f) Design 2.0

Figure 8.17: Comparing the acceleration time response of the objective mass for various loading conditions under 2D and 3D FE analysis for both the designs.

Explosive Charge	500kg	250kg	125kg
Design 1.0 (m/s^2)	Failure (1002.90)	168.14 (151.23)	61.24 (49.73)
Design 2.0 (m/s^2)	Failure (358.43)	41.24 (35.05)	14.15 (14.40)

Table 8.12: Maximum objective mass acceleration results obtained from the 3D analysis under 29.59kg of objective mass for both the designs, 3D results with 44.39kg of objective mass are shown in the bracket.

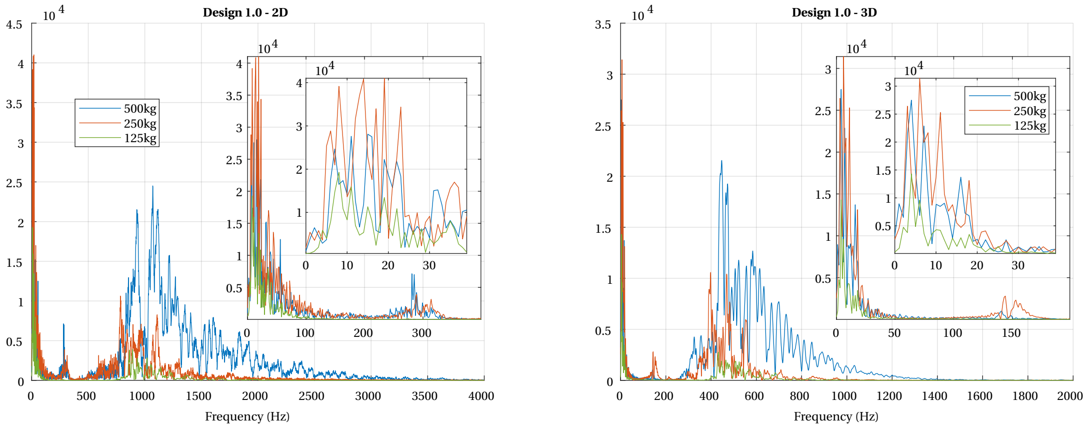

(a) Design 1.0 - 2D

(b) Design 1.0 - 3D

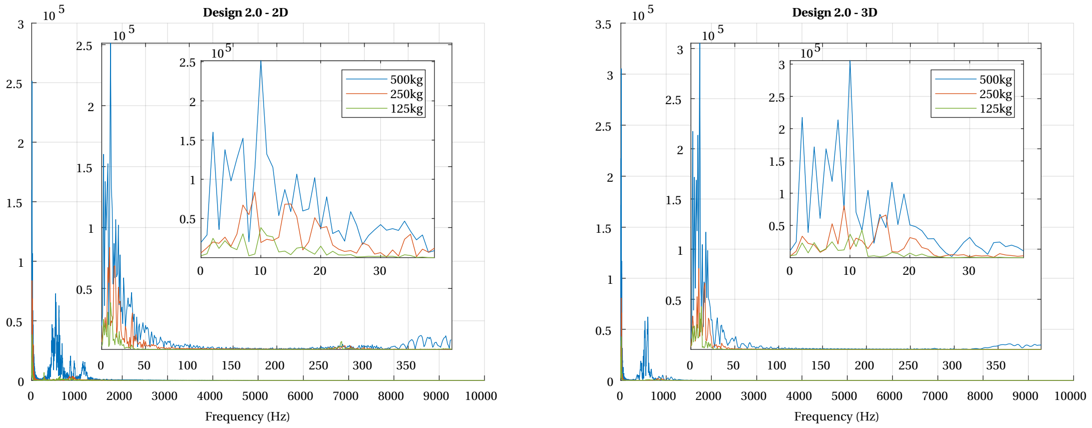

(c) Design 2.0 - 2D

(d) Design 2.0 - 3D

Figure 8.18: Comparing the acceleration frequency response of the objective mass for various loading conditions under 2D and 3D FE analysis for both the designs.

a lower preload and deformation experienced during the steady-state. This increases the vertical stiffness value and hence the objective mass experiences higher transmissibility. An increase in the objective mass has proved to reduce the transmissibility. For 59.18kg of objective mass, the acceleration experienced by the objective mass of Design 1.0 and Design 2.0 is $76.19 \mathrm{m/s}^2$ and $29.64 \mathrm{m/s}^2$ respectively. But the optimal design is more prone to static failure with an increase in objective mass.

8.6. DISCUSSION, LIMITATIONS AND RECOMMENDATIONS

The result of the parametric analysis provides the profile of the design space. The optimization provides with the virtual global optimum parameters. The best of the results from both the analysis is chosen and a design verification analysis in 3D is performed. The results of the 3D analysis are close to the 2D results. Therefore a cheap 2D analysis is sufficient for performing optimization. Computationally expensive 3D analysis can be used for verifying 2D results as performed in this study.

The results are also compared between Design 1.0 and Design 2.0. Design 1.0 provides an acceleration transmissibility of 11.363×10^{-3}, 2.981×10^{-3}, and 2.186×10^{-3} for 500kg, 250kg and 125kg of explosive mass respectively. Design 2.0 shows an acceleration transmissibility of 4.576×10^{-3}, 0.825×10^{-3}, and 0.592×10^{-3} for 500kg, 250kg and 125kg of explosive mass respectively. In all the cases the proposed Design 2.0 with the metallic interface shows an average acceleration transmissibility 3.263 times lower than Design 1.0. Design 2.0 shows better frequency response characteristics compared to Design 1.0. It performs relatively better under oblique loading and objective mass variations. Therefore Design 2.0 is the best candidate design to suppress large shocks arising due to an explosion.

8.6.1. LIMITATIONS

Given below are the limitations to be noted in this study:

1. No single design is confirmed from all the studies, three different design parameters are obtained for three different loading conditions. It can be postulated that designs optimized with higher shocks can be used for lower shock applications.
2. Boundary conditions are approximated and the interfaces are assumed to be perfect and intact. These might not be true in reality.
3. Horizontal loading on these designs is not tested. The presence of low stiffness in the lateral direction can make the shock mount vulnerable to lateral loading when used without the guide designed in Sec. 3.5.
4. The shock mount may not perform the same when used with eccentric loading. The mass needs to be balanced at the axis of the shock mount.
5. It can be postulated that when the mass increased, using multiple shock mounts in parallel can be non-compatible. The mass fitted in a balanced table provides eccentric loading on the shock mount, but during an uneven impact the balance is lost and the shock mount may not perform better. However, the shock mounts are tested for oblique shocks, with eccentric mass, and do perform satisfactorily.

8.6.2. RECOMMENDATIONS

Several recommendations for further research are given below:

1. Use of multiple metal interfaces in Design 2.0 and analyzing their performance.
2. Analysing Design 2.0 using the Tungsten metal interface. Tungsten having 2.14 times higher acoustic impedance than structural steel could reduce the overall coefficient of transmission, improving the performance of a shock mount with an interface.
3. Analysing the performance of multiple shock mounts in stacks to reduce the transmissibility.
4. Analysing the response of the shock mount under pure lateral loading.
5. Figuring out methods to handle and post-process huge data extracted from the Abaqus output file quickly. This proved a big challenge for these studies.
6. Analysing the response of the shock mount for greater time to know the complete characteristics of the response.
7. Optimizing the structure using multiple optimization algorithms to compare performance and converge the solution to obtain a global optimum.
8. Minimizing the shock response frequency of the shock mount.
9. Validating the results with experiments.

9

CONCLUSIONS

This thesis addresses the development and application of an optimization-based design approach for shock mounts. The study involved material model selection, conceptual shock mount design, shock wave description, performance simulation, shock mount optimization, and performance verification. The main findings regarding these 6 topics are given here. First, various material equations such as Neo-Hookean, Mooney-Rivlin, Arruda-Boyce, Polynomial, Yeoh, and Ogden material models have been compared to fit the uniaxial, biaxial, planar, and volumetric test data of Neoprene hyperelastic material. The Polynomial order 3 hyperelastic material model was found to fit the curves best and represented the material very closely. Hence the Neoprene hyperelastic material was modeled using the Polynomial order 3 hyperelastic material model with 9 constants and 3 incompressibility parameters.

Second, the shock wave that strikes the bottom hull of the ship was modeled analytically for three different explosive charges. The characteristics of such an impact wave were analyzed regarding the response of the ship. From the analytical model of the shock wave, the acceleration, velocity, and displacement experienced by the ship were plotted and used as the loading conditions for the shock mount.

Third, two candidate designs for modeling the shock mount have been proposed with the reason and inspiration behind their shape. Both the shock mounts were parameterized and the design integration was considered. Most parameters have been discussed with their importance in the design. Particularly Design 2.0 is a promising innovative design that is proposed as a result of this study. It contains a Neoprene-metal interface that reflects and transmits the incident wave proportionally, reducing the acceleration transmissibility to the objective mass. In principle, this design exploits the behavior of a wave at an interface. The theoretical performance and reasoning behind the shock mount are discussed in detail with equations and illustrations. Theoretically, the metal interface of Design 2.0 weakens the wave by about 8 times, compared to Design 1.0 which lacks such an interface. Hence only 12.4% of the incident large magnitude shock wave is transmitted across the interface.

Fourth, detailed FE modeling of the shock mount in the Abaqus FE package was discussed for a 2D axisymmetric and 3D geometry. The analysis was verified using sampling frequency and mesh convergence studies to get the results converged close to reality. In some situations, the FE model has been justified based on the balance between the computational cost and accuracy of the results. The outcome is an efficient automated FE model scripted in python that can analyze the shock mount for any given parameter in the geometry and shock. However, as expected modeling of these extreme phenomena is challenging and numerical problems were encountered. The reasoning for possible solver failures and errors was also discussed.

Fifth, multiple optimization algorithms have been compared and the BOBYQA algorithm was chosen as the best candidate algorithm for optimizing non-smooth problems with local minima. This algorithm was used in the shape optimization of the shock mount. Even though the optimizer was unable to converge to global optima, virtual global optima were computed and the results were compared with a standard discrete parametric study to come up with the best design parameters. This study is performed for a wave impact due to three explosive charges of 500kg, 250kg, and 100kg for both Designs 1.0 and Design 2.0.

Finally, the best results of the analysis were compared and verified using a 3D FE model. The result was found to be in good agreement and the time response was also observed to be similar. This makes 2D FEA efficient and reliable in the analysis and optimization of shock mounts. Design 1.0 was observed to have an acceleration transmissibility of 11.362×10^{-3}, 2.981×10^{-3}, and 2.186×10^{-3} under a blast wave load using 500, 250 and 125kg explosive charge respectively. Design 2.0 was observed to have an acceleration transmissibility of 4.576×10^{-3}, 0.825×10^{-3}, and 0.592×10^{-3} under a blast wave load using 500, 250 and 125kg explosive charge respectively. Design 2.0 has a 3.263 times average lower transmissibility than Design 1.0. The best designs have been further analyzed for different operating conditions, with a change of mass and an impact with an oblique shock. Both Design 1.0 and Design 2.0 performed satisfactorily under these conditions except for the highest shock with an explosive charge of 500kg, where the solver failed. The results were analyzed and discussed in both the time and frequency domain. The results in the frequency domain for the 3D analysis were satisfactory and lie within the stipulated limits when compared to the literature. The 3D analysis was observed to provide a lower shock response frequency compared to the 2D analysis. The acceleration transmitted to the objective mass was also within the limits compared to the literature.

The outcome of this report is the complete procedural analysis and design of a hyperelastic shock mount under a blast wave. A new Design 2.0 is proposed and is observed to perform 3.263 times better than Design 1.0 under identical shock loads. Design 2.0 is observed to perform relatively better under oblique shocks and objective mass variations. This design shows better frequency characteristics than Design 1.0 and completely filters out high-frequency components from the incoming shock. Therefore, Design 2.0 is proposed as the best candidate shock mount concept and design, which is a major outcome of this thesis. This work contributes to the research in the optimal design of shock mounts. The results are of interest to vibration and shock engineers especially maritime and defense applications.

Further research might well be conducted on optimizing the frequency bandwidth of the shock mount. In this study, this was evaluated after the optimization, but frequency characteristics could also be included in the design optimization phase. It is interesting to know the performance on this shock mount under lateral loading. In the current design, the shock mount is expected to be mounted in the upright position with a non-eccentric load, hence including various mounting positions and performance under eccentric loading is a good addition. Practical manufacturing and assembly of the shock mount are also crucial steps towards further validation and practical implementation.

REFERENCES

[1] R. de Borst and L. Sluys, *Computational Methods in Nonlinear Solid Mechanics* (TU Delft - CIE5142 Course Material, April 2015).

[2] Smarter Every Day, *Slow motion flipping cat physics,* `https://youtu.be/RtWbpyjJqrU` (2012).

[3] V. Giurgiutiu, *Chapter 5 - elastic waves,* in *Structural Health Monitoring with Piezoelectric Wafer Active Sensors (Second Edition)*, edited by V. Giurgiutiu (Academic Press, Oxford, 2014) second edition ed., pp. 199 – 292.

[4] R. H. Cole and R. Weller, *Underwater Explosions,* Physics Today **1**, 35 (1948).

[5] A. Keil, *The response of ships to underwater explosions*, Tech. Rep. (David Taylor Model Basin Washington DC, 1961).

[6] G. Lazzerini, *Ansys Explicit,* `https://www.ansys.com/-/media/ansys/en-gb/presentations/2017+customer+day+presentations/ansys-cd-2017-structures-iii-explicit-dynamcis.pdf?la=en-gb` (2017), [Online PPT; accessed December 2019].

[7] Abaqus, MIT, *Amplitude curves,* `https://abaqus-docs.mit.edu/2017/English/SIMACAEPRCRefMap/simaprc-c-amplitude.htm` (2017).

[8] Abaqus, MIT, *Schematic illustrations of deformation modes.* `https://abaqus-docs.mit.edu/2017/English/SIMA3DXRefImages/chyperelast-def-modes-nls.png` (2017).

[9] Ansys Inc., *Engineering Data,* Ansys 2019 R3.

[10] K. E. Zelik and A. D. Kuo, *Mechanical work as an indirect measure of subjective costs influencing human movement,* PLOS ONE **7**, 1 (2012).

[11] W. D. Reid, D. Science, T. O. (Australia), Aeronautical, and M. R. L. (Australia), *The response of surface ships to underwater explosions* (Melbourne, Vic. : DSTO Aeronautical and Maritime Research Laboratory, 1996) "AR-009-889" - Cover.

[12] H. Ucar and I. Basdogan, *Dynamic characterization and modeling of rubber shock absorbers: A comprehensive case study,* Journal of Low Frequency Noise, Vibration and Active Control **37**, 509 (2018), https://doi.org/10.1177/1461348417725954 .

[13] T. Sreekantamurthy, T. L. Turner, J. B. Moore, and J. Su, *Elastomeric structural attachment concepts for aircraft flap noise reduction-challenges and approaches to hyperelastic structural modeling and analysis,* in *55th AIAA/ASMe/ASCE/AHS/SC Structures, Structural Dynamics, and Materials Conference* (2014) p. 0509.

[14] Granta Design Limited, *CES EduPack 2019,* .

[15] W. E. Schevill, *Quiet power whaleboat,* The Journal of the Acoustical Society of America **44**, 1157 (1968).

[16] N. Kumar and V. V. Rao, *Hyperelastic mooney-rivlin model: determination and physical interpretation of material constants,* Parameters **2**, 01 (2016).

[17] Abaqus, MIT, *Abaqus cae user's guide / abaqus analysis user's guide,* `https://abaqus-docs.mit.edu/2017/English/SIMACAECAERefMap/simacae-c-gstconventions.htm#simacae-docconventinfo` (2017).

[18] R. S. Rivlin and G. I. Taylor, *Large elastic deformations of isotropic materials. ii. some uniqueness theorems for pure, homogeneous deformation,* Philosophical Transactions of the Royal Society of London. Series A, Mathematical and Physical Sciences **240**, 491 (1948), https://royalsocietypublishing.org/doi/pdf/10.1098/rsta.1948.0003 .

[19] R. S. Rivlin and E. K. Rideal, *Large elastic deformations of isotropic materials iv. further developments of the general theory,* Philosophical Transactions of the Royal Society of London. Series A, Mathematical and Physical Sciences **241**, 379 (1948), https://royalsocietypublishing.org/doi/pdf/10.1098/rsta.1948.0024 .

[20] E. M. Arruda and M. C. Boyce, *A three-dimensional constitutive model for the large stretch behavior of rubber elastic materials,* Journal of the Mechanics and Physics of Solids **41**, 389 (1993).

[21] R. S. Rivlin, D. W. Saunders, and E. N. D. C. Andrade, *Large elastic deformations of isotropic materials vii. experiments on the deformation of rubber,* Philosophical Transactions of the Royal Society of London. Series A, Mathematical and Physical Sciences **243**, 251 (1951), https://royalsocietypublishing.org/doi/pdf/10.1098/rsta.1951.0004 .

[22] O. H. Yeoh, *Some Forms of the Strain Energy Function for Rubber,* Rubber Chemistry and Technology **66**, 754 (1993), https://meridian.allenpress.com/rct/article-pdf/66/5/754/1942809/1_3538343.pdf .

[23] O. H. Yeoh, *Some forms of the strain energy function for rubber,* Rubber Chemistry and Technology **66**, 754 (1993), https://doi.org/10.5254/1.3538343 .

[24] R. W. Ogden and R. Hill, *Large deformation isotropic elasticity – on the correlation of theory and experiment for incompressible rubberlike solids,* Proceedings of the Royal Society of London. A. Mathematical and Physical Sciences **326**, 565 (1972), https://royalsocietypublishing.org/doi/pdf/10.1098/rspa.1972.0026 .

[25] Abaqus, MIT, *Bulk viscosity,* `https://abaqus-docs.mit.edu/2017/English/SIMACAEGSARefMap/simagsa-c-ovwbulkvisc.htm` (2017).

[26] P. K. Garu and T. K. Chaki, *Acoustic & mechanical properties of neoprene rubber for encapsulation of underwater transducers,* International Journal of Scientific Engineering and Technology **1**, 231 (2012).

[27] R. N. Capps, *Elastomeric materials for acoustical applications*, Tech. Rep. (Naval Research Lab Orlando (FL), 1989).

[28] A. K. Mathew, *Modeling Underwater Explosion (UNDEX) Shock Effects for Vulnerability Assessment in Early Stage Ship Design*, Ph.D. thesis, Virginia Tech (2018).

[29] T. Belytschko, W. K. Liu, B. Moran, and K. Elkhodary, *Nonlinear finite elements for continua and structures.* (John wiley & sons, 2013).

[30] J. C. Simo and T. J. Hughes, *Computational inelasticity*, Vol. 7 (Springer Science & Business Media, 2006).

[31] M. A. . R. Ansys Advanced Analysis Guide, *Chapter 5: Semi-implicit method,* `https://ansyshelp.ansys.com/account/secured?returnurl=/Views/Secured/corp/v193/ans_adv/Hlp_G_ADVSEMI.html` (2017).

[32] J. Overvelde, *Learn abaqus script in one hour,* `http://bertoldi.seas.harvard.edu/files/bertoldi/files/learnabaqusscriptinonehour.pdf` (2010).

[33] Abaqus, *Abaqus scripting reference guide,* `http://ivt-abaqusdoc.ivt.ntnu.no:2080/v6.14/books/ker/default.htm`.

[34] A. Mortazavi and V. Toğan, *Simultaneous size, shape, and topology optimization of truss structures using integrated particle swarm optimizer,* Structural and Multidisciplinary Optimization **54**, 715 (2016).

[35] W. A. Wall, M. A. Frenzel, and C. Cyron, *Isogeometric structural shape optimization,* Computer Methods in Applied Mechanics and Engineering **197**, 2976 (2008).

[36] C. Cartis, J. Fiala, B. Marteau, and L. Roberts, *Improving the flexibility and robustness of model-based derivative-free optimization solvers,* ACM Trans. Math. Softw. **45** (2019), 10.1145/3338517.

[37] A. Custódio, L. Vicente, and K. Scheinberg, *Methodologies and software for derivative-free optimization,* in *Advances and Trends in Optimization with Engineering Applications*, MOS-SIAM Book Series on Optimization, edited by T. Terlaky, M. Anjos, and S. Ahmed (Siam Society for Industrial and Applied, 2017) pp. 1–21.

[38] J. J. Moré and S. M. Wild, *Benchmarking derivative-free optimization algorithms,* SIAM J. Optimization **20**, 172 (2009).

[39] C. Cartis, J. Fiala, B. Marteau, and L. Roberts, *Improving the flexibility and robustness of model-based derivative-free optimization solvers,* (2018), arXiv:1804.00154 [math.OC] .

[40] C. Cartis, L. Roberts, and O. Sheridan-Methven, *Escaping local minima with derivative-free methods: a numerical investigation,* (2018), arXiv:1812.11343 [math.OC] .

[41] Python Library, *Using py-bobyqa,* `https://numericalalgorithmsgroup.github.io/pybobyqa/build/html/userguide.html` (2019).

[42] Department Of Defense, United States of America, *Shock tests, high-impact shipboard machinery, equipment, and systems, requirements,* MIL-S-901D(NAVY) (2017).

[43] Seagate Technology LLC, *BarraCuda,* `https://www.seagate.com/www-content/datasheets/pdfs/barracuda-2-5-DS1907-3-2005US-en_US.pdf` (2020).

[44] M. Möller, *Time stepping methods, ATHENS course: Introduction into Finite Elements,* `http://ta.twi.tudelft.nl/nw/users/matthias/teaching/athens/timestepping_2015.pdf` (2015), [Delft Institute of Applied Mathematics, TU Delft].

[45] J. Batoz and G. Dhatt, *Incremental displacement algorithms for nonlinear problems,* International Journal for Numerical Methods in Engineering **14**, 1262 (1979).

[46] E. Riks, *An incremental approach to the solution of snapping and buckling problems,* International Journal of Solids and Structures **15**, 529 (1979).

[47] M. Crisfield, *A fast incremental/iterative solution procedure that handles "snap-through",* in *Computational Methods in Nonlinear Structural and Solid Mechanics*, edited by A. K. Noor and H. G. McComb (Pergamon, 1981) pp. 55 – 62.

[48] M. A. Crisfield, *An arc-length method including line searches and accelerations,* International Journal for Numerical Methods in Engineering **19**, 1269 (1983).

[49] H. Hellweg and M. Crisfield, *A new arc-length method for handling sharp snap-backs,* Computers Structures **66**, 704 (1998).

[50] J. Ferreira and A. Serpa, *Application of the arc-length method in nonlinear frequency response,* Journal of Sound and Vibration **284**, 133 (2005).

[51] R. Courant, K. Friedrichs, and H. Lewy, *On the partial difference equations of mathematical physics,* IBM Journal of Research and Development **11**, 215 (1967).

[52] Y. D. Kwon, S. B. Kwon, X. Lu, and H. W. Kwon, *A finite element procedure with poisson iteration method adopting pattern approach technique for near-incompressible rubber problems,* Advances in Mechanical Engineering **6**, 272574 (2014), https://doi.org/10.1155/2014/272574 .

[53] T. J. Hughes, *The finite element method: linear static and dynamic finite element analysis* (Courier Corporation, 2012).

[54] K. J. Bathe, *Finite element procedures* (Klaus Jürgen Bathe, 2006).

This page is intentionally left blank.

A

MATERIAL MODELS

A.1. HYPERELASTIC MATERIAL MODELS

A.1.1. POLYNOMIAL HYPERELASTIC MATERIAL MODEL

Rivlin and Saunders[21] introduced the polynomial hyperelastic material model in 1951. This model expresses the elastic strain energy density function (ψ) in terms of two deviatoric strain invariants $\bar{I}_1$ and $\bar{I}_2$ of the left Cauchy-Green deformation tensor. The primary polynomial material model is given by,

$$\psi = \sum_{i,j=0}^{N} C_{ij}\left(\bar{I}_1 - 3\right)^i \left(\bar{I}_2 - 3\right)^j \qquad \text{, where } C_{00} = 0. \tag{A.1}$$

When volumetric test data is available, compressibility can be added to the Eq. A.1, which gives the complete polynomial hyperelastic material model,

$$\psi = \sum_{i,j=0}^{N} C_{ij}\left(\bar{I}_1 - 3\right)^i \left(\bar{I}_2 - 3\right)^j + \sum_{i=0}^{N} \frac{1}{D_i}\left(J^{el} - 1\right)^{2i} \qquad \text{, where } C_{00} = 0. \tag{A.2}$$

Here ψ is the strain energy per unit reference volume, C_{ij} and D_i are the material constants/parameters where D_i governs compressibility. $N \in \mathbb{N}$ is the order of the material model. First and second deviatoric strain invarients $\bar{I}_1$ and $\bar{I}_2$ are given by Eq. A.3.

$$\begin{aligned} &\bar{I}_1 = \bar{\lambda}_1^2 + \bar{\lambda}_2^2 + \bar{\lambda}_3^2 \\ &\bar{I}_2 = \bar{\lambda}_1^{(-2)} + \bar{\lambda}_2^{(-2)} + \bar{\lambda}_3^{(-2} \quad \text{where, } \bar{\lambda}_i = J^{-\frac{1}{3}} \lambda_i \end{aligned} \tag{A.3}$$

here, $\bar{\lambda}_i$ are the deviatoric stretches, λ_i are the principal stretches and J is the total volume ratio. The initial shear modulus (μ_0) and bulk modulus (K_0) are given in Eq. A.4.

$$\begin{aligned} \mu_0 &= 2(C_{10} + C_{01}) \\ K_0 &= \frac{2}{D_1} \end{aligned} \tag{A.4}$$

Certain material models such as Mooney-Rivlin, Neo-Hookean, Reduced-Polynomial, and Yeoh can be obtained from polynomial material Eq. A.2, by having special choices of C_{ij} and N.

Mooney-Rivlin 2 parameter hyperelastic material model can be considered a specific case of polynomial hyperelastic material model obtained by setting $N = 1$ and $C_{11} = 0$ in Eq. A.2, as shown in Eq. A.5.

$$\psi = C_{10}\left(\bar{I}_1 - 3\right) + C_{01}\left(\bar{I}_2 - 3\right) + \frac{1}{D_1}\left(J^{el} - 1\right)^2 \tag{A.5}$$

Neo-Hookean hyperelastic material model can be obtained by setting $N = 1$, $C_{01} = 0$ and $C_{11} = 0$ in Eq. A.2, as shown in Eq. A.6.

$$\psi = C_{10}\left(\bar{I}_1 - 3\right) \tag{A.6}$$

Reduced-Polynomial hyperelastic material model can be obtained by setting $j = 0$ in Eq. A.2, as shown in Eq. A.7.

$$\psi = \sum_{i=0}^{N} C_{i0}\left(\bar{I}_1 - 3\right)^i + \sum_{i=0}^{N} \frac{1}{D_i}\left(J^{el} - 1\right)^{2i} \tag{A.7}$$

Yeoh's hyperelastic 3$^{\text{rd}}$ order material model can be obtained by setting $N = 3$ and $j = 0$ in Eq. A.2, as shown in Eq. A.8.

$$\psi = C_{10}\left(\bar{I}_1 - 3\right) + C_{20}\left(\bar{I}_1 - 3\right)^2 + C_{30}\left(\bar{I}_1 - 3\right)^3 + \frac{1}{D_1}\left(J^{el} - 1\right)^2 + \frac{1}{D_2}\left(J^{el} - 1\right)^4 + \frac{1}{D_3}\left(J^{el} - 1\right)^6 \tag{A.8}$$

All these material models are compared using the Neoprene experimental data as discussed in section Sec. 2.3.1 .

A.1.2. HYPERELASTIC MATERIAL STABILITY

The quality of the fit to experimental data is judged using the concept of material or Drucker stability. It is verified for all the three modes present as shown in Fig. A.1.

For an incompressible material, the Drucker stability criterion requires that the change in stress, $\mathrm{d}\sigma$, due to an infinitesimal change in the logarithmic strain, $\mathrm{d}\epsilon$, satisfies the inequality Eq. A.9.

$$\mathrm{d}\sigma : \mathrm{d}\epsilon > 0 \tag{A.9}$$

Applying $\mathrm{d}\sigma = \mathbf{D} : \mathrm{d}\epsilon$, where $\mathbf{D}$ is the tangent material stiffness, Eq. A.9 becomes

$$\mathrm{d}\epsilon : \mathbf{D} : \mathrm{d}\epsilon > 0. \tag{A.10}$$

To satisfy Eq. A.10, $\mathbf{D}$ should be positive-definite. The inequality of Eq. A.10 can be represented in terms of principal stresses and strains for an isotropic elastic formulation, as shown in Eq. A.11.

$$\mathrm{d}\sigma_1 \mathrm{d}\epsilon_1 + \mathrm{d}\sigma_2 \mathrm{d}\epsilon_2 + \mathrm{d}\sigma_3 \mathrm{d}\epsilon_3 > 0 \tag{A.11}$$

Any value can be chosen for hydrostatic pressure without affecting the strains since the material is taken to be incompressible. It is convenient to choose σ_3=$\mathrm{d}\sigma_3 = 0$, which allows us to ignore the third term.

Changes in stress and strain can be computed using Eq. A.12.

$$\begin{pmatrix} \mathrm{d}\sigma_1 \\ \mathrm{d}\sigma_2 \end{pmatrix} = \begin{pmatrix} D_{11} & D_{12} \\ D_{21} & D_{22} \end{pmatrix} = \begin{pmatrix} \mathrm{d}\epsilon_1 \\ \mathrm{d}\epsilon_2 \end{pmatrix} \tag{A.12}$$

Here, $\mathbf{D}$ must be positive-definite for material stability, hence it should satify Eq. A.13

$$\begin{aligned} D_{11} + D_{22} > 0 \\ D_{11}D_{22} - D_{12}D_{21} > 0 \end{aligned} \tag{A.13}$$

where, D_{ij}, tangent stiffness matrix, is a function of stretch ratios $\lambda_1, \lambda_2, \lambda_3$.

Abaqus, the FE software platform that will be used in this thesis, performs a check on the stability for all six (tension and compression in all three modes) different forms of loading for most material models, including the polynomial material model[17].

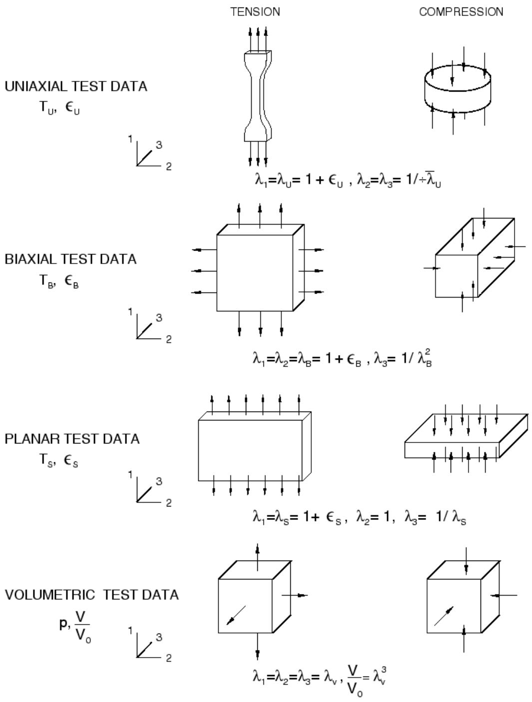

Figure A.1: Schematic illustration of deformation modes under which tests results are obtained[8].

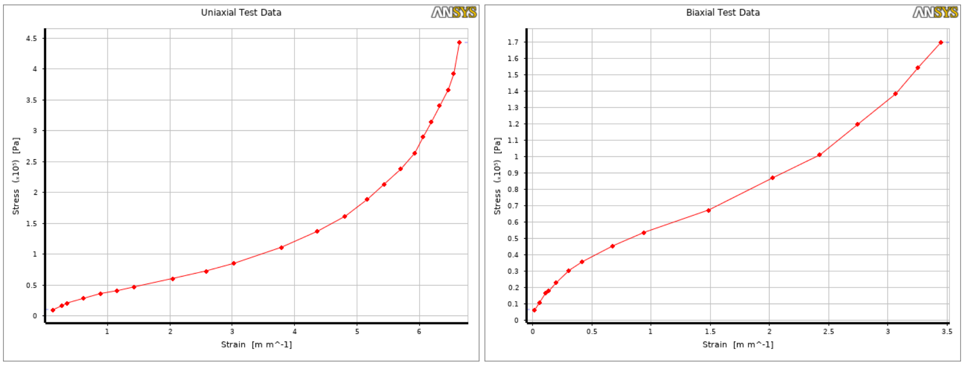

(a) Uniaxial Test Data

(b) Biaxial Test Data

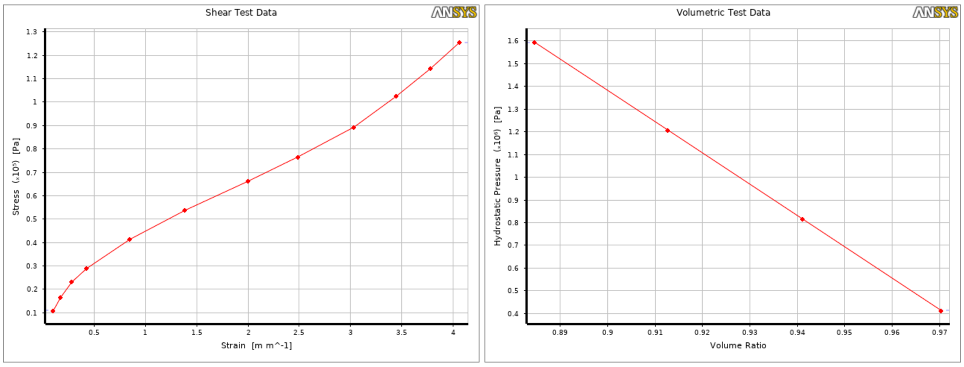

(c) Shear / Planar Test Data

(d) Volumetric Test Data

Figure A.2: Plot showing the test data obtained for neoprene material as obtained from Ansys material library[9].

A.1.3. MATERIAL TEST DATA

Test results are combined from all the three test modes to obtain a better characterization of the hyperelastic material behavior. Stress-strain relationships for different tests are obtained using derivatives of strain energy function with respect to the strain invariants, for the incompressible material model.

A.2. NEOPRENE MATERIAL TEST DATA

Neoprene material test data used in the hyperelastic material modeling is given in this section.

A.2.1. UNIAXIAL TEST DATA

Strain (mm^{-1})	Stress (Pa)
0.1338	10691.01486
0.2675	16800.46169
0.3567	21382.71919
0.6242	29019.35536
0.8917	36655.99154
1.1592	41237.55956
1.4268	47347.0064
2.051	61093.08941
2.586	73311.2936
3.0318	85530.18728
3.7898	111494.4745
4.3694	137458.7617
4.8153	161895.8596
5.172	189388.0256
5.4395	213825.1235
5.707	238262.2213
5.9299	264226.5085
6.0637	290190.7957
6.1975	314627.8936
6.3312	340592.1808
6.465	366557.1575
6.5541	392521.4447
6.6433	442922.8298

Table A.1: Neoprene Hyperelastic Material Uniaxial Test Data.

A.2.2. BIAXIAL TEST DATA

Strain (mm^{-1})	Stress (Pa)
0.02	6470.042784
0.06	10962.6684
0.11	16607.40841
0.14	18078.06072
0.2	22918.18224
0.31	30528.61833
0.42	35735.54108
0.68	45521.96342
0.94	53637.09594
1.49	67470.05293
2.03	87115.98208
2.43	101217.8347
2.75	119968.824
3.07	138624.6656
3.26	154788.741
3.45	169976.5183

Table A.2: Neoprene Hyperelastic Material Biaxial Test Data.

A.2.3. SHEAR / PLANAR TEST DATA

Strain (mm^{-1})	Stress (Pa)
0.1034	11031.616
0.1724	16547.424
0.2828	23166.3936
0.4276	28957.992
0.8483	41368.56
1.3862	53779.128
2	66189.696
2.4897	76669.7312
3.0345	89356.0896
3.4483	102594.0288
3.7793	114315.1208
4.0621	125484.632

Table A.3: Neoprene Hyperelastic Material Biaxial Test Data.

A.2.4. VOLUMETRIC TEST DATA

Volume Ratio	Hydrostatic Pressure (Pa)
0.8847	1593379.036
0.9127	1207961.952
0.9412	814960.632
0.9703	413685.6

Table A.4: Neoprene Hyperelastic Material Volumetric Test Data.

B

SHOCK MOUNT DESIGN

Figure below shows the three stages involved in a human jump.

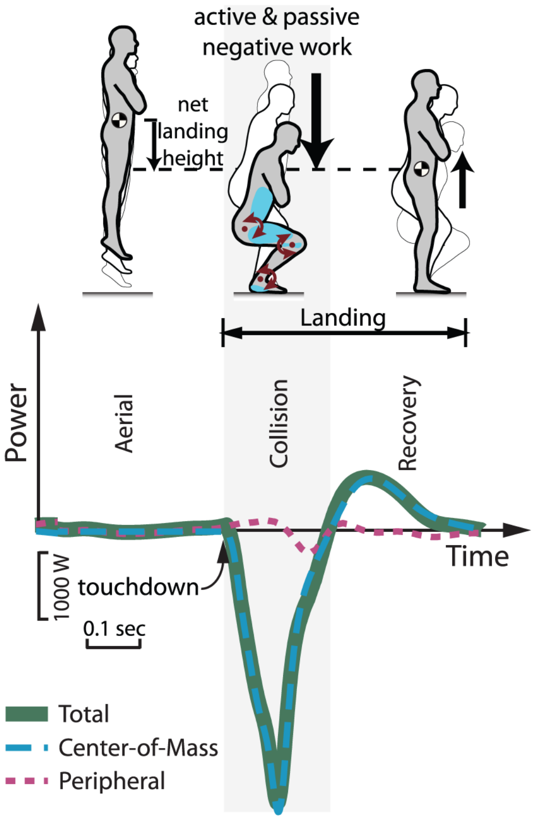

Figure B.1: Three stages during human landing after a jump.[10]

C

MODELING SHOCK

C.1. PYTHON SCRIPT

The python script used to model the vertical displacement of the ship due to an underwater explosion event is provided below;

```
ttime = 1 #Total Time = 1s
def loading():
    #Parameters
    rho = 1025.0 #kg/m^3 Density Of Sea Water
    c = 1500.0 #m/s Speed Of Sound In Water
    w = 500.0 #kg Mass Of Explosive
    r = 10.0 #m Distance To Rigid Plate / Stand Off Distance


    time = np.append(np.arange(0,0.006,0.00001),np.arange(0.006,ttime+.006,0.006))

    m = 3000.0 #Tons Mass Of Ship
    a = 1500.0 #m^2 Area Of Hull

    P0 = 52.4*((w**(1.0/3.0)/r)**1.18)*(10.0**6.0)
    theta = 0.084*w**(1.0/3.0)*(w**(1.0/3.0)/r)**(-0.23)/1000.0

    mp = m*1000.0/a #kg/m^2 Mass Per Unit Area
    beta = rho*c*theta/mp #Dimensionless

    alpha = 0.0 #deg Angle Of Incidence
    alpha = alpha*math.pi/180.0
    eta = 0.5 #Experiments
    Cf = 1 #Ship Type, Location Aboard Ship, Type Of Installation

    #Displacement
    intcons = -2*P0*(theta**2)/(mp*(1-beta))*(1-1/beta)
    sf = Cf*w**(1.0/2.0)/r*(eta+(1-eta)*cos(alpha))

    ans = []
    for t in time:
        disp = 2.0*P0*(theta**2)/(mp*(1-beta))*(math.exp(-t/theta)-math.exp(-beta*t/theta)/beta)+i
        ans = ans + [[t,disp*sf]]
    return ans
```

C.2. SEQUENCE OF EVENTS

A super-heated, highly compressed gas bubble is formed along with the generation of a shock wave in the surrounding water during the sudden release of energy associated with an explosion. An exponentially decaying pressure wave propagates as a spherical pressure wave initially at speeds much faster than the speed of sound in water and rapidly dropping to sound velocity. The gas bubble begins to expand in size (overshooting the equilibrium condition between hydro-static pressure and gas pressure) at the same time the gas pressure in the bubble gradually decreases. At the outset of reaching a maximum radius with minimum pressure, the bubble starts to contract initially slowly and later rapidly reaching a minimum radius. This generates large pressures in the bubble and the bubble begins to expand again. This process continues creating a cycle of events[5].

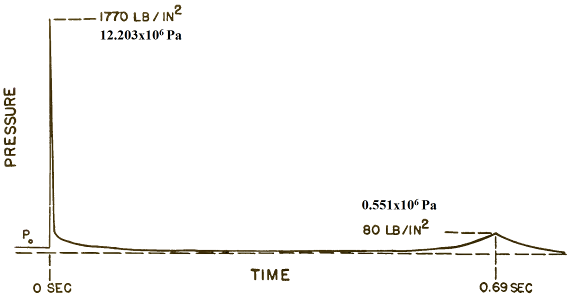

Figure C.1: Pressure at 60 feet (18.288 m) from a 300 pound (136 kg) TNT charge ignited at 50 feet (15.24 m) below the surface[4].

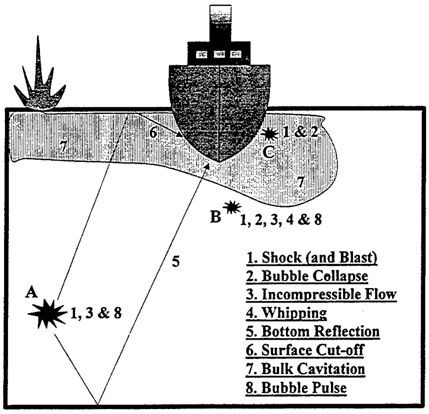

Figure C.2: Sequence of events during shock-wave propagation along with their location[11].

At each re-compression, additional pressure pulses are emitted which are not shock waves and they become weaker with each oscillation. The first of such bubble pulses can have a peak pressure of 10 to 15 percent of the shock wave peak pressure. The relation between the shock wave and bubble pulse pressures along with its duration is shown in Fig. C.1. A considerable amount of energy present initially is lost during each pulse making successive pulses weaker. Therefore generally only the first pulse is of practical significance.[4] Sequence of events during shock-wave propagation along with their location is shown in Fig. C.2.

D

Finite Element Modeling

D.1. Governing Equation[1]

The problem is discretized in the spatial domain to obtain semi-discretized forms and in the time domain to arrive at the fully discretized set of equations employing finite element representation of virtual work.

The equations of motion of an elementary volume V without damping in a general three dimensional continuum can be written as,

$$\mathbf{L}^{\mathbf{T}}\sigma + \mathbf{p} = \mathbf{R}\ddot{\mathbf{u}} \tag{D.1}$$

where, σ is the vector containing stress components $(\sigma_{xx}, \sigma_{yy}, \sigma_{zz}, \sigma_{xy}, \sigma_{yz}, \sigma_{zx})$, $\mathbf{u}$ is the vector of the displacement components (u_x, u_y, y_z), $\mathbf{R}$ is the density matrix equal to $diag[\rho, \rho, \rho]$ and $\mathbf{p}$ is the assembled body forces.

The kinematic equations is given by

$$\epsilon = \mathbf{L}\mathbf{u} \tag{D.2}$$

where, ϵ is the set of strain components and $\mathbf{L}$ is the matrix differential operator.

The constitutive equations for the nonlinear material behavior is generally given in the rate form by,

$$\dot{\sigma} = \mathbf{D_i}\dot{\epsilon} \tag{D.3}$$

where, $\mathbf{D_i}$ matrix is the nonlinear tangent stiffness moduli.

D.2. Finite Element Formulation[1]

D.2.1. Weak Formulation

Weak form of the Eq. D.1 is obtained by replacing the equation of motion with the virtual work equation,

$$\int_V \partial\mathbf{u}^{\mathbf{T}}[\mathbf{L}^{\mathbf{T}}\sigma - \mathbf{R}\ddot{\mathbf{u}} + \mathbf{p}]dV = 0 \tag{D.4}$$

Using Green's theorem the general virtual work equation for linear and nonlinear problems is obtained, with no assumptions made w.r.t material behavior, and is given by,

$$\int_V \partial\mathbf{u}^{\mathbf{T}}[\mathbf{R}\ddot{\mathbf{u}}]dV + \int_V \partial\epsilon^{\mathbf{T}}\sigma dV = \int_V \partial\mathbf{u}^{\mathbf{T}}\mathbf{p}dV + \int_V \partial\mathbf{u}^{\mathbf{T}}\mathbf{t}dS \tag{D.5}$$

Semi-discretization of the above equation is obtained using the interpolation of the continuous displacement field ($\mathbf{u} = \mathbf{H}\mathbf{a}$), interpolation of the continuous acceleration field ($\mathbf{u} = \mathbf{H}\ddot{\mathbf{a}}$) (where, Matrix $\mathbf{H}$ contains the interpolation polynomial and $a, \ddot{a}$ are nodal displacements and accelerations respectively) and relation between strains and the nodal displacements ($\dot{\epsilon} = \mathbf{B}\dot{\mathbf{a}}$). Semi-discrete equation of motion governing the response of a linear or nonlinear system of finite elements that will be used for explicit time integration as discussed in Sec. D.3.1 is given by,

$$\mathbf{M}\ddot{\mathbf{a}}^{\mathbf{t}} = \mathbf{f}_{\mathbf{e}}^{\mathbf{t}} - \mathbf{f}_{\mathbf{i}}^{\mathbf{t}} \tag{D.6}$$

where, $\mathbf{M} = \int_V \mathbf{H}^{\mathbf{T}}\mathbf{R}\mathbf{H}\mathrm{d}V$ is the mass matrix, $\mathbf{f}_{\mathbf{e}}^{\mathbf{t}} = \int_V \mathbf{H}^{\mathbf{T}}\mathbf{p}^{\mathbf{t}}\mathrm{d}V + \int_V \mathbf{H}^{\mathbf{T}}\mathbf{t}^{\mathbf{t}}\mathrm{d}S$ is the external load vector and $\mathbf{f}_{\mathbf{i}}^{\mathbf{t}} = \int_V \mathbf{B}^{\mathbf{T}}\sigma^{\mathbf{t}}\mathrm{d}V$ is the internal load vector.

Using suitable substitutions for stress and strain in virtual work Eq. D.5 at time $t+\Delta t$, the semi-discrete nonlinear equation of motion that will be used for implicit time integration is given by,

$$\mathbf{M}\ddot{\mathbf{a}}^{\mathbf{t}+\Delta\mathbf{t}} + \mathbf{K}^{\mathbf{t}}\Delta\mathbf{a} = \mathbf{f}_{\mathbf{e}}^{\mathbf{t}+\Delta\mathbf{t}} - \mathbf{f}_{\mathbf{i}}^{\mathbf{t}} \tag{D.7}$$

where , $\mathbf{K}^{\mathbf{t}} = \int_V \mathbf{B}^{\mathbf{T}}\mathbf{D}_{\mathbf{i}}^{\mathbf{t}}\mathbf{B}\mathrm{d}V$ is the tangential stiffness matrix and $\mathbf{f}_{\mathbf{e}}^{\mathbf{t}+\Delta\mathbf{t}} = \int_V \mathbf{H}^{\mathbf{T}}\mathbf{p}^{\mathbf{t}+\Delta\mathbf{t}}\mathrm{d}V + \int_S \mathbf{H}^{\mathbf{T}}\mathbf{t}^{\mathbf{t}+\Delta\mathbf{t}}\mathrm{d}S$. The tangential stiffness matrix is nonlinear and can cause issues in convergence during implicit time integration.

D.2.2. EXPLICIT TIME INTEGRATION

An explicit time integration can have major advantages in reducing the computation effort per time step. It is easy to implement and parallelize. Storage of the system matrices and factorization of the stiffness matrix is not required in the explicit scheme when using lumped mass matrices. Shortcomings of the explicit method are the time step restriction and the absence of knowing whether the exact path of dynamic equilibrium has been traced. The first issue concerns the stability of the solution and is discussed in solution methods Sec. D.3.1. The second issue concerns the accuracy of the solution and is important for nonlinear problems. For determining the state variables at time $t+\Delta t$, strong nonlinearities during a time step are not taken into account. This gives rise to small solution errors that are not corrected and get accumulated causing significant solution errors making the numerical solution to drift from equilibrium for large time steps and nonlinearity[1]. It is highly inefficient for solution of stationary problems unless local time-stepping (i.e $\Delta t = \Delta t(x)$ is used [44].

D.2.3. IMPLICIT TIME INTEGRATION

Implicit time stepping is stable over a wide range of time steps, sometimes unconditionally. They are excellent iterative solvers for steady-state problems. They are difficult to implement and parallelize at a higher cost per time step. They are insufficiently accurate for truly transient problems at large Δt. The convergence of linear solvers deteriorates/fails with an increase in Δt[44].

D.3. SOLUTION METHODS

Solution methods used to solve nonlinear problems use incremental iterative solvers/methods rather than using direct methods. Batoz and Gouri[45] proposed incremental displacement algorithms to solve nonlinear structural stability problems. They proposed two algorithms Newton-Raphson (N-R) and its modified version, which are self-correcting (stiffness changes at every iteration) and standard incremental (stiffness is kept constant throughout the iteration) methods respectively. Crisfield modified the Riks[46] solution model in conjunction with modified N-R, making it suitable for use in FEM handling snap-through. He also applies the algorithm to a large deflection analysis of a shallow elastic shell[47]. This leads him to develop a stable arc-length method that is more robust to snap-back and snap-through. It can represent/follow the load-displacement curve completely but it comes at a cost. The use of the arc-length method in FEA for large deflection analysis of thin plates and shallow shells is shown by Crisfield [48]. The modified arc-length method is proposed to represent very sharp snap-backs for use in fracture mechanics[49]. N-R or modified N-R are unable to deal with limit points and are unstable in problems with these features. By solving a system of nonlinear equations, the nonlinear frequency response curve for a nonlinear dynamic system is obtained using the arc-length method, for a system with large strain and large displacement [50].

D.3.1. EXPLICIT TIME INTEGRATION SOLUTION PROCEDURE

To solve semi-discretised equation of motion Eq. D.6, central difference approximations for velocity and acceleration is adopted. The algorithm for explicit time integration is provided below:

1. Select a time step Δt smaller than the critical time step.

2. Calculate constants $c_1 = 1/(\Delta t^2), c_2 = 1/(2\Delta t)$.
3. Initialise: $\mathbf{a}^0, \dot{\mathbf{a}}^0, \ddot{\mathbf{a}}^0$, $t = 0$s.
4. Compute: $\mathbf{a}^{-\Delta t} = \mathbf{a}^0 - \Delta t \dot{\mathbf{a}}^0 + (\Delta t^2/2)\ddot{\mathbf{a}}^0$.
5. Compute: $\hat{\mathbf{M}} = c_1 \mathbf{M}$
   $\hat{\mathbf{f}} = \mathbf{f}_e^t - c_1 \mathbf{M}(\mathbf{a}^{t-\Delta t} - 2\mathbf{a}^t) - \mathbf{f}_i^t$.
6. Solve for total displacements: $\hat{\mathbf{M}}\mathbf{a}^{t-\Delta t} = \hat{\mathbf{f}}$.
7. Calculate incremental displacement field: $\Delta \mathbf{a} = \mathbf{a}^{t+\Delta t} - \mathbf{a}^t$.
8. Update internal force vector for next step: $\mathbf{f}_i^{t+\Delta t} = f(a^{t+\Delta t})$.
9. Calculate new accelerations and velocities:

$$\ddot{\mathbf{a}}^t = c_1(\mathbf{a}^{t-\Delta t} - 2\mathbf{a}^t + \mathbf{a}^{t+\Delta t})$$
$$\dot{\mathbf{a}}^t = c_2(-\mathbf{a}^{t-\Delta t} + \mathbf{a}^{t+\Delta t})$$

10. Next time step increment $t = t + \Delta t$ and go to step 5.

It is important to not take a time step bigger than the diffusion rate (of energy, mass, force, pressure, etc.) in the element, given a space discretization[51]. Practically the time step must be kept small allowing time for the information to propagate through space discretization. Equations relating to critical time step and characteristic length (l) of the smallest element in the mesh are shown in Eq. D.8 and Eq. D.9 according to Courant-Friedrich-Levy (CFL) condition.

$$\delta t \leq \delta t^{critical} \qquad \text{where } \delta t^{critical} = \frac{l}{c} \tag{D.8}$$

where c is the speed of sound in the material given by:

$$c = \sqrt{\frac{E(1-\nu)}{\rho(1+\nu)(1-2\nu)}}. \tag{D.9}$$

It can be seen from Eq. D.9 that, as ν tends to 0.5, c tends to infinity and $\delta t^{critical}$ tends to zero. This shows that incompressible materials should be analyzed with very small time steps. Using near-incompressible material assumption with a Poisson ratio of $0.4\bar{9}$ in the analysis is the method to solve incompressibility. It is shown that using 0.49 can bring fast convergence, but a maximum displacement discrepancy of 14% is observed when using $\nu = 0.49$ and 0.4999 for rubber. Using many decimals in the approximation of Poisson ration can also lead to divergence of the solution[52].

The Courant condition as given by Hughes[53] and Bathe[54] states,

$$\Delta t = \frac{2}{\omega_{max}} \tag{D.10}$$
$$\omega_{max} \leq \omega^e_{max} \tag{D.11}$$

where ω_{max} is the highest frequency of the total system. ω^e_{max} is the maximum frequency of a single finite element and is calculated from $\det(\mathbf{K}^e - (\omega^e_{max})^2\mathbf{M}^e) = 0$, where ($\mathbf{K}^e$ and ($\mathbf{M}^e$ are the element mass and tangent stiffness matrices. Δt is the critical time step for a specific element configuration. For nonlinear problems with softening (w^e_{max} becomes imaginary), a critical time step cannot be obtained and it is unclear if a stable time step exists for explicit time integration. Often a smaller time step than obtained from Courant condition is required for the integration of nonlinear problems[1].

D.4. PARTITIONING OF THE GEOMETRY IN 3D MESHING

The figure shows the planes used for partitioning the geometry and the cut cross-section of the partitioned part.

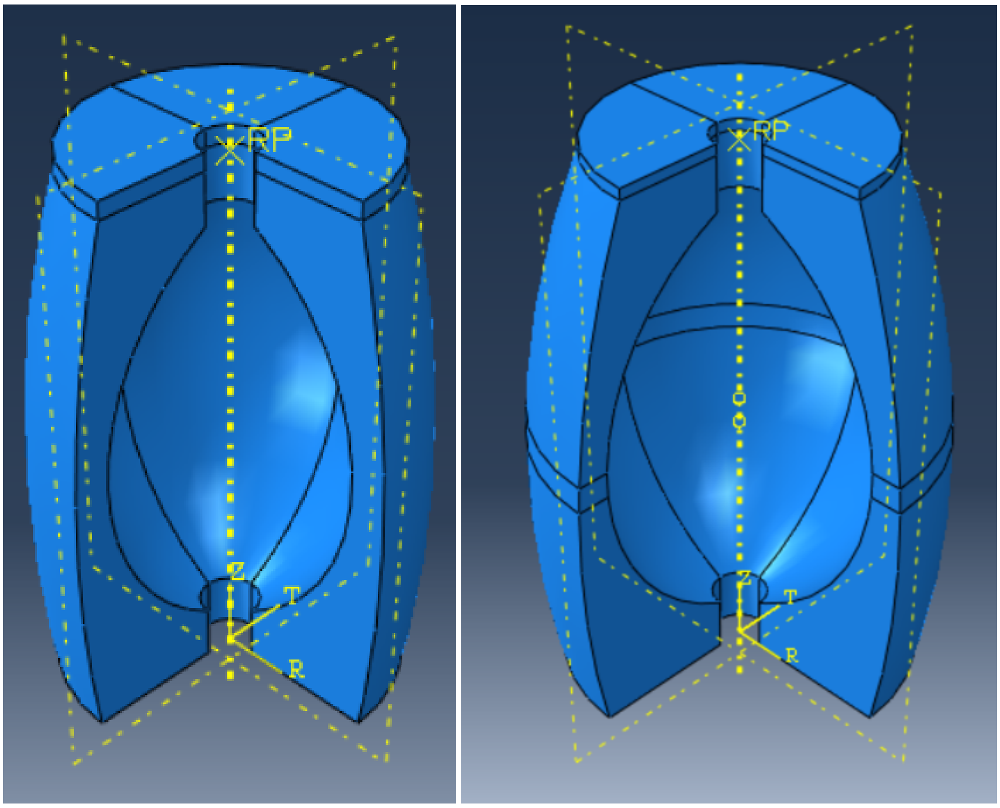

(a) Design 1.0

(b) Design 2.0

Figure D.1: Cut section of the partitioned geometry for both designs before meshing in 3D.

E

Optimization Method

E.1. Validation

The plot of the objective function over the entire design space is shown in Fig. E.1.

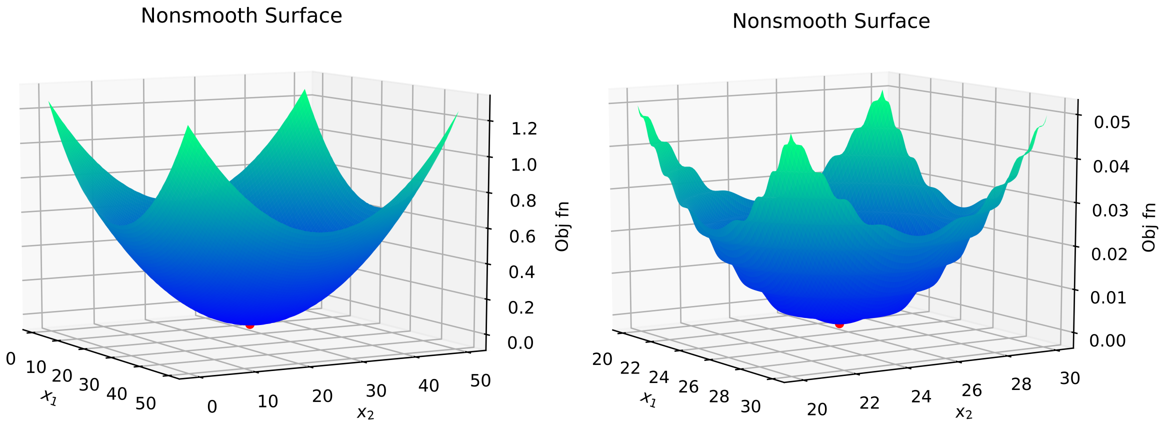

(a) Entire design space

(b) Magnified

Figure E.1: Plot of the objective function over design space where the red point shows the location of the objective minimum.

The minimum objective function values and optimized design variables obtained while using different optimization algorithms is compared in Tab. 6.1, Tab. E.1, Tab. E.2, Tab. E.3, when the optimization algorithm is initialized from multiple points respectively.

Algorithm	No. Of Fn. Eval.	No. Of Iter.	f_{min}	x_{min}
Py-BOBYQA	47	2	2.49e-14	[24.99999689 25.00000167]
BFGS	60	5	5.03e-11	[24.99988789 24.99988789]
Nelder - Mead	119	63	2.45e-16	[24.99999966 25.0000001]
Powell	85	4	0.0	[25.0 25.0]
COBYLA	75	1	2.01e-11	[25.00004553 25.00008931]

Table E.1: Initial Point: [50,50]

Algorithm	No. Of Fn. Eval.	No. Of Iter.	f$_{min}$	x_{min}
Py-BOBYQA	48	2	2.49e-14	[25.00000311 24.99999833]
BFGS	56	3	1.85e-08	[24.9978458 24.9978458]
Nelder - Mead	127	75	3.04e-16	[24.99999967 24.99999979]
Powell	88	4	0.0	[25.0 25.0]
COBYLA	71	1	9.09e-12	[24.99993292 24.9999931]

Table E.2: Initial Point: [0,0]

Algorithm	No. Of Fn. Eval.	No. Of Iter.	f$_{min}$	x_{min}
Py-BOBYQA	26	2	0.0	[25. 25.]
BFGS	4	1	0.0	[25. 25.]
Nelder - Mead	87	43	0.0	[25. 25.]
Powell	21	1	0.0	[25.0 25.0]
COBYLA	25	1	2e-11	[25.00003506 25.00009365]

Table E.3: Initial Point: [25,25]

F

SHOCK MOUNT DESIGN OPTIMIZATION RESULTS

F.1. PYTHON SCRIPTING

The python scripting methodologies used in the design optimization studies are discussed in this section.

F.1.1. PARAMETRIC STUDY PYTHON SCRIPTING

The analysis is modularized into function files. Initially, the Abaqus CAE python script is used to generate input files for all the design points. Then all the input files are submitted as a job and analyzed using the explicit solver to generate the output ".odb" file. The explicit analysis is the most time-consuming process and this can be executed parallelly depending on the available free licenses (each analysis uses 5 licenses when executed using 1 core, and uses 1 extra license for every additional core). Once the output files are generated, again Abaqus CAE is used for post-processing to extract the results.

PYTHON SCRIPTING

The analysis is modularized into function files. The design parameters are obtained from the optimizer and these parameters are passed initially to Abaqus CAE python script to generate the input file. Then the input files are submitted as a job and analyzed using the explicit solver to generate the output ".odb" file. The explicit analysis is the most time-consuming process of the optimization study and the analysis is performed using two CPU cores. Once the output files are generated, again Abaqus CAE is used for post-processing to extract the results. The extracted results are modified into objective function and constraint values to be fed into the optimizer. This loop continues until an optimal point is found / the optimizer terminates.

F.2. RESULTS USING FINAL OPTIMAL DESIGN PARAMETERS

The analyses results using the final optimal design parameters for both designs loaded with a given mass of explosive charge are shown below:

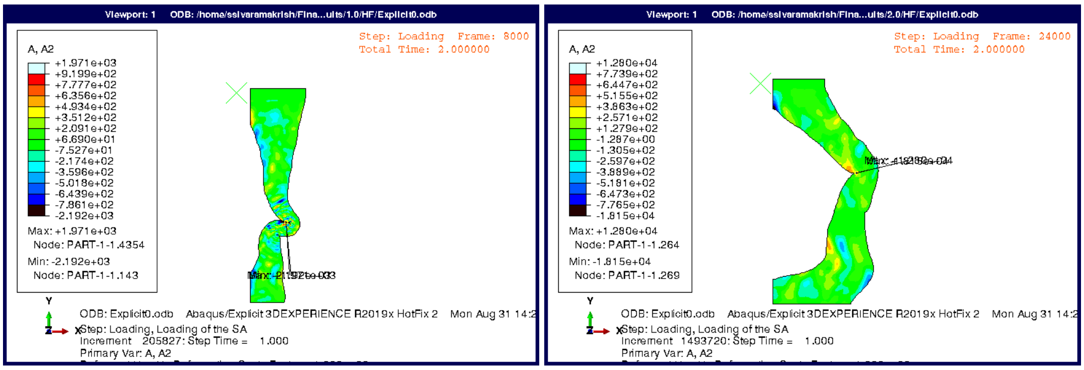

(a) Design 1.0 - 500kg (b) Design 2.0 - 500kg

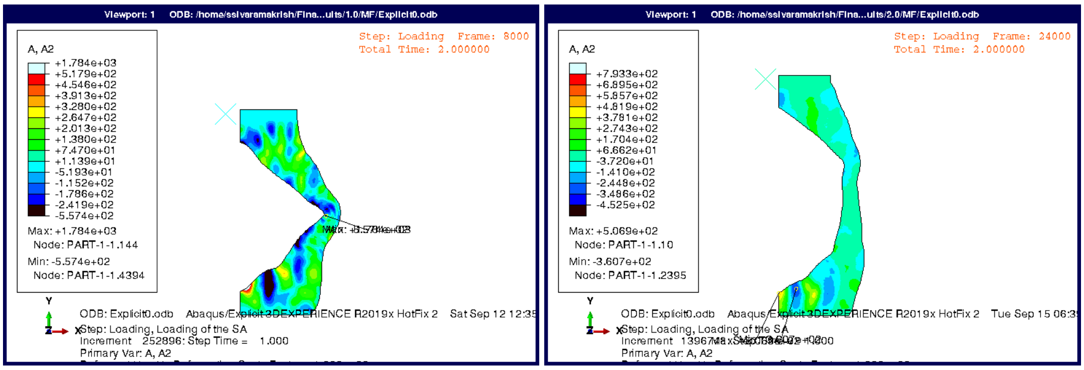

(c) Design 1.0 - 250kg (d) Design 2.0 - 250kg

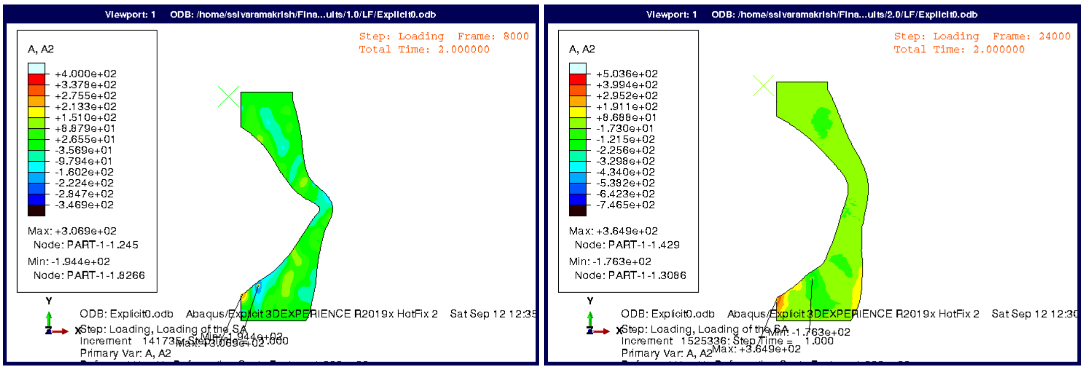

(e) Design 1.0 - 125kg (f) Design 2.0 - 125kg

Figure F.1: Acceleration results of objective mass using the final optimal design parameters at 1s after impact for both designs loaded with a given mass of explosive charge.

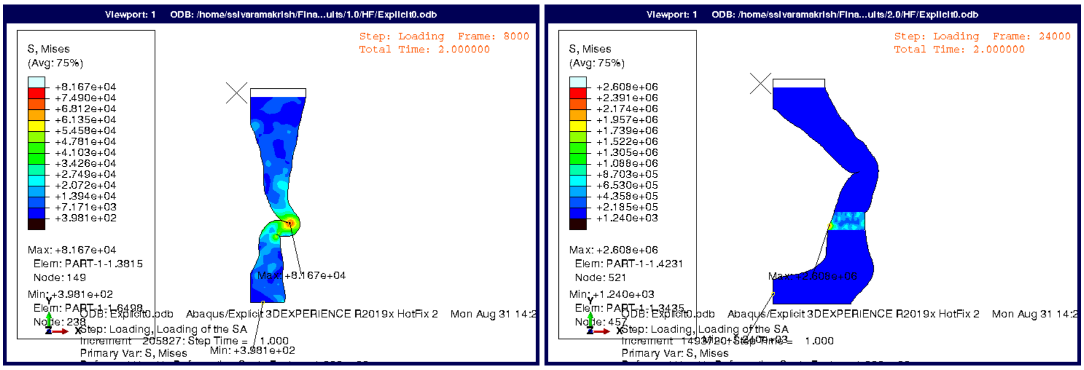

(a) Design 1.0 - 500kg (b) Design 2.0 - 500kg

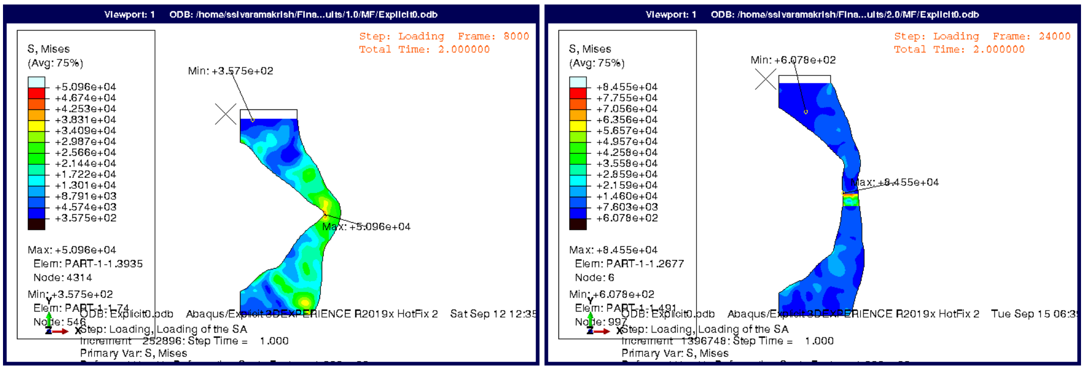

(c) Design 1.0 - 250kg (d) Design 2.0 - 250kg

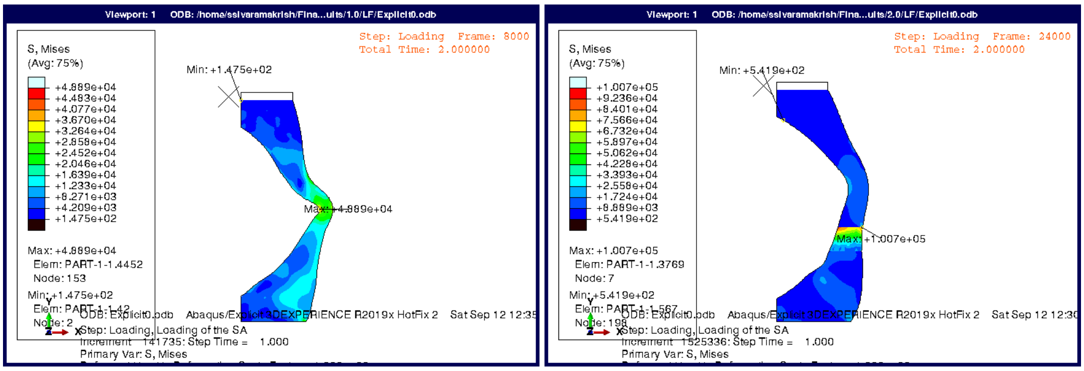

(e) Design 1.0 - 125kg (f) Design 2.0 - 125kg

Figure F.2: Stress results of the shock mount using the final optimal design parameters at 1s after impact for both designs loaded with a given mass of explosive charge.

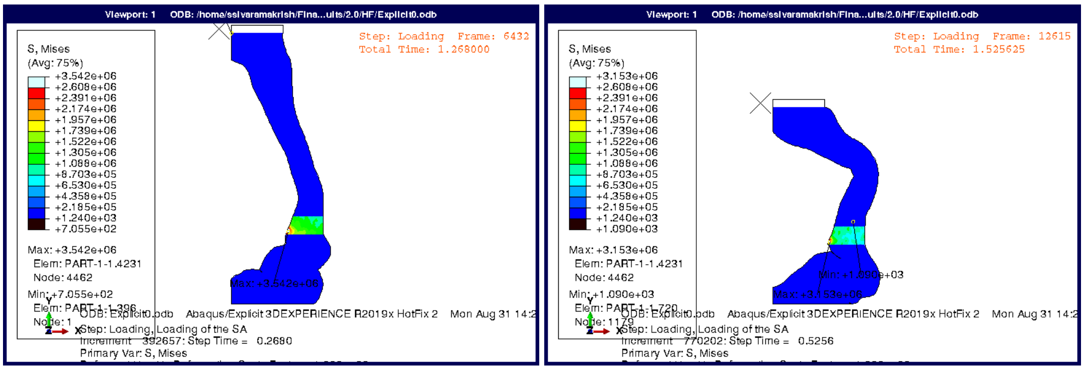

(a) Design 2.0 - Max (b) Design 2.0 - Min

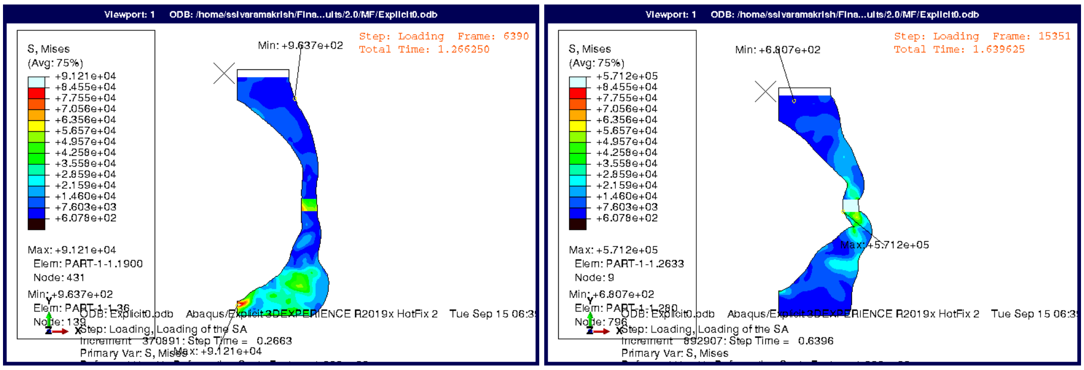

(c) Design 2.0 - Max (d) Design 2.0 - Min

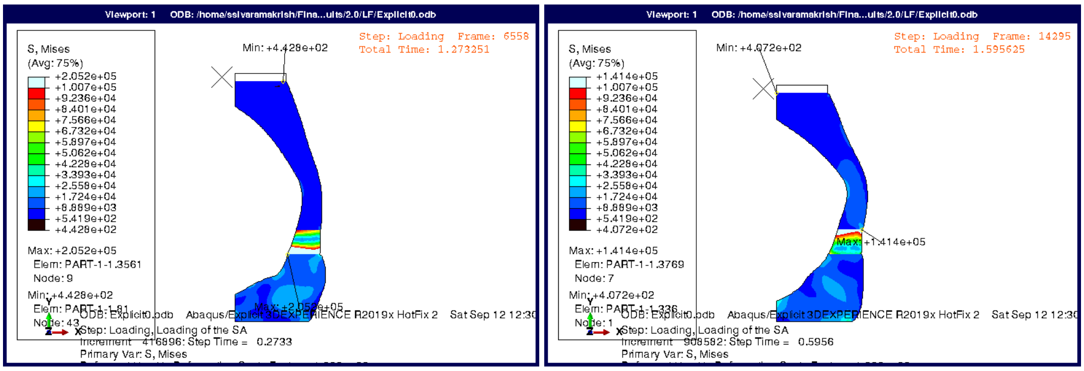

(e) Design 2.0 - Max (f) Design 2.0 - Min

Figure F.3: Stress results of the shock mount using the final optimal design parameters of Design 2.0 at maximum and minimum displacement of objective mass loaded with a given mass of explosive charge.

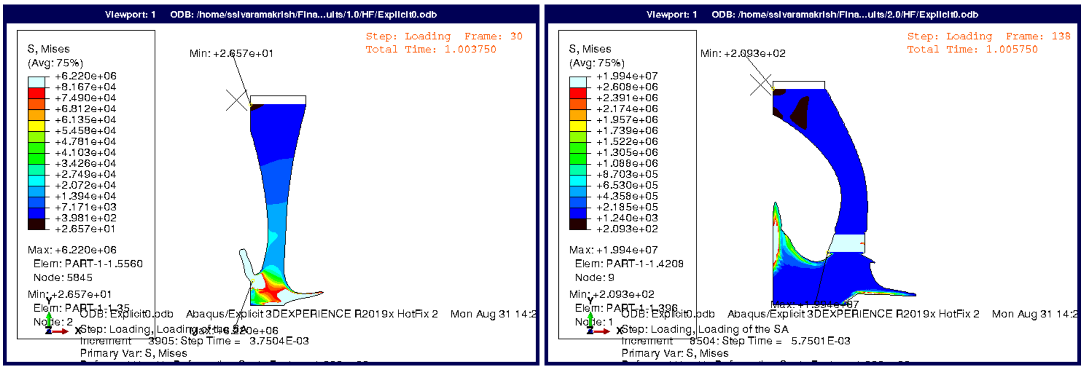

(a) Design 1.0 - 500kg

(b) Design 2.0 - 500kg

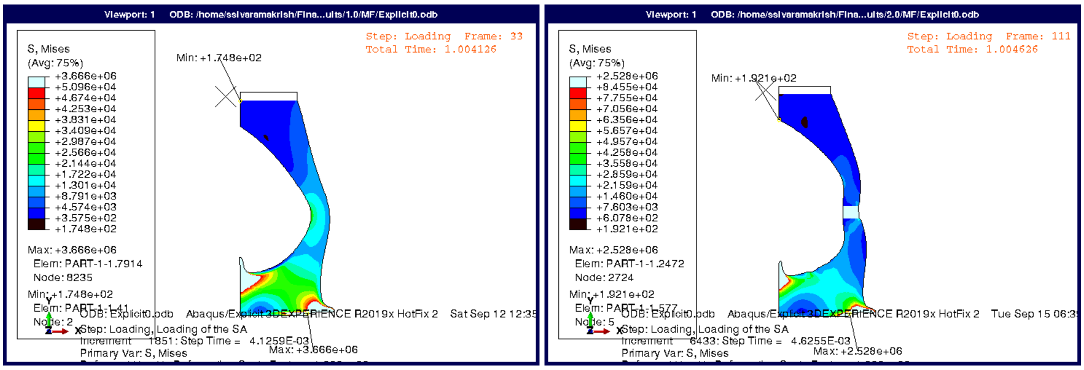

(c) Design 1.0 - 250kg

(d) Design 2.0 - 250kg

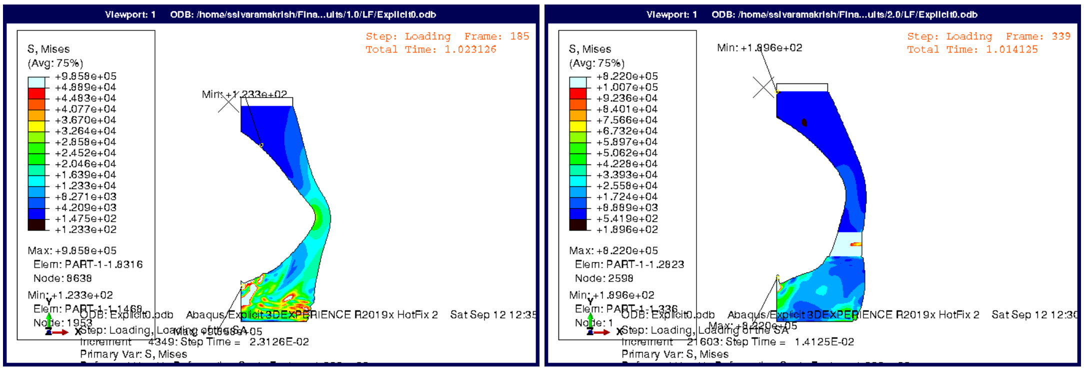

(e) Design 1.0 - 125kg

(f) Design 2.0 - 125kg

Figure F.4: Stress results at maximum stress experienced by the neoprene part of the shock mount using the final optimal design parameters for both designs loaded with a given mass of explosive charge.

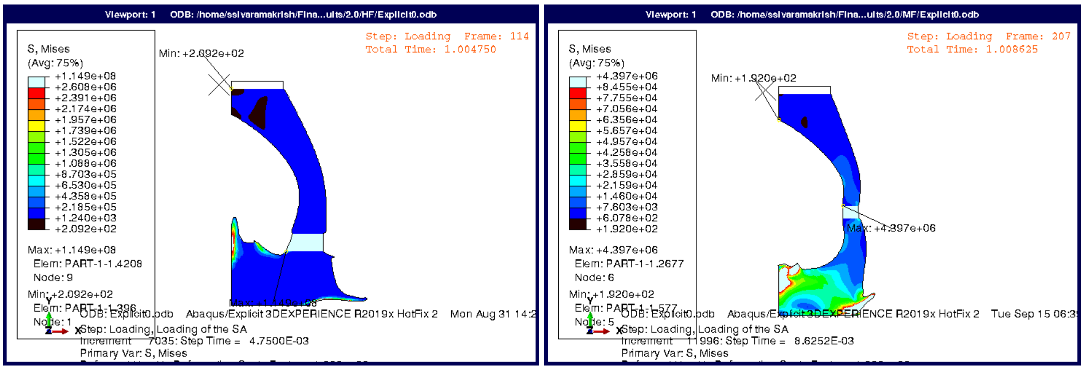

(a) Design 2.0 - 500kg

(b) Design 2.0 - 250kg

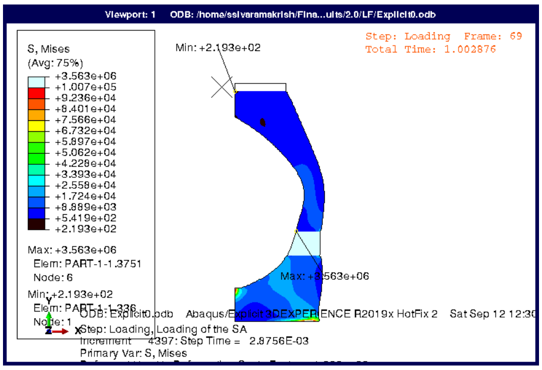

(c) Design 2.0 - 125kg

Figure F.5: Stress results at maximum stress experienced by the metallic interface part of the shock mount Design 2.0 using the final optimal design parameters loaded with a given mass of explosive charge.